Spontaneous and Evoked Calcium Waves Reveal State Dependent Functional Connectivity Changes in the Developing and Adult Mouse Cortex

Dennis Rene Tabuena

A dissertation

submitted in partial fulfillment of the

requirements for the degree of

Doctor of Philosophy

University of Washington

2021

Reading Committee:

William Moody, Chair

Bingni Brunton

David Perkel

Program Authorized to Offer Degree:

Graduate Program in Neuroscience

University of Washington

Abstract

Spontaneous and Evoked Calcium Waves Reveal State Dependent Functional Connectivity Changes in the Developing and Adult Mouse Cortex

Dennis Rene Tabuena

Chair of the Supervisory Committee:

William Moody

Department of Biology

During development, and into adulthood, the mouse cortex exhibits propagating waves that span the entire cortex. These waves are typically observed as a pattern whereby local cortical activity is followed by activation in adjacent areas. This leads to a propagating chain reaction that engages the entire cortex in a spatio-temporally coordinated manner. Typically in adulthood these waves are associated with slow wave sleep where they have been implicated in long term memory consolidation. During cortical development, previous studies had observed these waves only in slice preparations and their function was less clear, however they are currently thought to be linked to neuronal migration and maturation. Study of these waves had been limited in some part due to challenges associated with observing and quantifying their complex dynamics including propagation patterns and brain/behavior state dependencies. Here I present three

studies to address these challenges in order to help further elucidate the nature and function of these pan-cortical waves. First, we use different modes of anesthetization in adults to determine the state dependent dynamics of local and propagating activity, both spontaneous and sensory evoked. Second, we make the first observation of developmental waves *in vivo* establishing the timeline of emergence, their state dependence, and electrical signature. Finally we explore the utility of the finite-time Lyapunov exponent to visualize propagating activity and capture novel insights into the structure of waves.

Table of Contents

Introduction

Coordinated spontaneous activity plays many roles in assembly and maturation of neural networks. This activity ranges from intrinsic single cell activity to broadly propagating (Pan-cortical) waves (Easton et al., 2014; Barger et al., 2016; Mukherjee et al., 2017; Molnar et al., 2020; Rio-Berrmudez et al., 2020). Previous work in our lab has focused on these Pan-cortical Waves that cross the entire cortex in neonatal mouse brain slices. Work in slices has allowed our group to explore the fundamental facets of these waves and how they emerge and subside during the first few weeks after birth (Conhaim et al., 2010, 2011; Easton et al., 2014; Barger et al., 2016). Traveling waves such as these intrinsically have spatial-temporal properties but it is unclear how these function in development. Given what we know about how spontaneous activity and waves function in the development and patterning of visual, somatosensory, auditory and motor areas of the cortex (Heck et al., 2008; Kandler et al., 2009; Bonetti and Surace 2010; Kirkby et al., 2013), it seems likely that spatio-temporal properties are similarly important for pan-cortical wave function.

How the cortex operates in a highly synchronous mode to propagate waves, while at the same time developing the spatially and temporally restricted responses critical to mature cortical processing, remains unclear. A potential solution would be to segregate these modes of function in time via different functional cortical states. A hypothesis as to how this might occur is suggested by the striking resemblance of perinatal waves to the adult slow wave activity during slow wave sleep (SWS). During SWS, activity is synchronized in to large electrical events that span the entire cortex (Brown et al. 2012). Sleep has been implicated in the consolidation and transfer of hippocampal short-term memory into long term cortical connections, a process highly likely to be reliant on activity dependent plasticity. The similarities between adult sleep and developmental waves suggest the possibility of a common mechanism to enhance and strengthen new cortical connections in young and mature animals. However, no studies to date have directly examined the relationship between these two phenomena.

Unfortunately, two dimensional excised tissues can not fully replicate the three dimensional structure or natural states of the brain in vivo, nor can it give insight into the interactions with whole animal behavior. Thus, despite a number of in vitro studies outlining the basic properties of cortical waves in development, we still know relatively little about their role in the context of the whole animal, or indeed if they even occur in the intact brain (Dzhala et al., 2012). Therefore we aimed to harness modern in vivo methods to characterize and advance the understanding of dynamic and spatio-temporally complex patterns in cortical activity.

Recent developments in neuroscience recording technology such as genetic manipulation, high signal to noise ratio fluorophores, and advanced analytics methods have expanded our ability to explore the properties of the cortex of the mammalian brain, yet several challenges remain and new ones have arisen. In the pursuit of understanding complex problems the field has always sought to collect measures of brain activity in greater scale, specificity and resolution. High density recording methods such as neuropixels (Jun et al. 2017), and advancements in fluorophores like GCamp6 (Chen et al., 2013) have dramatically raised the bar in this area, allowing simultaneous recording from hundreds to thousands of neurons. Furthermore combining sensors like GCamp under the dual regulation by genetic expression with Cre/Lox system and chemical control with tetracycline on/off system, into single high expressing lines (Daigle et al., 2018), and the ever growing library of driver lines have empowered researchers to fine tune the spatial and temporal focus of the hypotheses to be tested.

The current relative ease of data collection has increasingly led to an array of large complex data sets which in some cases have outpaced traditional analysis methods and have far surpassed the reach of manual data curation. Thus, the field of neuroscience has begun to borrow analytical methods from other fields such as machine learning, physics, and fluid dynamics. Many of these methods fall into the family of dimensionality reduction methods which seek to approximate the complexity of large data sets using a smaller subset of underlying patterns in the data, in the hopes that these patterns can be related back to better understand the neurophysiology.

Another consequence of the ease of data collection has been the increased ability to capture beyond the traditionally narrow spatio-temporal scope of behavior or activity. Rather than focusing on specific events in a particular brain area or under specific restricted conditions, it has become more common to obtain recordings that span large areas of the brain across more dynamic and naturalistic scenarios (Murphy et al., 2020; de Vries et al., 2020). This further compounds the ability to test dynamic hypotheses that go beyond our previously restricted view of the brain. This big data approach is particularly well suited to expanding on our current understanding of cortical function. With the ability to record across the entire cortical surface we are now able to begin probing long range activity such as how sensory information expands beyond primary sensory areas of cortex in a data driven manner, whereas previously hypotheses were limited to interactions to a handful of ad hoc predetermined areas. Similarly the expanded temporal range of recordings has increased the ability to record long periods of naturalistic behavior. This has given further insight into the nonlinearities in brain activity patterns that could not be otherwise observed, such as attention those found across brain states such as wake or sleep; passive vs attentive processing; and longitudinally through development of the nervous system.

Propagating cortical waves are particularly well suited to study with these new methods. By their nature it is necessary to record many neurons across distances spanning up to the entire cortex. In addition, we hypothesize that waves (along with other observed activity patterns) will likely be more heterogenous than those observed in slices. Variations in propagation patterns and dynamics and will likely be dependent on the full brain structure as well as upon the brain state. Thus the works presented here attempt to take advantage of these recent technologies and modern methods to characterize and advance the understanding of dynamic and spatio-temporally complex wave patterns in the cortex. We aimed to address the lack of knowledge with a novel approach and a series of experiments to better understand how waves are exhibited in vivo, their relationship to sleep/wake cycles, and how they may contribute to sensory cortex development. Probing wave properties in the most natural setting to date will greatly expand our knowledge and provide the foundation for future study in activity dependent development. Through these efforts we were able to make observations of wave activity in anesthetized adult mice and in neonatal pups. We were able to show that different modes of anesthesia could induce brain states in adults that facilitated or suppressed stimulated waves. These waves were the result of propagating activity out of primary sensory areas to the rest of the cortex observable by calcium imaging and low frequency local field potentials. In neonates we were able to confirm the emergence of waves during the first week after birth. These waves were restricted to periods of sleep indicating a dependence on sleep state which was then confirmed using sleep deprivation. In addition analysis of activity patterns using data driven feature extraction showed differential patterns across animal age and behavior state. By combining calcium imaging with simultaneous EEG we were able to discover the broad

spectrum of synchronized activity driving calcium waves. Finally adapting methods for fluid flow analysis to calcium imaging was demonstrated to be a useful tool for describing wave activity in both neonates and adult mice. Together these results begin to paint a clearer picture of how waves are regulated and provide the tools to further probe their function in cortical development and adult plasticity.

References:

Barger, Z., Easton, C. R., Neuzil, K. E., & Moody, W. J. (2016). Early network activity propagates bidirectionally between hippocampus and cortex. Developmental Neurobiology, 76(6), 661–672. https://doi.org/10.1002/dneu.22351

Bonetti, C., & Surace, E. M. (2010). Mouse embryonic retina delivers information controlling cortical neurogenesis. PLoS ONE. https://doi.org/10.1371/journal.pone.0015211

Brown, R. E., Basheer, R., McKenna, J. T., Strecker, R. E., & McCarley, R. W. (2012). Control of Sleep and Wakefulness. Physiological Reviews. https://doi.org/10.1152/physrev.00032.2011

Chen, T. W., Wardill, T. J., Sun, Y., Pulver, S. R., Renninger, S. L., Baohan, A., Schreiter, E. R., Kerr, R. A., Orger, M. B., Jayaraman, V., Looger, L. L., Svoboda, K., & Kim, D. S. (2013). Ultrasensitive fluorescent proteins for imaging neuronal activity. Nature, 499(7458), 295–300. https://doi.org/10.1038/nature12354

Conhaim, J., Cedarbaum, E. R., Barahimi, M., Moore, J. G., Becker, M. I., Gleiss, H., Kohl, C., & Moody, W. J. (2010). Bimodal septal and cortical triggering and complex propagation patterns of spontaneous waves of activity in the developing mouse cerebral cortex. Developmental Neurobiology. https://doi.org/10.1002/dneu.20797

Conhaim, J., Easton, C. R., Becker, M. I., Barahimi, M., Cedarbaum, E. R., Moore, J. G., Mather, L. F., Dabagh, S., Minter, D. J., Moen, S. P., & Moody, W. J. (2011). Developmental changes in propagation patterns and transmitter dependence of waves of spontaneous activity in the mouse cerebral cortex. Journal of Physiology. https://doi.org/10.1113/jphysiol.2010.202382

Daigle, T. L., Madisen, L., Hage, T. A., Valley, M. T., Knoblich, U., Larsen, R. S., Takeno, M. M., Huang, L., Gu, H., Larsen, R., Mills, M., Bosma-Moody, A., Siverts, L. A., Walker, M., Graybuck, L. T., Yao, Z., Fong, O., Nguyen, T. N., Garren, E., … Zeng, H. (2018). A Suite of Transgenic Driver and Reporter Mouse Lines with Enhanced Brain-Cell-Type Targeting and Functionality. Cell, 174(2), 465-480.e22. https://doi.org/10.1016/j.cell.2018.06.035

de Vries, S. E. J., Lecoq, J. A., Buice, M. A., Groblewski, P. A., Ocker, G. K., Oliver, M., Feng, D., Cain, N., Ledochowitsch, P., Millman, D., Roll, K., Garrett, M., Keenan, T., Kuan, L., Mihalas, S., Olsen, S., Thompson, C., Wakeman, W., Waters, J., … Koch, C. (2019). A large-scale standardized physiological survey reveals functional organization of the mouse visual cortex. Nature Neuroscience 2019 23:1, 23(1), 138–151. https://doi.org/10.1038/s41593-019-0550-9

Del Rio-Bermudez, C., Kim, J., Sokoloff, G., & Blumberg, M. S. (2020). Active Sleep Promotes Coherent Oscillatory Activity in the Cortico-Hippocampal System of Infant Rats. Cerebral Cortex, 30(4), 2070–2082. https://doi.org/10.1093/cercor/bhz223

Dzhala, V., Valeeva, G., Glykys, J., Khazipov, R., & Staley, K. (2012). Traumatic Alterations in GABA Signaling Disrupt Hippocampal Network Activity in the Developing Brain. Journal of Neuroscience, 32(12), 4017–4031. https://doi.org/10.1523/JNEUROSCI.5139-11.2012

Easton, C. R., Weir, K., Scott, A., Moen, S. P., Barger, Z., Folch, A., Hevner, R. F., & Moody, W. J. (2014). Genetic Elimination of GABAergic Neurotransmission Reveals Two Distinct Pacemakers for Spontaneous Waves of Activity in the Developing Mouse Cortex. Journal of Neuroscience, 34(11), 3854–3863. https://doi.org/10.1523/jneurosci.3811-13.2014

Heck, N., Golbs, A., Riedemann, T., Sun, J.-J., Lessmann, V., & Luhmann, H. J. (2008). Activity-Dependent Regulation of Neuronal Apoptosis in Neonatal Mouse Cerebral Cortex. Cerebral Cortex. https://doi.org/10.1093/cercor/bhm165

Jun, J. J., Steinmetz, N. A., Siegle, J. H., Denman, D. J., Bauza, M., Barbarits, B., Lee, A. K., Anastassiou, C. A., Andrei, A., Aydin, Ç., Barbic, M., Blanche, T. J., Bonin, V., Couto, J., Dutta, B., Gratiy, S. L., Gutnisky, D. A., Häusser, M., Karsh, B., … Harris, T. D. (2017). Fully integrated silicon probes for high-density recording of neural activity. Nature, 551(7679), 232–236. https://doi.org/10.1038/nature24636

Kandler, K., Clause, A., & Noh, J. (2009). Tonotopic reorganization of developing auditory brainstem circuits. In Nature Neuroscience. https://doi.org/10.1038/nn.2332

Kirkby, L. A., Sack, G. S., Firl, A., & Feller, M. B. (2013). A role for correlated spontaneous activity in the assembly of neural circuits. In Neuron. https://doi.org/10.1016/j.neuron.2013.10.030

Molnár, Z., Luhmann, H. J., & Kanold, P. O. (2020). Transient cortical circuits match spontaneous and sensory-driven activity during development. Science, 370(6514). https://doi.org/10.1126/SCIENCE.ABB2153

Mukherjee, D., Yonk, A. J., Sokoloff, G., & Blumberg, M. S. (2017). Wakefulness suppresses retinal wave-related neural activity in visual cortex. Journal of Neurophysiology. https://doi.org/10.1152/jn.00264.2017

Murphy, T. H., Michelson, N. J., Boyd, J. D., Fong, T., Bolaños, L. A., Bierbrauer, D., Siu, T., Balbi, M., Bolaños, F., Vanni, M., & Ledue, J. M. (2020). Automated task training and longitudinal monitoring of mouse mesoscale cortical circuits using home cages. ELife, 9, 1–91. https://doi.org/10.7554/ELIFE.55964

Functional States Shape the Spatiotemporal Representation of Population and Cortex-wide Neural Activity in Mouse Sensory Cortex

Miriam Schwalm*[1,2], Dennis Tabuena*[3], Curtis Easton*[3], Tom Richner[3], Pierre Mourad[3], Hiro Watari[2,3], William Moody[3] & Albrecht Stroh[1,4c]

(in preparation)

[1]Institute of Pathophysiology, University Medical Center Mainz
[2]Department of Biological Engineering, Massachusetts Institute of Technology, Cambridge, MA
[3]Department of Biology, University of Washington, Seattle, WA
[4]Leibniz Institute for Resilience Research, Mainz
*These authors contributed equally to this work
[c] Corresponding author

Abstract

The spatiotemporal representation of neural activity during rest and upon sensory stimulation in cortical areas is highly dynamic, and may be predominantly governed by the respective brain state. Active, or persistent cortical states are generally associated with a sustained depolarization of cortical neurons and suppression of silent states, often present during awake periods but a similar state may also be maintained by certain sedatives. Conversely, in slow wave like activity, dominating slow wave sleep, bimodal patterns of bursts of neural activity alternating with silent periods can spread over the entire cortex. Here we characterized two distinct functional states in the sensory cortices of mice that differ in their spatiotemporal characteristics on the local and global cortical scale. Using electrophysiological recordings in conjunction with local and wide-field calcium imaging, we examine how sensory information propagates throughout the cortex in a state dependent manner. We put forward the notion that the spatio-temporal characteristics of both sensory and stimulus-evoked responses in the cortex is governed by rather distinct functional states, putatively serving two distinct neurophysiological roles:

Introduction

Neural networks undergo constant fluctuations provoked by changes of internally generated activity, even in the absence of external stimulation. Alternating states of excitability are associated with changes in global functional state, as between sleep and wakefulness (Steriade et al., 1991; Destexhe et al., 2007), from inattention to vigilance (McGinley et al., 2015a; Boly et al., 2007) or from resting to locomotion (Poulet & Petersen, 2008; Eggermann et al., 2014). These changes of neural activity are reflected in the ongoing neuronal signal and shape responses upon incoming sensory information on different spatial scales, from single neurons (Li et al., 2004; Steriade et al., 1993), over local populations (Constantinople and Bruno 2011) to global functional connectivity (Aedo-Jury et al., 2020).

The spatiotemporal representation of neural activity during rest and upon sensory stimulation in cortical areas therefore has to be state-dependent and dynamic. Active cortical states are generally associated with a sustained depolarization of cortical neurons

(Constantinople & Bruno, 2011; Destexhe et al., 2007; Sheroziya & Timofeev, 2015) and suppression of silent states (Steriade et al., 1991; McGinley et al., 2015b), leading to fast ongoing fluctuations of neural activity. Such persistent activity is often present during awake periods (Corsi-Cabrera et al., 2001; Brown et al., 2012), but a similar state may also be maintained by certain sedatives (Constantinople & Bruno, 2011; Schwalm et al., 2017). Conversely, bursts of neural activity alternating with silent periods can be found under a plethora of different conditions in populations of thalamocortical neurons (Steriade et al., 2001; Rochefort et al., 2009; Steriade et al., 1993c; Timofeev et al., 2001; Sanchez-Vives et al., 2017). These bimodal patterns of activity have their origin in deeper layers of the cortex (Chauvette et al., 2010; Sanchez-Vives & McCormick, 2000; Stroh et al., 2013) and were shown to affect neuronal excitability as well as stimulus responses of neuronal networks throughout the brain (McGinley et al., 2015b; Petersen et al., 2003; Steriade et al., 1993d,c). Such slow wave like activity can occur rather locally (Nir et al., 2011), or can spread over the entire cortex (Stroh et al., 2013) , while being spontaneously triggered mostly in frontal areas (Massimini et al., 2004; Stroh et al., 2013; Matsui et al., 2016). Although slow waves can be found during awake resting (Crochet & Petersen, 2006; Vyazovskiy et al., 2011; McGinley et al., 2015a) they classically have been described during states of deep anesthesia (Sanchez-Vives & McCormick, 2000; Petersen et al., 2003; Seamari et al., 2007; Chauvette et al., 2011; Stroh et al., 2013; Busche et al., 2015; Zucca et al., 2017; Sanchez-Vives et al., 2017) and although the main features are similar to those of slow wave sleep (SWS) waves (Destexhe et al., 2007; Sanchez-Vives et al., 2017), slow waves under anesthesia occur more rhythmically and synchronously across the cortex and show longer periods of inactivity between waves than it is the case during SWS (Chauvette et al., 2011; Busche et al., 2015).

Here we characterized two distinct functional states in the sensory cortices of mice that differ in their spatiotemporal characteristics on the local and global cortical scale: a slow wave (SW) state typified by bimodal activity characterized by relative quiescence with brief bursts of globally synchronous activity, and a persistently active (PA) state with constant, uninterrupted local activity. Using electrophysiological recordings in conjunction with local and wide-field calcium imaging, we examine how sensory information propagates throughout the cortex in a state dependent manner. The state dependent propagation modes we characterize represent an experimental model for cortical information processing and may be useful to explain response variability of neural networks under seemingly constant conditions.

Results

Mesoscale Assessment of Population Activity reveals two distinct spatial activity patterns

We subjected two different strains (see methods) of transgenic GCaMP6 mice to two sedative regimens (SW and PA), which were previously shown to yield distinct local and brain-wide activity patterns (Schwalm et al., 2017, Aedo-Jury et al., 2020). We explored the mesoscale correlates of these two activity patterns using thinned-skull preparations and wide field CCD camera imaging techniques (Figure 1 A). We obtained high spatial resolution images including almost the entire cortical surface to reveal the spatial activation pattern in each state. We found activity signatures sharing key characteristics of the two activity states previously explored by connectivity analyses in combined resting state fMRI and calcium photometry recordings (Aedo-Jury 2020): ongoing activity in PA state displayed rapid oscillations with spatially diverse activity Over the course of 9 sec short bursts of Ca activity are visible at

different times across the field of view (Fig. 1B, Sup Vid 1). In contrast, ongoing activity in SW was characterized by slow propagating waves. In the supplemental video 2 (still frames in Fig. 2B) a single propagating burst of activity that spans the entire field of view can be seen. Indeed, - analysis based on the mean signal across the field of view exemplifies distinct signal dynamics (Fig. 1 C, D, E). We calculated the mean dfof signal for each pixel in the field of view to examine the spatial and temporal differences between states (Fig. 1C). The SW state showed large amplitude oscillations in the mean signal due to near synchronous activation of the entire field of view. In contrast the PA state showed rapid small amplitude oscillations where the field of view is never fully active nor fully quiescent. To quantify this difference, we calculated the probability distribution of the mean dfof trace with respect to time (Fig 1DE). In the probability distribution of the SW has the largest mass at near zero activation with and exponential like shift to high activations while the PA distribution shows a bimodal distributions with masses at ~10% and 40% activation. The differences in these distributions were significant when compared with permutation-based test.

We complemented this approach by observing responses upon sensory stimulation using two modalities: visual stimulation, subjecting the animal to light flashes administered to the contralateral eye at an inter-event interval of 2-4s; and sensory stimulation, i.e. electric stimulation of the hindpaw with a an inter-event interval of 2-4s Stimulation current was manually titrated for each animal to induce a cortical response but not cause a reflexive twitch.

Wide field time-lapse imaging of sensory responses during PA state revealed a spatially highly stereotypical response to visual and somatosensory stimuli (Fig. 1 F). Upon visual stimuli, an area of activation spanning 6.9 ± 1.7 mm^2 (n=9) was observed in PA state ($p<0.001$, student's t-test; Figure 1 G). In sharp contrast, the response area upon somatosensory stimuli during SW state, with a mean of 23.1 ± 0.3 mm^2 (n=6), was greater than the mean somatosensory response area during PA state (7.5 ± 2.0 mm^2; n=6, $p<0.001$, student's t-test). There was no statistically significant difference between the response areas for visual and somatosensory stimuli within SW ($p=0.687$) or PA states ($p=0.827$). This effect may be visualized by comparing the maximum extent of activity in the time-lapse images of PA state sensory responses (Figure 1) with the sensory responses of SW state (Figure 3).

Local optical recordings reveal unique temporal signal dynamics of SW and PA

To characterize the temporal characteristics of ongoing and sensory-evoked activity during SW and PA with high temporal resolution, we employed single optic-fiber based calcium and local field potential recordings in wild-type (WT) mice. During PA state a continuous signal was present in the photometry and LFP transients, devoid of prolonged periods of quiescence (Figure 2 A, C). The corresponding LFP spectrogram shows continuous power values around 15 Hz (Figure 2 C). SW activity was characterized by stereotypical fluorescence waves and LFP deflections, which were interrupted by silent periods ranging at (Figure 2 A, B), as reported previously by us and others (Schwalm 2017, Aedo-Jury 2020, Stroh 2013, Messer et al., 2020). The LFP's spectrogram reflects the alternation of slow wave events and silent periods in the frequency distribution, showing high power during slow wave events (Figure 2 F). Next, to explore if the observed differences in the ongoing signals have impact on the neuronal encoding of sensory stimuli, neuronal responses upon forepaw stimulation were compared during PA and

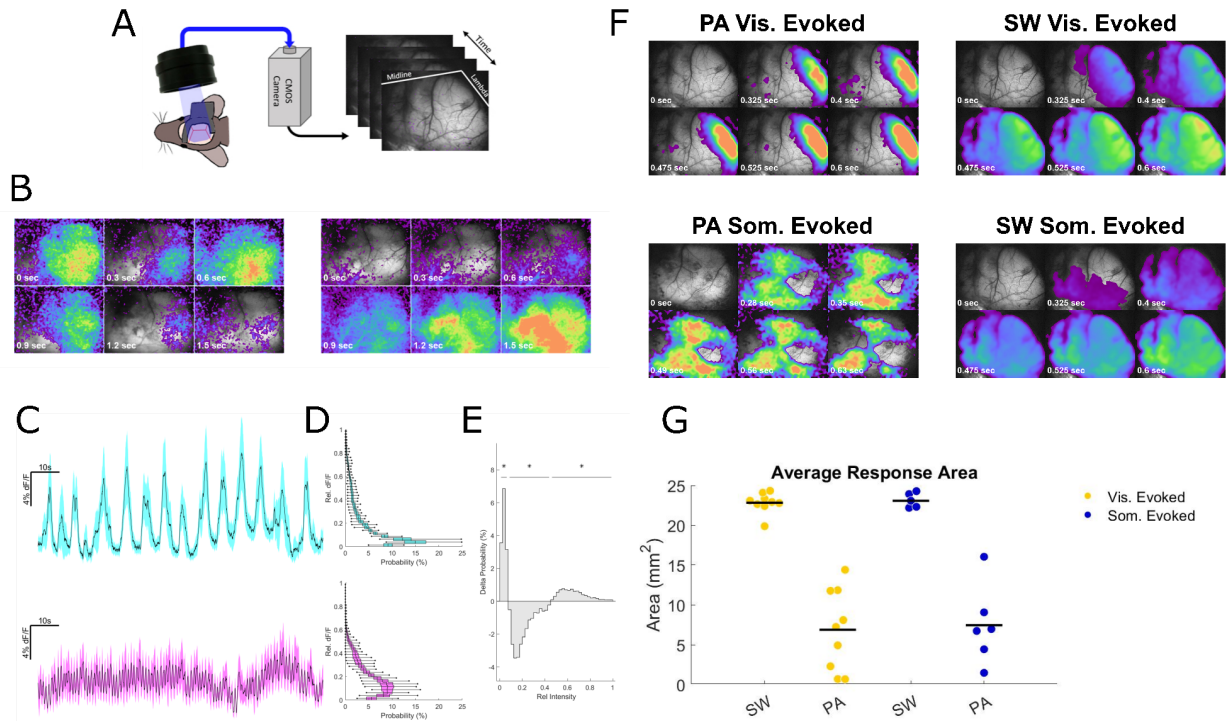

Figure 1. Camera recordings of transgenic GCaMP6 animals reveal mesoscale spatiotemporal characteristics of two distinct activity states. (A) Camera recording setup. (B) Images of different time points during recording of ongoing activity of PA and SW state. (C) Mean percent dF/F across cortical field of view for SW state (top) and PA state (bottom) shown in (B). Shaded region indicates the SD at each time point. (D) Average probability distributions of mean dF/F across all animals. Center indicates lines indicate mean probability for each bin, boxes indicate S.D. and whiskers indicate the minimum and maximum values (n=9 animals). (E) Difference of the mean probability distributions (from D), positive probabilities indicate higher occurrence during SW state while negative indicate higher occurrence in the PA state. Significant regions were determined using permutation based testing and are indicated with horizontal bars with asterisks ($p<0.0001$ for all after Bonferroni correction). (F) Sensory evoked activity (a brief 10 ms LED light flash to the left eye for visual stimulation (vis stim) and a mild electric stimulus (1 mA, 10ms pulse) to the right forepaw (som stim) show propagation properties of elicited activity for PA and SW state (average of X stimuli each). (G) Area of response to stimuli for visual and somatosensory stimuli in SW and PA state.

SW state. During PA, short-delay responses become apparent upon electric forepaw stimulation pulses (1 mA, 10 ms) (Figure 2 G, H), while during SW state, forepaw stimuli reliably evoked SW events with longer latency and duration (mean probability 90 %; n = 4 mice; Figure 2 G, H). During SW state stimulus trains of 3 Hz for 4 s led to comparable calcium waves as those evoked by single pulses, while during PA state short-latency responses were elicited by every stimulus pulse upon the same stimulation paradigm (LFP recordings reveal similar signal characteristics; Supplementary Figure 1).

To explore if functional state dynamics have influences on sensory responses in awake mice, animals with implanted optic fibers for calcium recordings in S1 and V1 were head fixed on a tracking ball which allowed them to initiate running voluntarily throughout the course of a measurement. Visual stimulation in awake animals lead to similar short-latency responses in V1 as previously shown under the light sedative PA state condition (Supplementary Figure 2 A, B) and to responses of longer latency when the animal was resting (Supplementary Figure 2B), in line with electrophysiological studies (Dadarlat & Stryker, 2017; Kaneko et al., 2017; Busse et al., 2017; Vinck et al., 2015). The reported properties of ongoing activity are not limited to the type of anesthesia used for eliciting the two functional states, SW state can be reliably evoked under Ketamin/Xylazin anesthesia and PA state can be evoked by low dosages (0.4-0.6%) of isoflurane or during awake conditions (Supplementary Figure 2 C-E).

The Role of Functional State for Cortico-cortical Sensory Processing

To further inform on the spatiotemporal properties of the described states and to probe the impact of functional state on cortical responses upon incoming information, population calcium signals have been recorded in two different sensory cortices (primary somatosensory cortex (S1) and primary visual cortex (V1); Figure 3 A), under the previously described anesthetized conditions. Here, simultaneous calcium recordings with optic fibers placed in S1 and contralateral V1 showed synchronous SW events in both regions (Figure 3 B, C) with events being detected in 60 % of the cases occurring first in S1. To further understand the directionality of slow wave propagation, we plotted the mean cross-correlation S1 versus V1 for spontaneously occurring slow wave events (Figure 3 C), suggesting a propagation of waves in anterio-posterior direction as previously reported by others (Stroh et al., 2013; Massimini et al., 2004; Matsui et al., 2016). We quantified the delay between event onset in V1 versus S1 for spontaneous events (Figure 3). Overall, spontaneous events had a mean S1 to V1 delay of 128ms (median: 167, IQR: 79.4–262, n: 217).

Propagation of waves was also observed for stimulus-induced SW events (Figure 3). In mice electric forepaw stimulation (1 mA pulses contralateral to the recording site, Figure 3 D, E) evoked a slow calcium wave detected after a latency of 98 ± 7 ms (n = 141 events in 7 animals) in S1 and with a mean latency of 204 ± 7 ms (n = 67 events in 3 animals) in ipsilateral V1 (in contralateral V1 waves were detected after a mean latency of 228 ms ± 8 ms; n = 81 events in 4 animals). Visually evoked slow waves (Figure 3 F, G) were detected with a mean latency of 115 ms (± 4 ms; n = 115 events in 7 animals) in V1 and with a mean latency of 263 ms (± 10 ms; n = 40 events in 3 animals) in ipsilateral S1 (in contralateral S1 waves were detected after a mean latency of 288 ms ± 11 ms; n = 71 events in 4 animals). The propagation velocity of these waves was on average 30 mm/s, similar to values reported by others (Stroh et al., 2013).

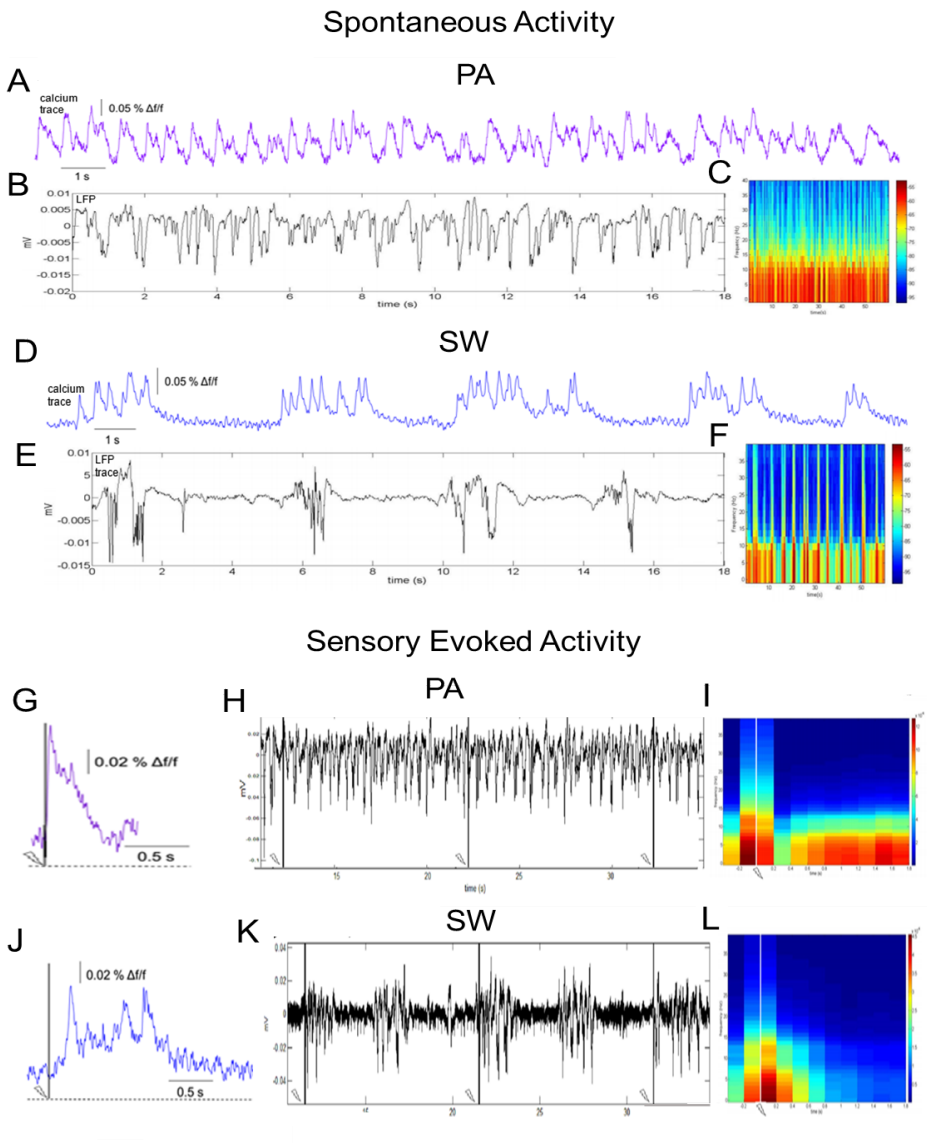

Figure 2. Local dynamics of SW and PA state. (A) Individual calcium trace recorded by an optic fiber upon OGB-1 staining in somatosensory cortex of an isoflurane anesthetized mouse during SW state activity (blue). Stereotypical, long-duration calcium waves interrupted by silence periods become apparent. (B) LFP signals under the same conditions show similar dynamics (different recording, but same timescale as in A). (C) The spectrogram of the LFP signal in (B) reflects the alternation active and silent periods in the frequency distribution, with the appearance of higher frequencies (40 Hz) during SW events. (D) During PA state induced by medetomidine sedation the calcium trace (purple) recorded in the same animal as in (A) shows a continuous fluctuation where prolonged periods of quiescence disappear, which is also visible in the LFP signal (E, different recording, but same timescale as in D). (F) The spectrogram of the LFP signal in (E) reflects this ongoing persistent activity showing continuous frequencies around 15 Hz. (G) Electric forepaw stimulation pulses (10 ms, 1 mA) reliably evokes calcium response in PA state (single trial response). (H) Stimulus pulses evoke short-latency LFP spikes during PA state (note that these deflections occur very briefly after the stimulus pulse and for a very short duration in the depiction chosen to be comparable to (K). (I) The stimulus-locked spectrogram of the LFP trace in (H) shows time-frequency profiles before and after stimulation pulse (n = 30 events). (J) During SW state the same stimulus pulse evokes a slow calcium wave with a mean probability of 90 % (n = 4 animals) which differs in latency, duration and microarchitecture from an evoked response during PA state in the same animal (G). (K) The response properties observed for the calcium signal in (J) also account for the LFP signal during SW state. (L) The stimulus-locked spectrogram of the LFP recording in (K) shows time-frequency profiles before and after the stimulation pulse (n = 30 events).

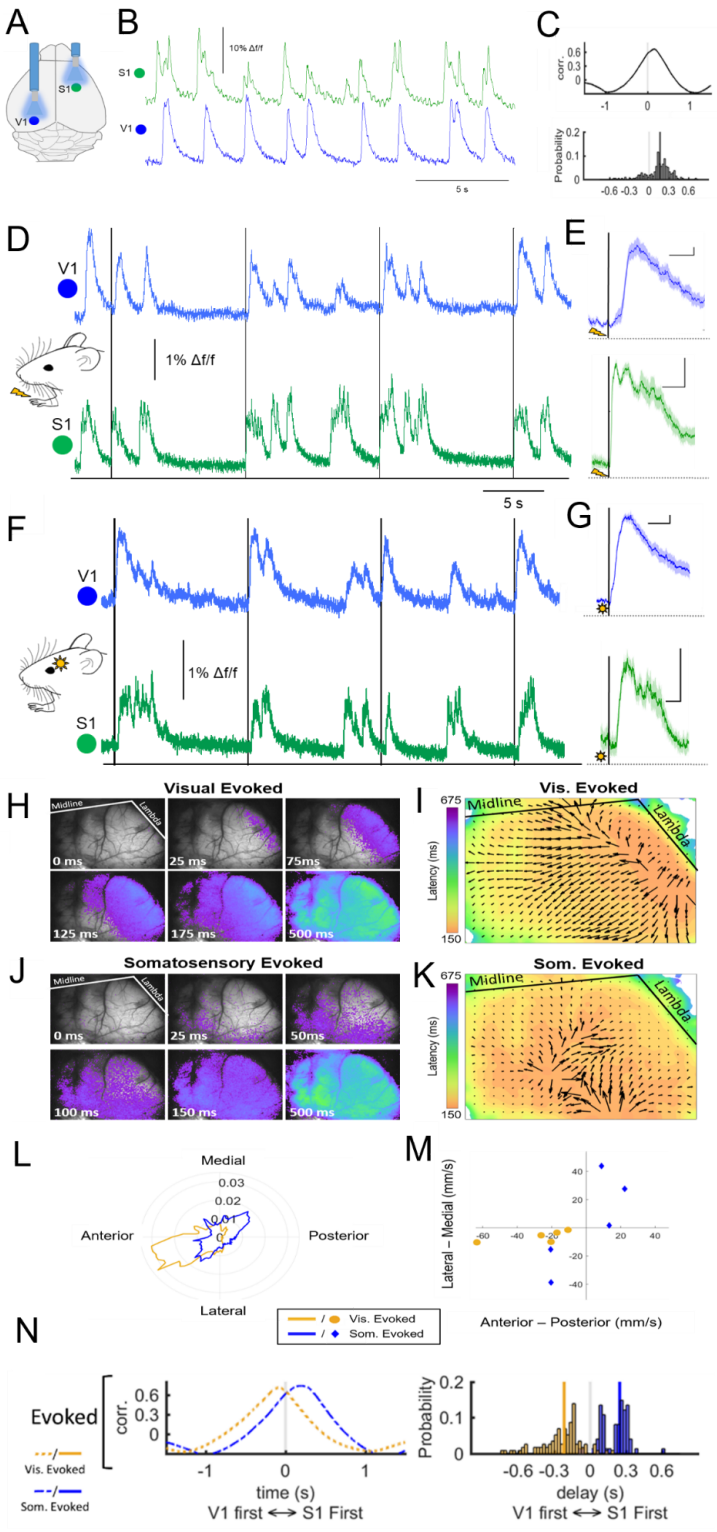

Figure 3. Sensory processing during SW state. (A) Optic-fiber based calcium signals were measured in contralateral S1 and V1 as depicted (or in ipsilateral S1 and V1). (B). Ongoing SW events are synchronized between the two recording sites, which is also visible in the cross-correlogram of the two depicted signals indicating that the posterior waves follow the anterior ones with variable delays (C). (D) Stimulus-evoked slow wave events start in the area of their respective sensory afferents and are detected with stereotypic delays in distant recording sites. Forepaw stimulation (10 ms pulses of 1 mA, ISI 10 s) reliably evokes slow wave events after 73 ms in S1 and after 290 ms in V1 in this mouse (averages of 20 events each). (E) Averages of stimulus-locked traces shown in (D) (line = mean, shading = SEM of 30 evoked events; vertical scale bars = 1 % Δf/f, horizontal scale bars = 500 ms). (F) Visual stimulation (10 ms LED light flash, ISI 10 s) leads to waves occurring after a mean delay of 114 ms in V1 and 340 ms in S1 in the same animal (averages of 20 evoked events). (G) Averages of traces shown in (C) (line = mean, shading = SEM of 30 evoked events; vertical scale bars = 1 % Δf/f, horizontal scale bars = 500 ms). (H) Still frames from a dfof movie depicting the propagation of a visually evoked wave, . (I) Quiver plot depicting pixel by pixel propagation velocities and direction for visual stimuli, K. (J) Still frame from a dfof movie depicting the propagation of a somatosensory evoked wave. (K) Quiver plot depicting the pixel by pixel propagation velocities and direction for J. Colormap indicates response latency for all pixels.. In (L) weighted polar distribution of propagation velocities for visual and somatosensory stimuli for all animals. (M) shows the vector mean propagation velocity and direction for each animal. (N) Correlation between V1 and S1 for evoked slow waves (left) and delay between V1 and S1 (right).

Given that fiber photometry only captures a small fraction of local cortical activity, we sought to better understand the relation between propagation patterns, sensory stimuli, and functional state with widefield calcium imaging. Using transgenic animals expressing GCaMP and thinned skull imaging techniques, we obtained high spatial resolution images of SW propagation throughout a majority of one hemisphere of the cerebral cortex at 20 – 40 Hz (Figure 4 H, I). Similarly, to what has been observed for the previously described dual-photometry measurements, waves appeared to initiate in the region corresponding to the sensory modality stimulated, then propagate across the cortex with stereotypic propagation direction and velocities (Figure 4 I-L). To quantify the differences in propagation direction between stimuli we compared the weighted distribution of velocity vectors (Figure 3L). Visually and somatosensory evoked responses differed significantly in their propagation direction distribution profile ($p<0.001$), indicating different propagation patterns. The average propagation (Fig. 3M) of visual evoked waves was consistently in the anterolateral direction whereas somatosensory evoked responses varied, with 3/5 propagating in the posteromedial direction and 2/5 propagating rostro-laterally. The velocities did not differ significantly when direction was disregarded ($p = 0.78$, students t-test) and had a combined mean of 30.5 ± 5.3 mm/s (n: 10). The specificity of initiation site and propagation direction but not velocity with respect to stimulus modality, suggest that the SW state is receptive to a range of incoming sensory inputs and favors the broad propagation of this signal across the cortex. To further understand the directionality of slow-wave propagation, we plotted the mean cross-correlation of Ca fiber signals from S1 and V1 for sensory-evoked stimuli (Figure 3N, left). The peak of the correlation has different sign depending on the stimulus, indicating visual vs somatosensory evoked slow-waves propagate in opposite directions. We directly quantify the delay between event onset in V1 vs S1 for evoked events (Figure 3N, right). The delays for somatosensory stimuli appear to include two populations. The less prevalent, shorter delay time could represent slow-waves evoked by another stimulus (i.e. auditory noise in the room) that occurred nearly simultaneously with a somatosensory stimulus, or some other brain activation due to the intense electrical stimulus. Overall, the S1 to V1 delay for somatosensory stimuli had a mean of 247ms (median: 247.0, IQR: 105–292, n: 74) ($P=0.009$), while the S1 to V1 delay for visual stimuli was significantly slower with mean -445ms (median: -218, IQR: -385 – -144; $p<0.001$).

Refractory properties of SW responses

Additionally, we observed an effect of sensory stimuli at different intervals following spontaneous slow waves (Figure 4 A, B), indicating that slow wave events show refractory periods as previously shown (Stroh et al 2013). Somatosensory-evoked response latencies were overall faster than those of visual responses. Responses in the cortical area associated with the stimulus were detected significantly sooner for somatosensory versus visual stimuli ($p<0.001$). To further understand the directionality of sensory evoked slow wave propagation, we plotted the mean cross-correlation S1 versus V1 for sensory-evoked stimuli (Figure 4 F, left; compare to spontaneously occurring slow wave events in Figure 1 C). The peak of the correlation has different sign depending on the stimulus, indicating visual versus somatosensory evoked slow waves to propagate in opposite directions. Spontaneous versus somatosensory evoked slow waves generally propagate in the same direction.

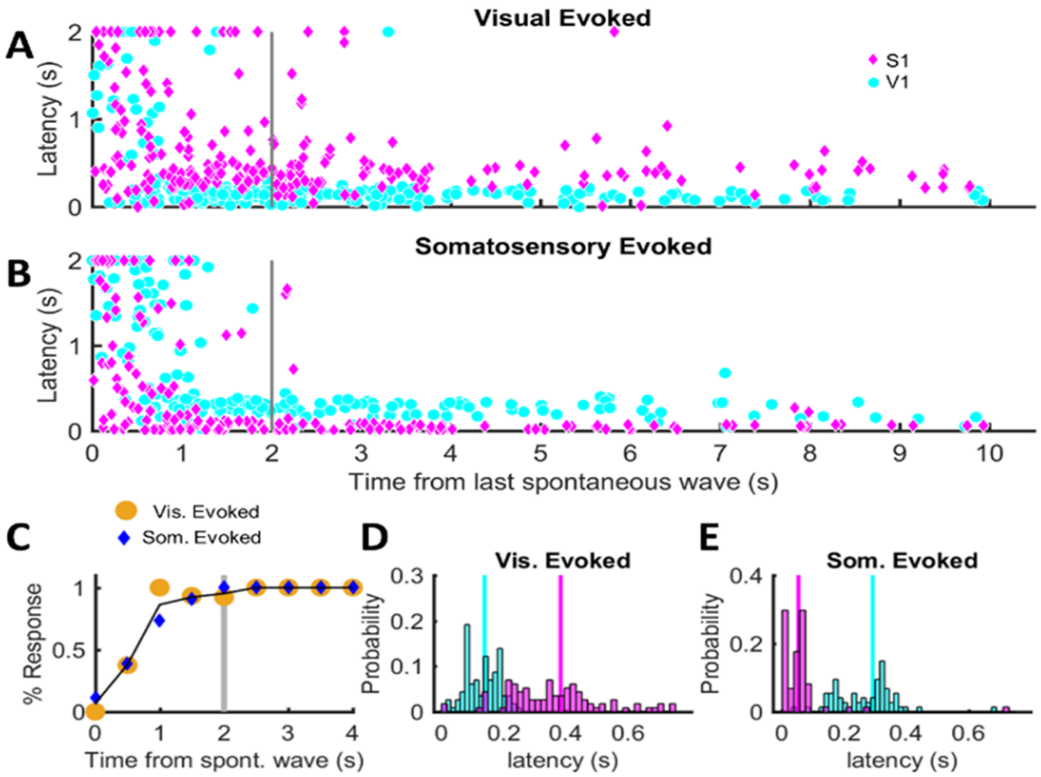

Figure 4. Effect of sensory stimuli at different intervals following spontaneous slow waves. (A, B) Latency to next detected slow wave and the time from last detected slow wave at time of stimulus. Variability in response time is reduced when stimuli are applied outside the refractory period (gray line), which is calculated in (C) as the time following a spontaneous slow-wave after which 90% of stimuli are followed by a slow-wave within 500s. (D, E) show latency of calcium responses in S1 and V1 from time of visual and somatosensory stimulation, respectively. Only stimuli arriving after the refractory period are included.

Primary responses in the corresponding sensory area precede a propagating global wave

We showed that slow wave activity is dominated by stereotypically reoccurring slow wave events. Although reliably elicited by peripheral stimulation, the microarchitecture of slow wave events and their stereotypical shape does not seem to encode stimulus features, which might be related to the engagement of large areas of the cortex during this state. Notably, and only in the in the primary area, corresponding to the sensory stimulation, we could observe a short-latency fast response, which was followed by a slow wave event (Figure 5 A). This 'primary response' was not present in the slow wave event detected in the distant sensory area, which suggests that although a local circuit of neurons might be activated encoding the sensory stimulus, not unlike a localized activation in persistent brain state, only the initiated slow wave is propagating across the cortex. These primary response component had been observed in previous studies in the auditory cortex (Grienberger et al., 2012), and can be recorded only in cases in which the recording fiber is placed directly upon the area of primary active neurons.

While calcium recordings are useful to describe the spatial extent of brain activity, their time resolution is slower than electrical recordings and unsuited to measure spectral content of sensory responses. As spectral analysis of electrical recordings is able to separate sensory response components, we used intracranial electrode implants to record local field potentials in V1 and S1 in response to visual stimuli. We compared the spectral content of responses to visual stimulation when the cortex was in the SW state or PA state. In addition, we also examined a subset of responses that occurred during the refractory window observed in the SW state. Example stimulus response averages and quantification in log(Fold Change) are shown in Figure 5 B, with summary values and statistics of the electrical response shown in Supplemental Tables 1,2. During the SW state we observed an initial high burst activity with broad spectral content delta thru gamma, which was time locked to the stimulus, (Figure 5 B, top left). This initial burst was then followed by a 2-3 second period of sustained elevation in delta through beta but not gamma activity. The timing of these two activity profiles align with the primary and secondary responses observed in fiber recordings (Figure 5 A). Upon examining the cortical area being stimulated, V1, we found that this primary fast response was present in both the SW and PA state as well as when during the refractory window of the SW state (Figure 5 B, left column, 'on stim'). This was also quantified by comparing the gamma power responses between these states in V1, which were all elevated in response to stimulation but did not differ significantly from each other (Figure 5 B, V1 'on stim'; Supplemental Tables 1, 2). We then examined the response to visual stimuli in somatosensory cortex (Figure 5 B right column, 'off stim'). In S1 we found that only the SW state allowed propagation of visual information across the cortex. In the SW state S1 exhibited a sustained lower frequency response similar to secondary response in V1, but not the higher frequency gamma response. Neither the primary nor secondary responses were observed in S1 during the PA state or in the refractory window of the SW state (Figure 5 A, B; Supplemental Tables 1,2). Collectively these findings suggest two independent phenomena that are differentially regulated by cortical state and are carried by cortical oscillations distinct in frequency and time course.

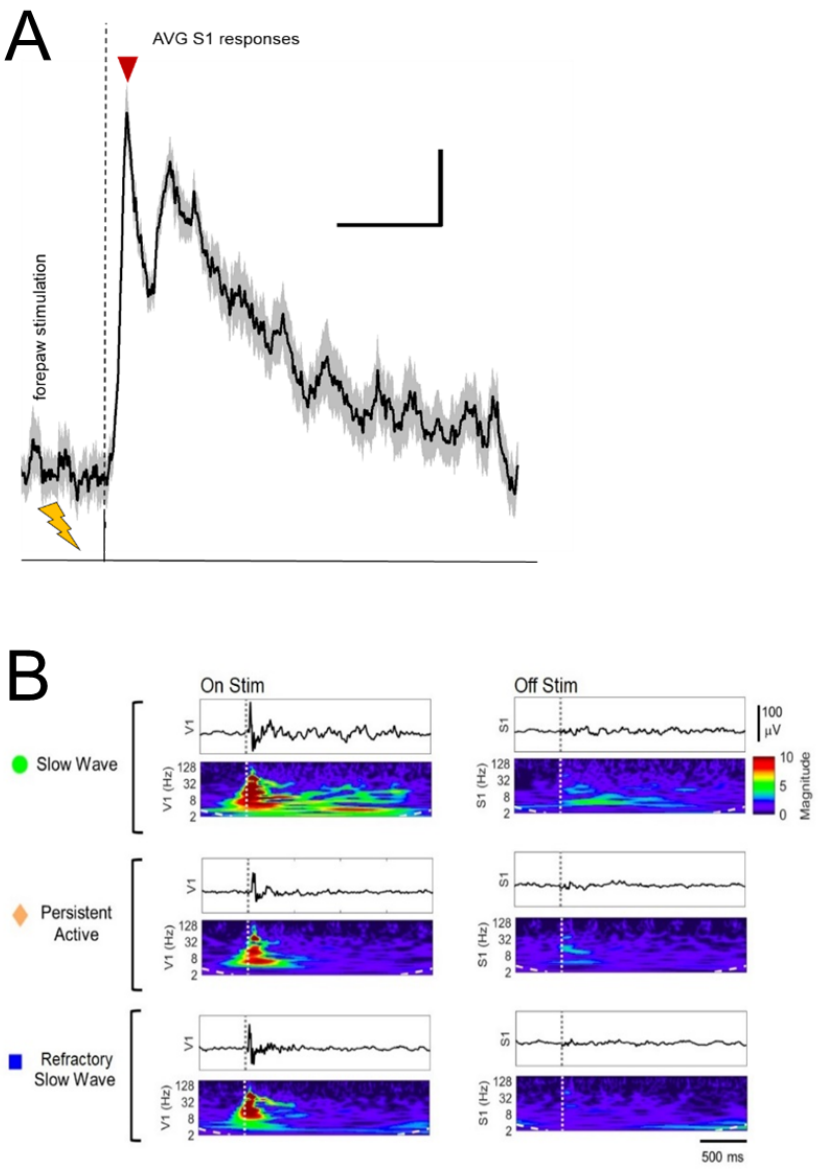

Figure 5. **Primary responses in the stimulus-encoding sensory area occur prior to the onset of an evoked SW event during SW activity.** A) Upon forepaw stimulation (yellow flash symbol) a primary response is detected in S1 (red arrow), followed by a slow wave event (averages of 30 events, black line = mean, grey shaded area = sem; vertical scale bar = 1 % Δf/f, horizontal scale bar = 500 ms). B) Electrical recordings of slow waves: stimulus triggered averages from V1 (left, 'On Stim') and S1 (right, 'Off Stim') in one animal under three conditions. Corresponding, spectrograms of responses displayed beneath each trace. Dotted line marks time of visual stimulus.

Discussion

It still remains unknown to what extent distinct functional states engage different areas of the brain and how they shape the representation of sensory afferents in the cortex depending on their spatial extension. Considering that state changes can take place under a variety of conditions, it is of importance to first characterize functional state as a variable by investigating the related ongoing neuronal signals across different cortical scales. Second, it is of interest to test how functional states shape the afferent output of the circuits they are dominating. Functional states generated through a modulation of internal activity, independent of environmental stimuli, may bring along different excitability modes of neuronal networks and are thereby likely linked to distinct processing of information by the brain. Hence, under anesthesia as well as in awake conditions, the current functional state of the cortical network provides a rich experimental variable, able to explain distinct properties of neuronal responses (McGinley 2016).

The presented findings indicate that the response of the cortical network to a sensory stimulus critically depends on the current functional state of the network. Sensory responses during SW versus PA state are more variable, with propagating waves often triggered by stimuli during SW state, but not during a refractory period following individual slow waves. Spectral analysis of electrical field potential recordings shows that gamma activity (> 40 Hz) is always observed in the cortical area associated with the stimulus. Together, these results support previous experiments showing elevated delta and theta activity during slow wave-generating states (Steriade et al., 1993; Constantinople and Bruno, 2011). In addition to SW state, we identify in these experiments a spatially constrained, gamma-based sensory response that occurs during PA state, but may be triggered by slow waves as well. Most importantly, we measure the traveling slow wave front with wide-field calcium imaging and find that the area of wave initiation and direction of propagation depends on the sensory modality stimulated.

Mesoscale Correlates of Functional States

Population activity measured via optical fiber recordings has allowed previous investigations of slow wave events in anesthetized animals (Stroh et al., 2013; Grienberger et al., 2012; Zhang et al., 2017). However, our lightly anesthetized recordings reveal a persistently active state where cortical activity occurs continuously, without the periods of quiescence that are characteristic of SW state. Upon peripheral somatosensory stimulation during SW activity, stereotypical calcium and LFP deflections were observed, which were time-locked to the stimulation pulses but similar to spontaneously occurring events regarding their properties. Evoked waves seem to follow all-or-none principles, which became particularly apparent observing the calcium and LFP signals upon a train of multiple stimulus pulses. During PA state, the same stimulus pulses lead to short-latency responses which precisely followed upon each single pulse and were, upon higher stimulation frequencies, prone to adaptation. As changes of functional state can occur spontaneously in awake as well as during prolonged anesthesia, they may appear as noise if they are disregarded in the statistical modeling of neural signals (McGinley et al., 2015b). When considered, changes of functional state can contribute to explain variability in experimental results under a variety of conditions.

Sensory responses in SW and PA state

As previously reported for auditory evoked slow waves (Grienberger et al., 2012) we observed two distinct components of sensory-evoked calcium responses: an early, fast-rising transient followed by a large, slow, long-latency calcium transient. The initial fast transient is missing in spontaneous and in optogenetically evoked calcium transients (Stroh et al., 2013; Grienberger et al., 2012) and is likely explained by thalamic afferents to lower layer 3, layer 4 and the layer 5/6 border (Romanski & LeDoux, 1993; Winer & Lee, 2007). The fast response was similar to the responses we observed during persistent activity and represents most probably the encoding of the stimulus, while the initiated wave propagates to distant cortical sites. Our results indicate that the direction of SW propagation is different if different sensory stimuli are used to stimulate waves. Given that visually evoked waves initiate posteriorly and propagate in anterior direction, while somatosensory stimuli initiate more anterior and to posterior sites, it appears that stimulation of different sensory modalities activates waves in associated cortices that are able to propagate depending on the refractoriness of other regions. The generally observed anterior-posterior propagation of slow waves (Massimini, 2004; Nir et al., 2011) may reflect that the dominant sensory pathways activated in wakefulness, and thus subsequently during slow-wave sleep, are located in more anterior regions.

Refractory period

EEG studies have indicated that slow waves may be activated locally and can propagate broadly depending on whether the brain is stimulated in-phase with the natural slow oscillation (Massimini, 2004; Nir et al., 2011). The current study indicates that the phase of the network activity reflects a propensity of the slow wave generating network towards refractoriness following active periods of the SW state. The dependence of SW generation on network history is likely to explain some of the wide variability of sensory responses observed when calcium imaging techniques are used to measure cortical activity in-vivo. Not only does the cortex display distinct states with different sensory response modes: the cortical response to stimuli can vary greatly within one state, depending on the sensory modality stimulated and history of activity in the network. Still, functional state may gate the secondary but not primary response to sensory stimulation as we observed a fast, high-frequency primary response encoded in its respective sensory area, and is independent of cortical state, followed by a secondary, slow and sustained low-frequency response that occurs and propagates only during SW state. These primary responses likely reflect incoming primary sensory information, presumably through thalamo-cortical projections. It is also interesting to note that the putative cortico-cortical activity appears to propagate via rhythms such as delta and theta which are highly associate with cortical synchrony in states like slow wave sleep.

In conclusion, we put forward the notion that the spatio-temporal characteristics of both sensory and stimulus-evoked responses in the cortex is governed by rather distinct functional states, putatively serving two distinct neurophysiological roles: Slow wave state facilitates cortex-wide information transfer, as required for memory consolidation in sleep, and persistent state allows for the selective, activation of modality-specific activation, required for a nuanced percept. Notably, as demonstrated by the joint occurrence of primary and secondary responses in this study in slaw wave state, and the findings of slow waves occurring the awake, aspects of these brain states can be identified in various conditions, slow wave and persistent states are not exclusive to awake or naturally sleeping condition. A brain-state informed analysis of

neurophysiological and neuroimaging data might therefore result in less variance, and a better understanding on the respective valence of a given activation patters, which is of particular relevance in translational studies.

Materials and Methods

Animals

All animals were housed under a 12 h light–dark cycle and provided with food and water ad libitum. Animal husbandry and experimental manipulation were carried out according to international standards and were approved either by the Landesuntersuchungsamt Rheinland-Pfalz, Koblenz, Germany or by the UW Institutional Animal Care and Use Committee.

Two different types of transgenic animals were used in these experiments. The first were triple-transgenic animals expressing cre/tet-dependent GCamp6f (Ai93, Jackson labs, stock #: 024103), as well as Cux2-Cre and Camk2-tet. The second group of animals expressed cre-dependent GCamp6s (Ai162, Jackson labs, stock #: 031562) and Emx1-Cre. It should be noted that there were survival issues with the second animals, likely due to tet-toxicity in response to excessive expression levels. However, a subset of animals grew up to healthy adults, and no differences were observed in the patterns of activity propagation vs the Ai93 animals. The increased calcium fluorescence in the Ai162 animal allowed faster image acquisition with increased signal-to-noise. For wide field experiments 5 animals were crosses of Cux2-Cre-Camk2-tet and Ai93, and 4 were Emx1-Cre and Ai162.

Dual-fiber Photometry

Mice were anesthetized with isoflurane mixed with pure oxygen to maintain surgical depth of anesthesia (3.0% induction, 1.5 – 2.0 % maintenance of anesthesia). Animals were fixed in a stereotactic frame with ear- and bite bars and placed onto a warming plate to keep body temperature constant at 37° C throughout the surgery. Anesthesia depth was repeatedly assessed by monitoring the tail-pinch reflex as well as the respiration rate of the animal. After application of topical anesthesia (xylocaine gel 2 %, AstraZeneca, Wedel, Germany) on the animal's head, a skin incision was made and the exposed area of the skull was cleaned and dried from fluids and blood. For anesthetized experiments involving recordings in somatosensory (S1) or visual cortex (V1), lateral muscles were partially removed with the help of a scalpel. Stereotactic coordinates of the regions targeted for virus injection, injection of the calcium dye or for imaging or recording, were located accordingly (coordinates for mice were taken from Paxinos & Franklin (2012) and a craniotomy was prepared under a dissecting microscope (Leica, Wetzlar, Germany) using a dental drill (Ultimate XL-F, NSK, Trier Germany, and VS1/4HP/005, Meisinger, Neuss, Germany). For calcium dye injections a small burr-hole was opened. The skull was removed using a sharp scalpel or a needle and the exposed area was moistened with phosphate buffered saline (PBS, Sigma, Munich, Germany) and the fluorescent calcium indicator Oregon Green Bapta-1 AM (OGB-1; Life Technologies/Molecular Probes, Waltham, USA) was prepared as previously described (Stosiek, Stroh) and bulk loaded into the somatosensory (S1; AP -0.2 mm, ML +/- 2.5 mm, DV -300 and -500 µm) and visual cortex (V1; AP -3.8 mm, ML +/–2.0 mm, DV -300 and -500 µm). Dye solution was delivered using a glass micropipette with an outer tip diameter of 45 µm and an inner diameter of 15 µm connected to a 10 mL syringe. Approximately

0.5 - 1.0 µl of the solution were slowly released at each injection depth by gentle manual pressure. After injection, the pipette was held in place for 2 min before slowly retracting it from the tissue. After a waiting period of 50 - 60 minutes to allow for ester cleavage, the cladding from the tip of a multimode optic fiber with a 200 µm diameter and 0.48 numerical aperture (Thorlabs, Grünberg, Germany) was removed and the fiber was inserted perpendicular to the dura above each recording site (S1 and ipsi- or contralateral V1). For anesthetized recordings mice were kept in the stereotactic frame and the fibers were held in place by two stereotactic arms. Mice for awake recordings either underwent a previous surgery three days before the experiments for implantation of a metal holder on the cranium or were implanted with such holder directly during the dye injection and fiber implants surgery. The metal holder was fixed on the skull with dental cement. For awake recordings fibers were glued to the skull using UV glue.

For excitation of the calcium indicator, we used custom-built setups either coupling a LED directly into an optic fiber (FOM and FOMII, NPI Electronic Instruments, Tamm, Germany). The light for excitation of the calcium indicators was delivered by a 650 mW LED with a nominal peak wavelength of 470 nm. LED power was controlled by an adjustable current source. The light beam was focused by means of a fixed focus collimator into one end of a multimode fiber which was connected to the system by an SMA connector. An aspheric lens was used to guide the emitted fluorescent light back through the same fiber where it was focused on a silicon photomultiplier photodetector with an active area of 3 x 3 mm2 and a photon detection efficiency of 20 % at 490 nm. The recorded fluorescence signals were digitized with a sampling frequency of 2 kHz using a multifunction I/O data acquisition interface (Power1401, Cambridge Electronic Design, Cambridge, UK) and its corresponding acquisition software (Spike2).

For excitation of the calcium indicator, we used constant illumination of (1.3 mW/mm2) at a wavelength of 470 or 488 nm which was switched on at the beginning and stayed on during the course of the measurement. For somatosensory stimulation under anesthesia, two needle electrodes were subcutaneously inserted into the forepaw (between digits 2 and 4), contralateral to the recording site, and connected to a constant current stimulator (DS5, Digitimer, Welwyn Garden City, UK). Stimulation pulses were of constant duration (10 ms) and strength (1 mA). Either single pulse stimulation or a block paradigm with a pulse train of 4 s at 3 Hz, followed by 10 s or 20 s baseline, was used. For visual stimulation in anesthetized or awake mice, a TTL pulse controlled small LED was used on the eye contralateral to the recording site. Depending

on the experiment, either single pulse stimulation (10 ms light pulses) or a block paradigm as described for somatosensory stimulation was used.

For awake recordings, after animals recovered from anesthesia on the tracking ball, the air flow controlling the Styrofoam ball was set to let animals run if they chose to initiate movement while they were head-fixed with a metal holder which was attached to a frame.

Calcium data preprocessing was performed with Igor Pro and were low-pass filtered before subsequent event detection if not stated otherwise. All depicted traces represent relative changes in fluorescence intensity (delta f/f). Events were treated as experimental units, given their stereotypical properties which are ubiquitously observed across animals. The descriptive statistics of the event properties distributions grouped by animals were very similar across individuals. Thus, calcium response statistics were pooled over events (mathematically equivalent to weighted averages), ensuring that every event is contributing equally to the

average, independent of its source (the individual animal). Data were tested for normal distribution using

the Lilliefors test, an assumption-free adaptation of the one-sample Kolmogorov-Smirnov test. In cases where normal distribution could be assumed ($p > 0.05$), the parametric two-tailed Student's t-test was employed to compare means (a p-value below 0.05 was considered significant). Where normal distribution could not be verified, the non-parametric Wilcoxon rank-sum test for equal medians was used to test median differences. All quantifications are presented as mean ± SEM, unless stated otherwise. In cases of an unstable baseline or absence of characteristic signal dynamics of slow wave-associated calcium transients (Grienberger et al., 2012; Stroh et al., 2013) calcium data was excluded from analysis. The time series trace from the fiber data was denoised using binomial (Gaussian) smoothing and normalized by dividing the original trace by the averaged baseline, for which one second of baseline was chosen manually. Latencies were quantified semi-automatically in each post-stimulus response. Cross-correlations of calcium signals were computed using the function crosscorr() in Matlab.

To determine the length of the refractory period, the rate of successful slow-wave generation in response to a sensory stimulus was calculated with respect to time elapsed from the previous spontaneous wave. This time was measured for each stimulus and binned into 0.5 second intervals. The first interval at which greater than 90% of sensory stimuli resulted in a slow-wave in the associated sensory cortex was calculated at 2 seconds. This calculation pooled somatosensory and visual stimuli across animals.

Widefield Imaging

For these experiments a titanium U-shaped head-holder was used instead of ear-bars. A craniotomy was performed to expose the skull, and the U-bar was positioned and glued to the surface of the skull with cyanoacrylate glue such that a majority of one hemisphere was exposed. The U-bar was held in place with an adjustable clamp, and a Dremel used to gently removed the flaky layers of the skull until blood vessels were clearly visible beneath the remaining skull when moistened. Then the skull was allowed to briefly dry and glue was applied to prepare the surface for imaging. The clamp was adjusted to present a level surface for imaging, and epifluorescent widefield imaging used to collect images of GCamp fluorescence emission at 10-40 Hz, with a Hamamatsu Orca Flash 2.8 CMOS camera and HCImage V4.4.0.11. We used an AD Instruments PowerLab 4/26 and LabChart V8 to trigger and synchronize stimuli to calcium records.

To analyze stimulus responses, we first spatially down-sampled and calculated the relative change in florescence over time ($\%\Delta f/f$) for each stimulus using the frame prior to stimulus onset as a reference frame. These responses were temporally aligned to stimulus onset and averaged to create stimulus triggered averages for each animal. To calculate response area, we used a threshold of 3.5 standard deviations of the averaged pre-stimulus signal to determine the onset of response (if any) on a pixel by pixel basis. We used the maximum number of pixels activated within 1-2 s to define the response area. To calculate propagation velocity and direction, we analyzed the difference in latency of neighboring pixels by creating a response time map and then taking the spatial gradient. To compare velocity between visual and somatosensory responses we combined the response vectors of all animals into a weighted polar distribution after manually aligning images to the midline suture. Distributions were compared using a Kuiper test available in the Circular Statistics Toolbox for MatLab (Berens, 2009). In addition,

we also quantified the mean velocity vector for somatosensory and visual responses by averaging all velocity vectors within each triggered average.

Local Field Potential Recordings

For LFP recordings a pipette with a tip resistance of 0.2M was filled with PBS and lowered into either the S1 or the V1 craniotomy at a depth of 300 µm. A grounding wire was implanted in the olfactory bulb. Signals were amplified using an extracellular amplifier (EXT-02F/2, npi Electronics, Tamm, Germany), filtered at 300 Hz (low pass), digitized at 2 kHz. Signals were analyzed using Spike2 software or custom-written Matlab scripts, including the Chronux toolbox (REF). Ongoing neuronal activity during different brain states or individual responses upon sensory stimulation were plotted against time to observe signal characteristics. Spectrograms showing time-frequency profiles were plotted with the Chronux package for multitapers using the following parameters: fpass= 0 – 40 Hz; Time-Bandwith-product = 4; Number of tapers = 9 and a moving window of 400 ms window size and 200 ms step size. For ongoing activity without stimulation the average for at least 60 s of recording was used, for stimulus-locked spectrograms the responses of 30 stimulus trials were averaged.

Further analysis was conducted on stimulus-triggered response averages from multiple animals. A minimum of 10 responses were averaged for each data point, with each data point representing one animal. Fold change in power was calculated by taking the average power of each response average from a time 0-1.5 seconds after the stimulus and dividing by the average power in a 200ms interval ending 100ms before the stimulus. For separation of slow-wave responses into refractory and non-refractory groups, an analysis of network history at the time of each stimulus was performed. The V1 electrical record was converted to power over time, and slow-wave onsets were detected where the power crossed 4 standard deviations above the mean. A stimulus response was considered to have occurred in the refractory period if spontaneous event onset was detected < 2 seconds prior to stimulus.

Anesthesia

To reach the functional state under investigation, different anesthesia protocols were used. Slow wave activity emerges under various anesthetics including ketamine-xylazine, propofol, midazolam, halothane, isoflurane, and urethane (e.g. Alkire et al., 2008; Chauvette et al., (2011); Murphy et al., 2011a; Sakata & Harris 2009), even though there are differences regarding the length of silent periods depending on the type and depth of the anesthesia used. For investigating slow wave activity, isoflurane was continuously supplied through custom-made anesthesia masks equipped with a tooth holder to reduce head movements. We used relatively high levels of isoflurane concentration to maintain slow wave activity (1.2 – 1.8 %) as we were aiming to achieve slow waves around 0.1 Hz. As depth of anesthesia is highly dependent on the physiological state of the animal, e.g. body- and therefore cortical temperature (Sheroziya & Timofeev, 2015; Schwalm & Easton, 2016), we relied on the online calcium or electrophysiological signal to ensure stable slow wave activity throughout the measurements and adjusted the isoflurane level accordingly, to achieve a rather uniform occurrence of slow waves. Consequently, while the absolute level of isoflurane anesthesia varied, based on many parameters such as length of anesthesia, we achieved rather constant conditions in terms of the characteristics of slow waves while the isoflurane concentrations were comparable with others (Chen et al., 2013b; Grienberger et al., 2012; Lissek et al., 2016; Luczak et al., 2007; Stroh et al.,

2013). Frequency of spontaneous waves is strongly dependent on the depth of anesthesia, ranging from about 10 waves/min at high anesthesia levels to 30 waves/min at low levels (Stroh et al., 2013). Further reduction of anesthesia leads to irregular patterns of activity indicating transition to a persistent state, which is usually reached at 0.4 - 0.6 % isoflurane. For maintaining a stable persistent network activity, we either used such low levels of isoflurane (0.4 - 0.6 %) or the sedative medetomidine (Dormitor 1 mg/mL, Pfizer, Orion Pharma, Espoo, Finland) as bolus injection of 0.05 mg/kg in mice and as bolus injection of 0.04 mg/kg followed by continuous subcutaneous infusion of 0.05 mg/kg/h for rats. For anesthesia controls we used ketamin/xylazin (ket/xyl; 180 mg/kg and 0.011 mg/kg respectively in NaCl solution). Physiological parameters as breathing rate and temperature were continuously monitored. Functional state was assessed with either of the reported recording techniques, and recording sessions in which functional state was unclear or varying, were excluded from the analysis.

Table 1 – Visual response properties

Frequency	Region	Brain state	mean log(FC)	median log(FC)	IQR log(FC)	N (animals)
Total Power (0.5-200Hz)	V1	SW	2.68	2.42	2.16–3.34	10
		SW-r	0.67	0.39	-2.6e-3–1.20	6
		PA	1.83	1.94	1.40–2.46	10
	S1	SW	2.00	1.78	1.26–2.78	10
		SW-r	-0.36	-0.43	-0.71– -0.19	6
		PA	0.61	0.52	0.38–1.02	10
Sub-Gamma (0.5-35 Hz)	V1	SW	2.69	2.69	2.12 – 3.12	10
		SW-r	0.56	0.31	-0.12 – -1.09	6
		PA	1.79	1.84	1.46 – 2.25	10
	S1	SW	2.06	1.80	1.24 – 3.03	10
		SW-r	-0.37	-0.54	-0.91 – -0.13	6
		PA	0.61	0.56	0.42 – 0.96	10
Gamma (35-200Hz)	V1	SW	2.20	2.26	1.19 – 2.90	10
		SW-r	1.53	1.58	0.76 – 2.02	6
		PA	2.08	2.17	1.20 –2.92	10
	S1	SW	1.16	0.80	0.52 – 1.66	10
		SW-r	-0.19	-0.29	-0.43 – 0.15	6
		PA	0.55	0.62	0.18 – 0.78	10

Table 2 – Visual response significance tests

Comparison		Sub-Gamma (0.5-35 Hz)	Gamma (35-200Hz)	Total
V1 vs S1 Wilcoxon signed-rank	SW	p=0.055	* p=0.020	* p=0.020
	SW-r	* p=0.031	* p=0.031	* p=0.031
	PA	** p=0.004	** p=0.002	** p=0.004
V1 Mann-Whitney U	SW vs PA	** p=0.008	p=0.968	** p=0.053
	SW-r vs SW	** p=0.002	p=0.456	** p=0.002
	SW-r vs PA	** p=0.011	p=0.368	** p=0.016
S1 Mann-Whitney U	SW vs PA	** p<0.001	p=0.243	** p<0.001
	SW-r vs SW	** p=0.012	p=0.328	** p=0.026
	SW-r vs PA	** p=0.011	** p=0.005	** p=0.011

References

Aedo-Jury, F., Schwalm, M., Hamzehpour, L., & Stroh, A. (2020). Brain states govern the spatio-temporal dynamics of resting-state functional connectivity. ELife, 9, 1–23. https://doi.org/10.7554/ELIFE.53186

Alkire, M. T., Hudetz, A. G., & Tononi, G. (2008). Consciousness and Anesthesia. Science, 322(5903), 876–880. https://doi.org/10.1126/SCIENCE.1149213

Boly, M., Coleman, M. R., Davis, M. H., Hampshire, A., Bor, D., Moonen, G., Maquet, P. A., Pickard, J. D., Laureys, S., & Owen, A. M. (2007). When thoughts become action: An fMRI paradigm to study volitional brain activity in non-communicative brain injured patients. NeuroImage, 36(3), 979–992. https://doi.org/10.1016/J.NEUROIMAGE.2007.02.047

Brown, R. E., Basheer, R., McKenna, J. T., Strecker, R. E., & McCarley, R. W. (2012). Control of sleep and wakefulness. In Physiological Reviews (Vol. 92, Issue 3, pp. 1087–1187). https://doi.org/10.1152/physrev.00032.2011

Busche, M. A., Kekuš, M., Adelsberger, H., Noda, T., Förstl, H., Nelken, I., & Konnerth, A. (2015). Rescue of long-range circuit dysfunction in Alzheimer's disease models. Nature Neuroscience 2015 18:11, 18(11), 1623–1630. https://doi.org/10.1038/nn.4137

Busse, L., Cardin, J. A., Chiappe, M. E., Halassa, M. M., McGinley, M. J., Yamashita, T., & Saleem, A. B. (2017). Sensation during Active Behaviors. Journal of Neuroscience, 37(45), 10826–10834. https://doi.org/10.1523/JNEUROSCI.1828-17.2017

Chauvette, S., Volgushev, M., & Timofeev, I. (2010). Origin of Active States in Local Neocortical Networks during Slow Sleep Oscillation. Cerebral Cortex, 20(11), 2660–2674. https://doi.org/10.1093/CERCOR/BHQ009

Chen, X., Rochefort, N. L., Sakmann, B., & Konnerth, A. (2013). Reactivation of the Same Synapses during Spontaneous Up States and Sensory Stimuli. Cell Reports, 4(1), 31–39. https://doi.org/10.1016/J.CELREP.2013.05.042

Constantinople, C. M., & Bruno, R. M. (2011). Effects and Mechanisms of Wakefulness on Local Cortical Networks. Neuron, 69(6), 1061–1068. https://doi.org/10.1016/J.NEURON.2011.02.040

Corsi-Cabrera, M., Pérez-Garci, E., Del Río-Portilla, Y., Ugalde, E., & Guevara, M. A. (2001). EEG Bands During Wakefulness, Slow-Wave, and Paradoxical Sleep As a Result of Principal Component Analysis in the Rat. Sleep, 24(4), 374–380. https://doi.org/10.1093/SLEEP/24.4.374

Dadarlat, M. C., Michael, X., & Stryker, P. (2017). Systems/Circuits Locomotion Enhances Neural Encoding of Visual Stimuli in Mouse V1. https://doi.org/10.1523/JNEUROSCI.2728-16.2017

Destexhe, A., Hughes, S. W., Rudolph, M., & Crunelli, V. (2007). Are corticothalamic "up" states fragments of wakefulness? In Trends in Neurosciences (Vol. 30, Issue 7, pp. 334–342). https://doi.org/10.1016/j.tins.2007.04.006

Eggermann, E., Kremer, Y., Crochet, S., & Petersen, C. C. H. (2014). Cholinergic Signals in Mouse Barrel Cortex during Active Whisker Sensing. Cell Reports, 9(5), 1654–1660. https://doi.org/10.1016/J.CELREP.2014.11.005

Grienberger, C., Adelsberger, H., Stroh, A., Milos, R.-I., Garaschuk, O., Schierloh, A., Nelken, I., & Konnerth, A. (2012). Sound-evoked network calcium transients in mouse auditory cortex in vivo. The Journal of Physiology, 590(4), 899–918. https://doi.org/10.1113/JPHYSIOL.2011.222513

Li, C. T., Poo, M., & Dan, Y. (2009). Burst Spiking of a Single Cortical Neuron Modifies Global Brain State. Science, 324(5927), 643–646. https://doi.org/10.1126/SCIENCE.1169957

Lissek, T., Obenhaus, H. A., Ditzel, D. A. W., Nagai, T., Miyawaki, A., Sprengel, R., & Hasan, M. T. (2016). General Anesthetic Conditions Induce Network Synchrony and Disrupt Sensory Processing in the Cortex. Frontiers in Cellular Neuroscience, 0(APR), 64. https://doi.org/10.3389/FNCEL.2016.00064

Massimini, M., Huber, R., Ferrarelli, F., Hill, S., & Tononi, G. (2004). The Sleep Slow Oscillation as a Traveling Wave. Journal of Neuroscience, 24(31), 6862–6870. https://doi.org/10.1523/JNEUROSCI.1318-04.2004

Matsui, T., Murakami, T., & Ohki, K. (2016). Transient neuronal coactivations embedded in globally propagating waves underlie resting-state functional connectivity. Proceedings of the National Academy of Sciences, 113(23), 6556–6561. https://doi.org/10.1073/PNAS.1521299113

McGinley, M. J., David, S. V., & McCormick, D. A. (2015). Cortical Membrane Potential Signature of Optimal States for Sensory Signal Detection. Neuron, 87(1), 179–192. https://doi.org/10.1016/J.NEURON.2015.05.038

McGinley, M. J., Vinck, M., Reimer, J., Batista-Brito, R., Zagha, E., Cadwell, C. R., Tolias, A. S., Cardin, J. A., & McCormick, D. A. (2015). Waking State: Rapid Variations Modulate Neural and Behavioral Responses. Neuron, 87(6), 1143–1161. https://doi.org/10.1016/J.NEURON.2015.09.012

Messer, M., Backhaus, H., Fu, T., Stroh, A., & Schneider, G. (2020). A multi-scale approach for testing and detecting peaks in time series. Https://Doi.Org/10.1080/02331888.2020.1823980, 54(5), 1058–1080. https://doi.org/10.1080/02331888.2020.1823980

Murphy, B. L., Pun, R. Y. K., Yin, H., Faulkner, C. R., Loepke, A. W., & Danzer, S. C. (2011). Heterogeneous Integration of Adult-Generated Granule Cells into the Epileptic Brain. Journal of Neuroscience, 31(1), 105–117. https://doi.org/10.1523/JNEUROSCI.2728-10.2011

Murphy, M., Bruno, M.-A., Riedner, B. A., Boveroux, P., Noirhomme, Q., Landsness, E. C., Brichant, J.-F., Phillips, C., Massimini, M., Laureys, S., Tononi, G., & Boly, M. (2011). Propofol Anesthesia and Sleep: A High-Density EEG Study. Sleep, 34(3), 283–291. https://doi.org/10.1093/SLEEP/34.3.283

Nir, Y., Staba, R. J., Andrillon, T., Vyazovskiy, V. V., Cirelli, C., Fried, I., & Tononi, G. (2011). Regional Slow Waves and Spindles in Human Sleep. Neuron, 70(1), 153–169. https://doi.org/10.1016/J.NEURON.2011.02.043

Poulet, J. F. A., & Petersen, C. C. H. (2008). Internal brain state regulates membrane potential synchrony in barrel cortex of behaving mice. Nature 2008 454:7206, 454(7206), 881–885. https://doi.org/10.1038/nature07150

Rochefort, N. L., Buzás, P., Quenech'du, N., Koza, A., Eysel, U. T., Milleret, C., & Kisvárday, Z. F. (2009). Functional Selectivity of Interhemispheric Connections in Cat Visual Cortex. Cerebral Cortex, 19(10), 2451–2465. https://doi.org/10.1093/CERCOR/BHP001

Romanski, L. M., & LeDoux, J. E. (1993). Information Cascade from Primary Auditory Cortex to the Amygdala: Corticocortical and Corticoamygdaloid Projections of Temporal Cortex in the Rat. Cerebral Cortex, 3(6), 515–532. https://doi.org/10.1093/CERCOR/3.6.515

Sakata, S., & Harris, K. D. (2009). Laminar Structure of Spontaneous and Sensory-Evoked Population Activity in Auditory Cortex. Neuron, 64(3), 404–418. https://doi.org/10.1016/J.NEURON.2009.09.020

Sanchez-Vives, M. V., Massimini, M., & Mattia, M. (2017). Shaping the Default Activity Pattern of the Cortical Network. Neuron, 94(5), 993–1001. https://doi.org/10.1016/J.NEURON.2017.05.015

Sanchez-Vives, M. V., & McCormick, D. A. (2000). Cellular and network mechanisms of rhythmic recurrent activity in neocortex. Nature Neuroscience 2000 3:10, 3(10), 1027–1034. https://doi.org/10.1038/79848

Schwalm, M., & Easton, C. (2016). Cortical Temperature Change: A Tool for Modulating Brain States? ENeuro, 3(3), 608–610. https://doi.org/10.1523/ENEURO.0096-16.2016

Schwalm, M., Schmid, F., Wachsmuth, L., Backhaus, H., Kronfeld, A., Jury, F. A., Prouvot, P. H., Fois, C., Albers, F., Van Alst, T., Faber, C., & Stroh, A. (2017). Cortex-wide BOLD fMRI activity reflects locally-recorded slow oscillation-associated calcium waves. ELife, 6. https://doi.org/10.7554/ELIFE.27602

Sheroziya, M., & Timofeev, I. (2015). Moderate Cortical Cooling Eliminates Thalamocortical Silent States during Slow Oscillation. Journal of Neuroscience, 35(38), 13006–13019. https://doi.org/10.1523/JNEUROSCI.1359-15.2015

Sheroziya, M., & Timofeev, I. (2015). Moderate Cortical Cooling Eliminates Thalamocortical Silent States during Slow Oscillation. Journal of Neuroscience, 35(38), 13006–13019. https://doi.org/10.1523/JNEUROSCI.1359-15.2015

Steriade, M., Amzica, F., & Nunez, A. (1993). Cholinergic and noradrenergic modulation of the slow (approximately 0.3 Hz) oscillation in neocortical cells. Https://Doi.Org/10.1152/Jn.1993.70.4.1385, 70(4), 1385–1400. https://doi.org/10.1152/JN.1993.70.4.1385

Steriade, M., Timofeev, I., & Grenier, F. (2001). Natural Waking and Sleep States: A View From Inside Neocortical Neurons. Https://Doi.Org/10.1152/Jn.2001.85.5.1969, 85(5), 1969–1985. https://doi.org/10.1152/JN.2001.85.5.1969

Steriade, M., Timofeev, I., & Grenier, F. (2001). Natural Waking and Sleep States: A View From Inside Neocortical Neurons. Https://Doi.Org/10.1152/Jn.2001.85.5.1969, 85(5), 1969–1985. https://doi.org/10.1152/JN.2001.85.5.1969

Steriade, M., Curr, F., & Nuiiez, A. (1991). Network Modulation of a Slow Intrinsic Oscillation of Cat Thalamocortical Neurons Implicated in Sleep Delta Waves: Cortically Induced Synchronization and Brainstem Cholinergic Suppression. In The Journal of Neuroscience.

Steriade, M., McCormick, D., & Sejnowski, T. (1993). Thalamocortical oscillations in the sleeping and aroused brain. Science, 262(5134), 679–685. https://doi.org/10.1126/SCIENCE.8235588

Steriade, M., Nunez, A., & Amzica, F. (1993). A novel slow (< 1 Hz) oscillation of neocortical neurons in vivo: depolarizing and hyperpolarizing components. Journal of Neuroscience, 13(8), 3252–3265. https://doi.org/10.1523/JNEUROSCI.13-08-03252.1993

Steriade, M., Nunez, A., & Amzica, F. (1993). Intracellular analysis of relations between the slow (< 1 Hz) neocortical oscillation and other sleep rhythms of the electroencephalogram. Journal of Neuroscience, 13(8), 3266–3283. https://doi.org/10.1523/JNEUROSCI.13-08-03266.1993

Steriade, M., Amzica, F., & Nurirez, A. (1993). Cholinergic and Noradrenergic Modulation of the Slow (~0.3 HZ) Oscillation in Neocortical Cells. JOURNALOF NEUROPHYSIOLOGY, 70(4).

Stroh, A., Adelsberger, H., Groh, A., Rühlmann, C., Fischer, S., Schierloh, A., Deisseroth, K., & Konnerth, A. (2013). Making Waves: Initiation and Propagation of Corticothalamic Ca2+ Waves In Vivo. Neuron, 77(6), 1136–1150. https://doi.org/10.1016/J.NEURON.2013.01.031

Timofeev, I., Grenier, F., & Steriade, M. (2001). Disfacilitation and active inhibition in the neocortex during the natural sleep-wake cycle: An intracellular study. Proceedings of the National Academy of Sciences, 98(4), 1924–1929. https://doi.org/10.1073/PNAS.98.4.1924

Vinck, M., Batista-Brito, R., Knoblich, U., & Cardin, J. A. (2015). Arousal and Locomotion Make Distinct Contributions to Cortical Activity Patterns and Visual Encoding. Neuron, 86(3), 740–754. https://doi.org/10.1016/J.NEURON.2015.03.028

Vyazovskiy, V. V., Cirelli, C., & Tononi, G. (2011). Electrophysiological correlates of sleep homeostasis in freely behaving rats. Progress in Brain Research, 193, 17–38. https://doi.org/10.1016/B978-0-444-53839-0.00002-8

Winer, J. A., & Lee, C. C. (2007). The distributed auditory cortex. https://doi.org/10.1016/j.heares.2007.01.017

Zhang, Q., Yao, J., Guang, Y., Liang, S., Guan, J., Qin, H., Liao, X., Jin, W., Zhang, J., Pan, J., Jia, H., Yan, J., Feng, Z., Li, W., & Chen, X. (2017). Locomotion-Related Population Cortical Ca2+ Transients in Freely Behaving Mice. Frontiers in Neural Circuits, 0, 24. https://doi.org/10.3389/FNCIR.2017.00024

Zucca, S., D'Urso, G., Pasquale, V., Vecchia, D., Pica, G., Bovetti, S., Moretti, C., Varani, S., Molano-Mazón, M., Chiappalone, M., Panzeri, S., & Fellin, T. (2017). An inhibitory gate for state transition in cortex. ELife, 6. https://doi.org/10.7554/ELIFE.26177

Supplemental Material

Supplemental Videos

Supplemental videos 1–6 are available in the repository at `https://github.com/dtabuena/FunctionalStates/tree/main/SupplementalVideos`.

Video Captions

Video 1 - Spontaneous Ca activity under in the Persistently Active state recorded in adult mouse cortex.

Video 2 - Spontaneous Ca activity under in the Slow Wave state recorded in adult mouse cortex.

Video 3 - Triggered average of the Ca responses after visual stimulation with and LED flash in the persistently active state.

Video 4 - Triggered average of the Ca responses after visual stimulation with and LED flash in the the slow wave state.

Video 5 - Triggered average of the Ca responses after somatic electrical stimulation of the hind paw in the persistently active state.

Video 6 - Triggered average of the Ca responses after somatic electrical stimulation of the hind paw in the slow wave state.

Supplemental Figures

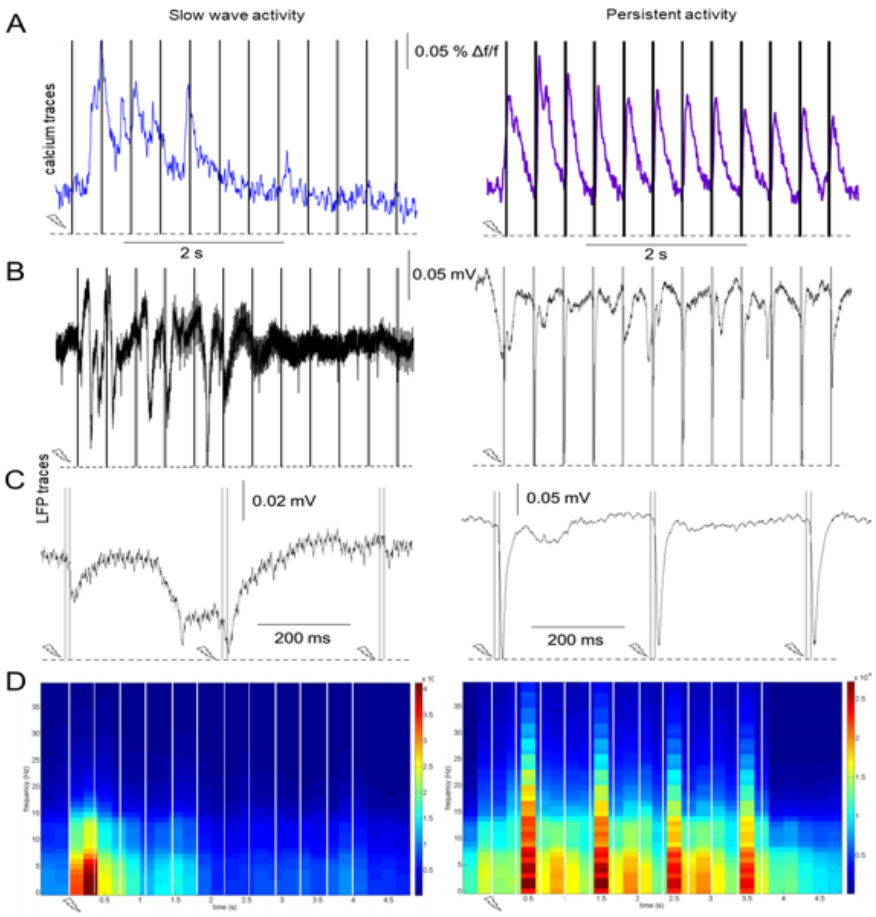

Supplementary Figure 1. Local dynamics of functional states during sensory-evoked activity (stimulus trains). (A) During slow wave activity (blue, left trace) stimulus trains of 3 Hz, 4 s lead to calcium waves comparable to the ones evoked by single pulses (cp. Figure 3.3 B). During persistent activity (purple, right trace) short-latency responses are elicited by every stimulus pulse of the train upon the same stimulation paradigm. (B) LFP recordings reveal similar signal characteristics upon 3 Hz 4 s stimulation as in above calcium, a stereotypic slow wave event is elicited during slow wave activity (left) whereas persistent activity is characterized by short-latency LFP spikes upon every pulse of the stimulus train (right). (C) A magnification of pulse 3-5 of the stimulus train in (B) shows that during slow wave activity a stereotypical wave event was elicited upon the stimulation, which is not responsive upon consecutive stimulus pulses, whereas during persistent activity every stimulus pulse was encoded by stimulus-locked LFP spike (right). (D) Stimulus-locked spectrograms reveal different response types upon 3 Hz 4 s stimulation paradigm for slow wave activity (left) and persistent activity (right) in their time-frequency profile.

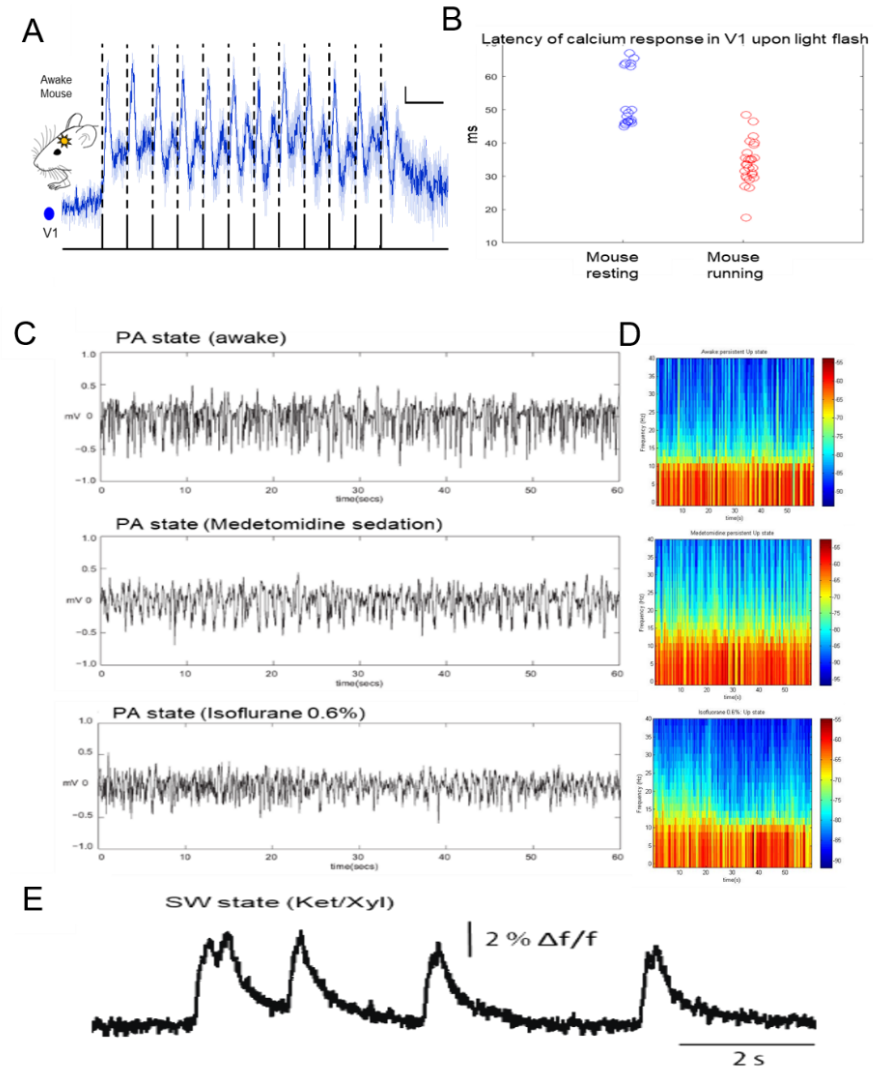

Supplementary Figure 2. Spatiotemporal dynamics in awake and sedated condition. (A) Responses occur locally in the area of respective sensory afferents in the awake mouse. Similar to the calcium responses in medetomidine sedated animals, visual stimulation leads to short-latency primary responses in the calcium signal of V1 (mean latency 25 ms ± 3 ms; 10 events) recorded in an awake mouse (averages of 10 stimulus trains of 3 Hz for 4 s events, line = mean, shading = SEM of 10 evoked events; vertical scale bars = 1 % Δf/f, horizontal scale bars = 500 ms). (B) Latency distributions of V1 calcium responses upon visual stimulation during rest and running. In this animal during a prolonged period of rest (> 30 s), visually evoked calcium responses in V1 (blue circles) occurred with a mean latency of 53 ms (± 2 ms; 18 events). When the animal was running on the tracking ball, visual stimulation evoked calcium responses in V1 with a mean latency of 34 ms (± 1 ms; 26 events). The medians of the distributions are statistically different (rank sum test, $p < 0.0001$). (C) and (D) different examples for PA state. (E) examples for SW state.

Pan-cortical waves in the neonatal mouse brain in vivo occur almost exclusively during sleep cycles

Dennis R. Tabuena[1,2], Randy Huynh[1], Jenna Metcalf[1], Thomas Richner[3], Albrecht Stroh[4], Bingni W. Brunton[1,3], *William J. Moody[1,3], Curtis R. Easton[1]

(in revision)

1. Department of Biology, University of Washington, Seattle, WA 98195
2. Graduate Program in Neuroscience, University of Washington, Seattle, WA 98195
3. University of Washington Institute for Neuroengineering, Seattle, WA 98195
4. Institute of Pathophysiology, University Medical Center of the Johannes Gutenberg-University Mainz & German Resilience Center, Hans-Dieter-Hüsch-Weg 19, D-55128 Mainz, Germany
* Corresponding author. profbill@uw.edu

Author contributions

DRT Designed research, Performed research, Analyzed data
RH Performed research
JM Performed research
TR Designed research, Performed research
AS Designed research, Analyzed data, Wrote the paper
BWB Performed research, Analyzed data
WJM Designed research, Analyzed data, Wrote the paper
CRE Designed research, Performed research, Analyzed data, Wrote the paper

Competing Interests

The authors have no competing interests to declare.

Acknowledgments

This work was supported by an NSF IOS BRAIN EAGER Grant, by the Simons Foundation for Autism Research Initiative, and by funds from the Royalty Research Fund of the University of Washington. DRT was supported by a Neuroscience Training Grant (T32NS099578) and by the Computational Neuroscience Training Grant.

Abstract

Spontaneous electrical activity plays major roles in the development of cortical circuitry. This activity can occur in highly localized regions or can propagate over the entire cortex, and both types of activity coexist during early development. To investigate how different forms of spontaneous activity might be temporally segregated, we used wide-field trans-cranial calcium imaging over an entire hemisphere in P1-P8 mouse pups. We found that waves of activity that propagate to cover the majority of the cortex (Pan-Cortical Waves) are generated at the end of the first postnatal week, along with several other forms of more localized activity. We further found that Pan-Cortical Waves are segregated into sleep cycles. Although present in P1 pups, their segregation into sleep is not complete until P6-P8. In contrast, cortical activity during wake states is more spatially restricted and the few large-scale forms of activity that occur during wake can be distinguished from Pan-Cortical Waves in sleep based on their initiation points in the cortex and their relationship to body movements. Cortical responses to whisker deflection

occupy a greater area of the cortex in sleep than in wake, indicating that functional cortical circuity in sleep generally favors more spatially widespread activity. This change in functional cortical circuitry to a state that is permissive for large-scale activity may temporally segregate different forms of activity during critical stages when activity-dependent circuit development occurs over many spatial scales. Our data also suggest that Pan-Cortical Waves in early development may be a functional precursor to slow sleep waves in the adult, which play critical roles in memory consolidation and synaptic rescaling.

Introduction

Many processes critical to the development of the cerebral cortex depend on spontaneous electrical activity (Blankenship and Feller, 2010; Kilb et al., 2011; Riyahi et al., 2021; Chang & Kanold, 2021). This activity occurs over a wide variety of spatial domains and serves, among other functions, important roles in establishing both local and long-range cortical circuitry (Easton et al., 2014; Barger et al., 2016; Mukherjee et al., 2017; Molnar et al., 2020; Rio-Berrmudez et al., 2020). Of particular interest is activity that propagates over very wide areas of the cortex, thus synchronizing firing in functionally very different cortical regions. This can take the form of spontaneous pan-cortical waves (Easton et al., 2014; Barger et al., 2016) or spindle bursts triggered by sensory feedback from myoclonic twitches (Rio-Berrmudez et al., 2020), both of which can synchronize activity between sensorimotor cortex and hippocampus.

All of this activity takes place on a substrate of rapidly developing cortical circuitry. The temporary neurons of the cortical subplate, for example, are major regulators of spontaneous firing at early stages (Molnar et al., 2020). In developing rats, the motor cortex not only does not initiate movements, but acts as a sensory structure, processing reafferent inputs resulting from myoclonic twitches (Gomez et al., 2021), and then later makes the transition to its primary adult function of initiating movement. Developing homeostatic mechanisms in cortical circuitry stabilize spontaneous firing rates in the face of large changes in sensory inputs (Riyahi et al., 2021), indicating the importance of intrinsic spontaneous mechanisms of cortical circuitry in regulating activity-dependent development.

A final important regulator of activity-dependent development in the brain appears to be state changes in functional circuitry represented by the fragmented immature sleep-wake cycles. The rodent state-dependent EEG, as indicated by the presence of sleep spindles, does not mature until the end of the second week, although behavioral sleep, indicated by atonia, is present well before that time (Blumberg et al., 2020). Nonetheless, sleep-wake cycles in the first postnatal week still regulate many developmental processes, such as responses of the visual cortex to retinal waves (Mukherjee et al., 2017) and the development of interactions between M1 and S1 circuits (Gomez et al., 2021; for review, see Blumberg et al., 2020).

Although many forms of spontaneous activity disappear during early development because their persistence would disrupt the mature functioning of the circuitry whose development they regulate, pan-cortical waves appear to persist in the form of slow sleep waves (Massimini et al., 2004; Lissek et al., 2016; Feher et al., 2021), where they are important in memory consolidation (Salfi et al., 2020; Skelin et al., 2021). Because many mechanisms of synaptic plasticity are shared between learning and development, we asked whether the sleep state of the immature rodent brain might be permissive for the generation of pan-cortical waves. If true, the segregation of large-scale waves into sleep might serve to temporally separate forms of spontaneous activity that are generated over very different spatial scales, thus minimizing mutual interference.

To test this hypothesis, we recorded cortical activity over an entire hemisphere, using trans-skull calcium imaging in unanesthetized GCaMP-expressing mice undergoing spontaneous sleep-wake cycles. Our results show that pan-cortical waves emerge during the first postnatal week, and they are indeed almost completely segregated into sleep bouts. These waves can be distinguished from large-scale activity during the wake state by their points of origin and by the fact that they occur in the absence of body movements. Quantitative analysis of the patterns of cortical activity using pixel-by-pixel correlation maps and non-negative matrix factorization confirmed that widespread spatial modes of activity are highly associated with sleep. These pan-cortical sleep waves can be prevented by transient sleep deprivation. Finally, we found that this form of large-scale sleep-related activity appears after birth, during the first postnatal week, after behavior sleep emerges.

Our results further confirm the central importance of sleep in brain development (Blumberg et al., 2020), and indicate that the sleep state may serve analogous functions in supporting long-range synaptic strengthening in the developing and the mature brain.

Results

Pan-Cortical Waves in P6-P8 Pups

We recorded cortical activity over a single hemisphere from 8 P6-P8 pups expressing GcaMP6s under control of the gene for the vesicular glutamate transporter 1 (Vglut1). Thus, our signal measures activity in the population of glutamatergic neurons of the cortex. These recordings totaled 591 minutes during which we detected 893 Sleep/Wake cycles, as determined by k-means sorting of the power spectrum of the nuchal EMG. Each experiment also included video of the animal so we could determine body movements associated with various forms of activity. Because our primary interest was in measuring large-scale wave activity, we found that calculating and plotting the fractional area of the imaged hemisphere engaged in activity (‘area fraction’) proved to be a useful metric for visualizing and analyzing wave events. (See Methods for details.)

In these recordings, we observed periodic wave-like events that initiated in a variety of locations and propagated over very large fractions of the hemisphere, often invading that portion of the contralateral hemisphere visible in our field of view (Fig. 1 A,B, Sup. Movies 1,2). Probability distributions of peak area fraction for 2288 events (all events with area fractions > 0.02), separated by whether the peak of the event occurred during sleep or wake, are shown in Fig. (1C, D). In sleep, event amplitudes are fit by a single exponential, indicating a single population of events, whereas in wake, there was a clear second population of large-scale events covering > 50% of hemisphere area. This was confirmed by probability histograms of all data points, expressed as either normalized $\Delta F/F$ or area fraction (Fig. S1). These distributions indicate that in the sleep state, a mechanism exists for the generation of a unique form of widely-propagating waves of activity. We refer to these as Pan-Cortical Waves. Below, we investigate the properties of these waves. We further show that, although waves of activity covering > 50% area fraction do occur in the wake state, these can be distinguished from Pan-Cortical Waves by several criteria.

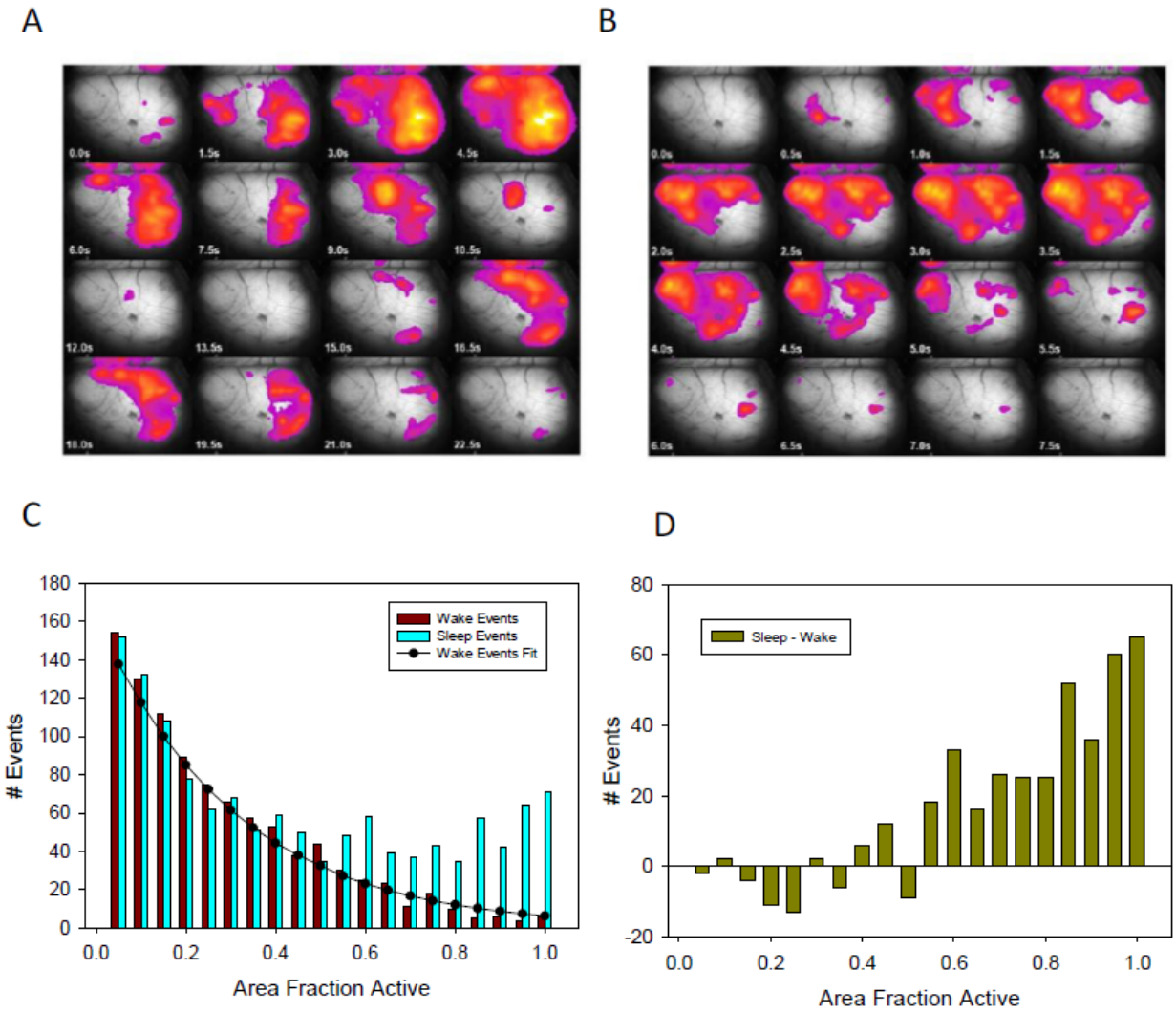

Figure 1. Spontaneous pan-cortical waves in a P8 mouse pup. A,B: Montages of Fluorescence images of the left hemisphere showing two spontaneous pan-cortical waves. Anterior is to the Left and the midline is visible near the upper edge of each frame. Time stamps are seconds. C: Frequency histogram of the fraction of the hemisphere area occupied by activity at the peak of all events in all animals > 2% active area, separated by sleep (cyan) and wake (brown) states. Best regression fit of wake data is also shown. Note that wake event amplitudes are well fit by a single distribution whereas sleep events show a separate population of large-area events covering > 50% of the hemisphere area. D: Difference plot (Sleep – Wake) from C, showing the large-area events characteristic of sleep.

Pan-Cortical Waves occur primarily during sleep and differ from large-scale activity during wake

Figure 2A shows 7 minutes of continuous recording from a P8 pup, with nuchal EMG, sleep-wake indicator based on k-means sorting of the EMG power spectrum (wake = high), area fraction of activity, and body movement taken from the video of the pup. Waves are easily visible as periods with high cortical area of activation lasting several seconds. Comparing the area fraction trace with the other parameters reveals two trends in the data. First, Pan-Cortical Waves occur during mainly periods classified as sleep. This relationship is seen throughout the records, but is highlighted in Insets B and C, where both brief (B) or prolonged (C) wake cycles cause and immediate reduction in the spatial extent of activity (area fraction trace). The second trend seen in this record is that the relation between activity and movement (bottom trace) inverts between sleep and wake. This is also apparent in inset C, where sleep, as indicated by atonia interrupted by brief myoclonic twitches, is associated with a large area fraction of activity. Upon waking, large and prolonged body movements, as indicated by both the EMG and movement traces, are associated with a smaller area fraction of activity. A video of a 5-min continuous recording of calcium signal and EMG showing multiple sleep-wake cycles and sleep-associated waves is shown in Supplemental Movie 3.

To further investigate these trends, we analyzed 510 Pan-Cortical Waves that initiated and reached peak amplitude within the same behavioral state. Of these, 434 (85%) occurred during sleep, even though animals spent almost identical amounts of time in sleep and wake states (50.39 + 4.63% sleep). Mean wave frequency in sleep was 1.41 + 0.09 / min, almost six times higher than wave frequency in wake (0.25 + 0.06; $p < 0.001$). As a result of this segregation of Pan-cortical Waves into sleep, the mean fractional hemisphere area involved in activity, measured over all times, was three-fold higher in sleep (0.14 + 0.01) than in wake (0.048 + 0.006; $p<0.001$).

The probability distributions in Fig. 1C,D and the different relationship between area fraction and movement seen in Fig. 2A suggest that large scale activity in wake could be distinguished from true Pan-Cortical Waves in sleep by the fact that the latter would be associated with smaller body movements. To test this, we examined the relationship between cortical activity and body movements for 174 events which covered > 50% hemisphere area and for which the entire event from 5% area fraction onset to decay to 5% area fraction occurred within a single behavioral state. For each event we integrated the fractional area record and the associated rectified difference-frame video record (see Methods for details). We then took the ratio of area/movement as a measure of the dependence of the spatial extent of cortical activity on movement. This ratio was nearly 50-fold higher for sleep events (353.9 + 163.7) than for wake events (8.05 + 2.19; $p<0.001$). As shown in Fig. 2D, this criterion can identify large-scale cortical waves as occurring in sleep with 96% accuracy (130/136) or in wake with 71% accuracy (27/38). This indicates that large-scale cortical activity in sleep is not associated with body movements whereas in wake this association is very strong.

The second criterion that can distinguish large-scale waves that occur in sleep vs. wake is the initiation point of the wave. We calculated the probability of predicting whether a given event occurred during wake or sleep given its initiation site. We found that if activity began anywhere except a small region near the early motor area it was almost certainly initiated during sleep whereas any activity beginning in this motor area was almost certainly occurring during wake (Fig.2 E,F).

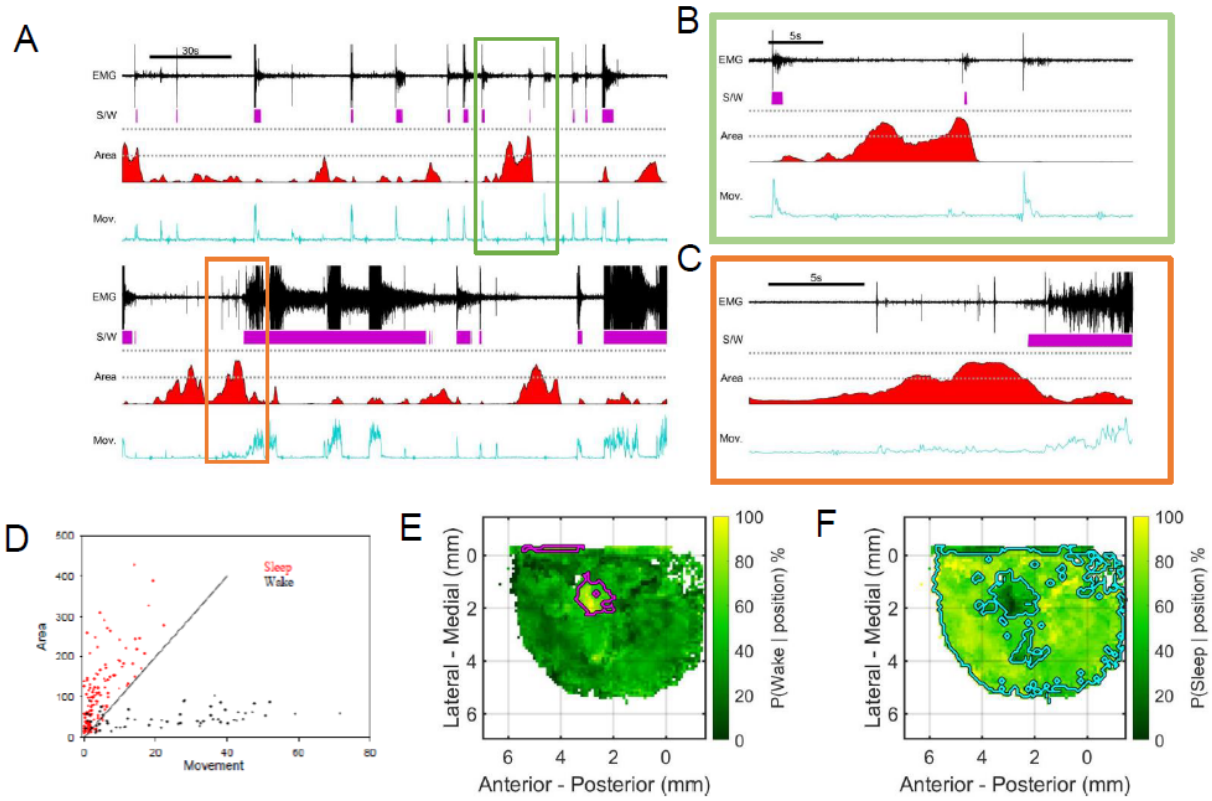

Figure 2. Pan-cortical waves occur primarily during sleep. A: 7-minute continuous recording from a P6 pup. Trace represent (top – bottom): Black – nuchal muscle EMG; Magenta – Sleep/wake indicator (high = wake); Red – Area fraction of hemisphere covered by activity; Cyan – body movement, derived from frame-difference film of animal. B,C: Insets from times indicated by squared in A. Note correlation of sleep and lack of body movement with high-area activity and onset of brief or prolonged wakefulness is correlated with reduced activity area. D: Scatter plot of fraction hemisphere are active vs. body movement (integral of frame difference trace as shown in A), for events >50% area coverage. Sleep events in red, wake events in black. Note the clear separation of sleep and wake events by the line shown: Large sleep events are correlated with much smaller body movements than wake events. E,F: Probability map indicating the chance the pup is awake or asleep (respectively) given where activity began in aligned mm coordinates. Regions where the probabilities are significantly different are bounded cyan traces for sleep and magenta for wake. Note that for F the majority of the cortex is bounded by cyan with pockets of lower probability which are not significantly elevated,shaded in dark green. Significance was determined using permutation based test with n = 8.

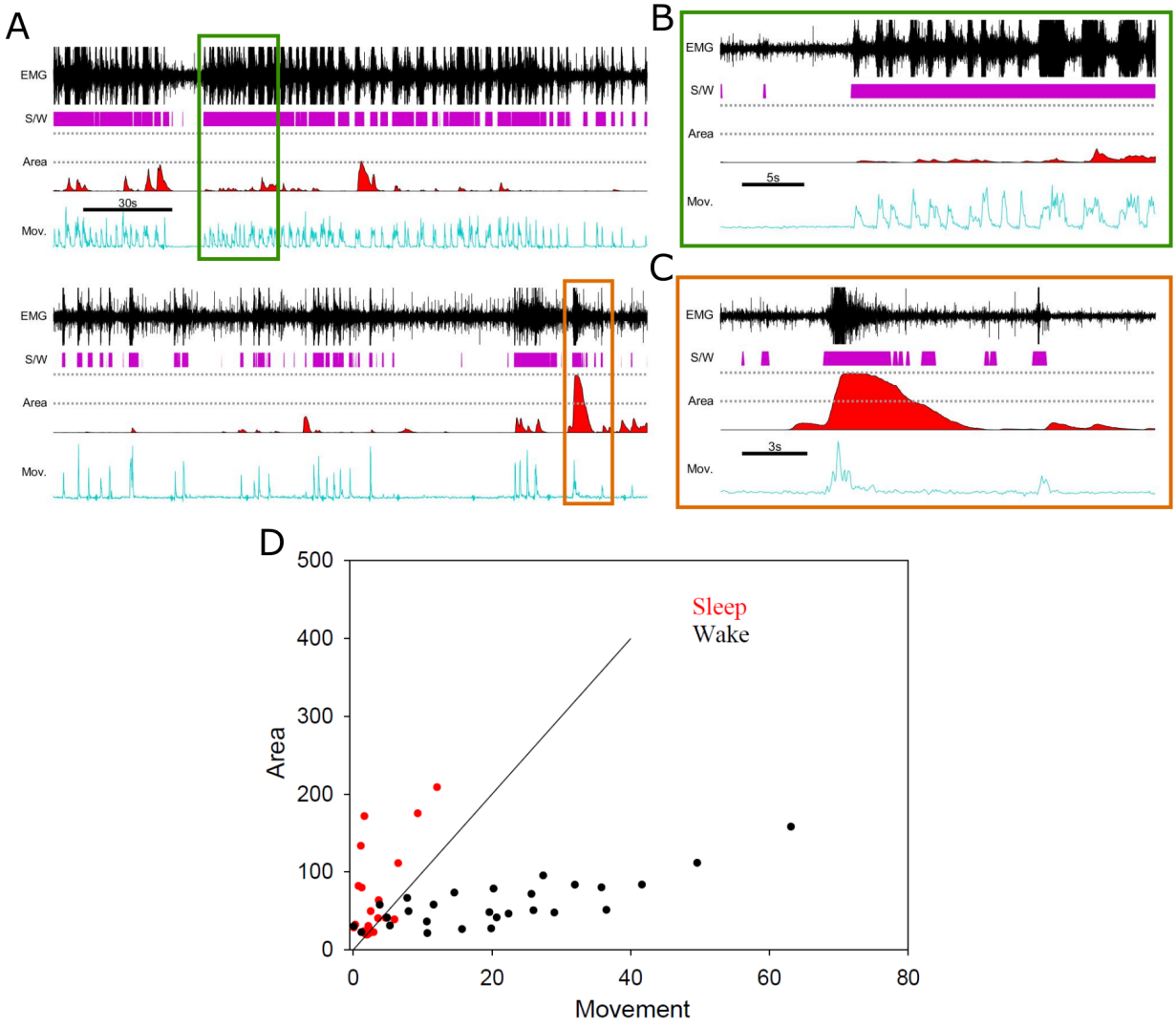

Figure 3. Relationships of pan-cortical waves and increased functional connectivity to sleep is much weaker at P1 than at P6-P8. A: 7-minute continuous recording from a P1 pup, traces as in Fig. 2. B,C: Expanded portions of records indicated by boxes in A. Note the lack of correlation of large-scale waves with sleep. D: Scatter plot of waves > 50% area coverage, showing area coverage as a function of body movement, as in Fig. 2D. At P1, there is a correlation of waves with large body movements in wake, but not in sleep, as at P6-P8.

Pan-cortical waves are present at P1 but not fully mature

The above data were collected at the end of the first postnatal week (P6-P8). We next asked whether the association of Pan-cortical Waves with sleep was present immediately after birth, on P1. As shown in Fig 3A-C there were large-scale waves of activity at P1, but no clear association of those waves with sleep states. In fact, at P1 only 44.6% of waves occurred in sleep, even though the fraction of time pups spent in sleep at P1 (62.5 + 4.65%) was not different that at P6-P8 ($p=0.22$). The frequency of waves in sleep (0.51 + 0.27) was smaller than that in wake (1.16 + 0.36, $p=0.02$), the inverse of the relationship at P6-P8. In addition, the inverse relationship between waves and body movement seen between sleep and wake waves at P6-P8, although still present at P1, was much less pronounced. Using the same area/movement ratio as above, the mean value for sleep waves was only about 3-fold higher than for wake waves (43.6 + 13.5 vs. 14.1 + 10.0, $p<0.001$) compared to the 50-fold difference at P6-P8. As shown in Figure 3D, a scatter plot of area vs. movement for P1 animals could still distinguish sleep from wake waves using the same criterion as for P6-P8 animals, at approximately the same level of accuracy (89% for sleep wave, 82% for wake waves). These data indicate that as early as P1, mechanisms driving changes in functional cortical circuitry between sleep and wake have at least partially matured and that sleep-related large-scale waves of activity could be driving activity-dependent mechanisms of neural circuit development at this early stage.

Functional connectivity in the cortex favors widespread activity in sleep at P6-P8

A common simple measure of functional connectivity is to compare correlation coefficients of activity across different regions of the brain. Based on this we used our calcium imaging records to compare correlation coefficients for pixel across the entire visible cortex (Fig 4). To calculate this metric, each video recording was separated in to dFoF time series data for each pixel, and calculated the covariance matrix for each recording for periods of sleep and wake. To analyze this difference across multiple recordings of different pixel counts, we calculated the median correlation coefficient for each pixel to others in a trace (the median of each row in each covariance matrix) to summarize the coactivity for each pixel (R-score). Higher R scores indicate that a greater number of pixels show correlated levels of activity, indicated more spatially widespread connectivity. The mean probability distribution of R-scores in each recording for P6-8 pups and P1 pups is shown in Fig. 4A,B, respectively. In P6-8 pups we see a significant shift to higher R-score during sleep indicating increase communication across cortical areas. In contrast P1 pups the R-score distribution was highly variable and did not exhibit significant trends across behavior state.

To test whether this increase in functional connectivity of the sleep state in P6-P8 animals affects evoked as well as spontaneous activity, we measured the spatial extent of activity in the cortex elicited by whisker deflection during wake, and during sleep periods when Pan-cortical waves were not occurring. As shown in Fig. 4C,D, whisker responses during sleep covered a much larger area than those during wake (9.28+1.62% of hemisphere area vs. 3.24+0.74%; $p=0.004$). These data indicated a higher degree of large-scale spatial connectivity is a property of the sleep state and emerges between P1 and P6-8, even though behavioral sleep and some pan-cortical waves have emerged by P1.

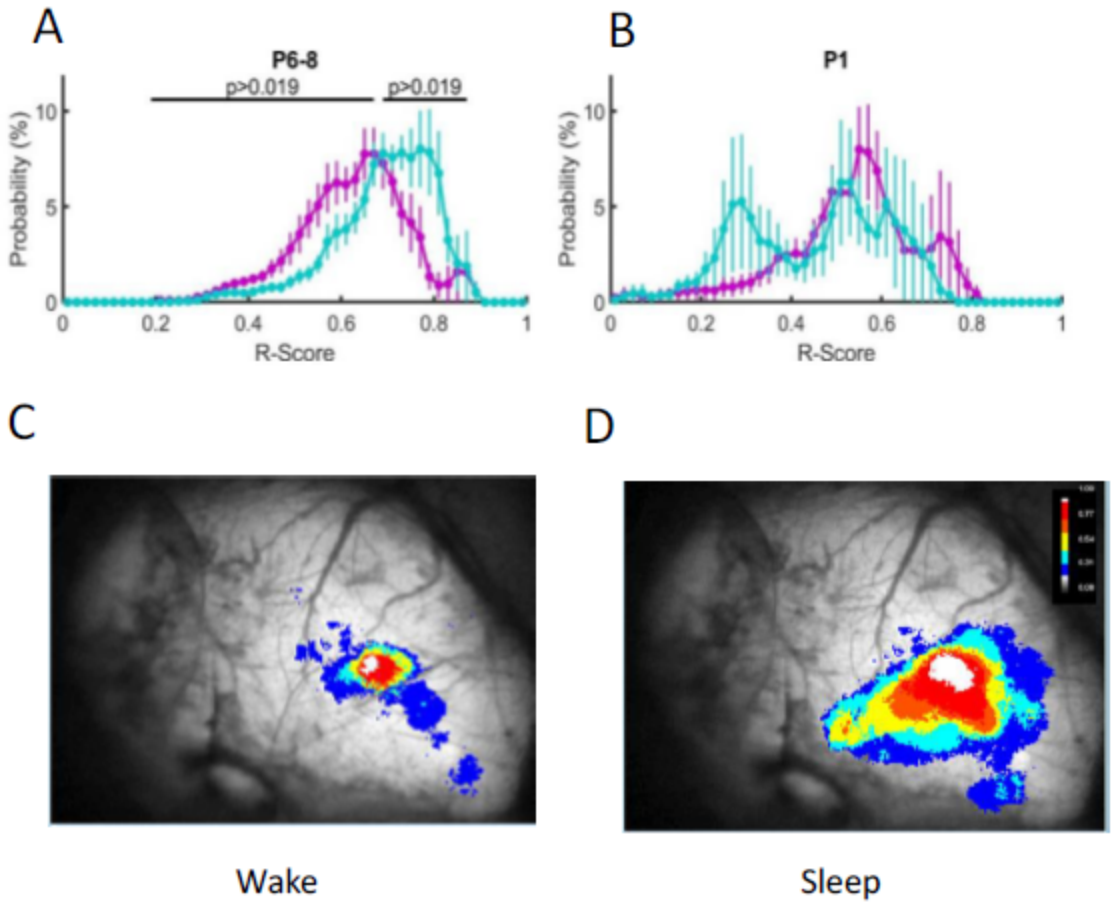

Figure 4. Increased functional connectivity associated with sleep at :6-P8, but not at P1. A,B: Median correlation of activity each pixel to other pixels in the record (R-Score; See text) compared between sleep and wake at P6-P8 (A) and P1 (B). In sleep at P6-P8, there is increased correlated activity across the hemisphere compared to wake. This is not seen at P1. C,D: Summed responses in barrel cortex to whisked deflection at P6-P8, displayed as probability of activity over repeated deflections, in wake (C) vs. sleep (D). Response area is much greater in sleep, indicating an increase in functional connectivity in sleep independent of wave generation. Whisker deflections that overlapped with wave generation were excluded from the analysis.

Quantification of sleep- and wake-related activity using Non-negative Matrix Factorization

To quantitatively compare the spatio-temporal patterns of cortical activity between sleep and wake states at both P6-8 and P1, we applied a dimensionality reduction method, Non-Negative Matrix Factorization (NNMF) (Berry et al., 2007), to the image sequences of activity. NNMF approximates the data contained within these sequences as a small number of static spatial modes ("Features"), each associated with a time vector ("Coefficients"). The original data are reconstructed to a given degree of accuracy by multiplying each feature matrix by its time vector and then adding the resulting feature image sequences. Each feature shows a set of pixels whose activity is repeatedly correlated during the time of the recording and its time vector shows when the correlated activity of those pixels occurs. The log2 ratio of the mode energy during sleep vs during wake (Sleep Score; see methods) using the time vector for each feature image quantifies how distributed the correlated activity of those pixels is between the sleep and wake states, with Sleep Scores >0 indicating greater prominence in sleep.

An example decomposition of calcium recording from a P8 aged pup into 20 features is shown in Fig. 5A with each panel depicting a spatial mode with its Sleep Score as derived from its associated coefficients vector. Example coefficients vectors to the top sleep- and top wake-ranked features are plotted in Fig. 5B. Most of the features occur preferentially in sleep (17/20), reflecting the high spatio-temporal complexity of activity caused by wave propagation from diverse initiation points in addition to many forms of more localized activity. In addition, sleep features have larger areas on average because of the spatially widespread synchrony of activity caused by the waves.

This was not the case for P1 pups (Fig. 6), where widespread activity was not necessarily more likely during sleep nor were the majority of components associated with sleep. Fewer features were required to describe activity at P1 (13 in the example shown, compared to 20 in the P8 example shown in Fig. 5). We quantified this by calculating the variance explained by decomposing each recording multiple times into numbers of features varying from 1 to 25 (Fig 6C), and then examining the relationship between feature number and the variance in the image stack explained. Significantly more features were required to describe similar variances at P6-P8 than at P1, confirming the greater complexity of cortical activity at P8. To further quantify the nature of this new complexity and increased mode bias to sleep we calculated the bivariate distributions of component area and sleep score for P6-8 and P1 animals (6D,E). We noted a significant shift in these distributions after the first week. A new population of modes with wider spread (20-40% coverage of the cortex) and higher association with sleep emerge (see difference distribution in Fig. 6F).

Forced waking confirms the causal relationship between sleep and Pan-cortical Waves

All of the above data were obtained from spontaneous sleep-wake cycles. To show a causal relationship between sleep and Pan-cortical waves, we developed a closed-loop system to cause brief periods of sleep deprivation, wherein real-time detection of sleep based on the EMG power spectrum triggered a mechanical stimulus to the snout of the pup to cause it to wake. Periods of stimulus-induced sleep deprivation were clearly associated with a low incidence of Pan-cortical waves, much as were periods of spontaneous wakefulness (Fig. 7A). In addition, stimulus-induced waking during a Pan-cortical wave caused the wave to terminate much as was the case for spontaneous waking. (Compare, e.g., spontaneous waking after the first sleep wave in Fig. 7B to stimulus-induced waking during each of the two sleep waves in Fig. 7C.).

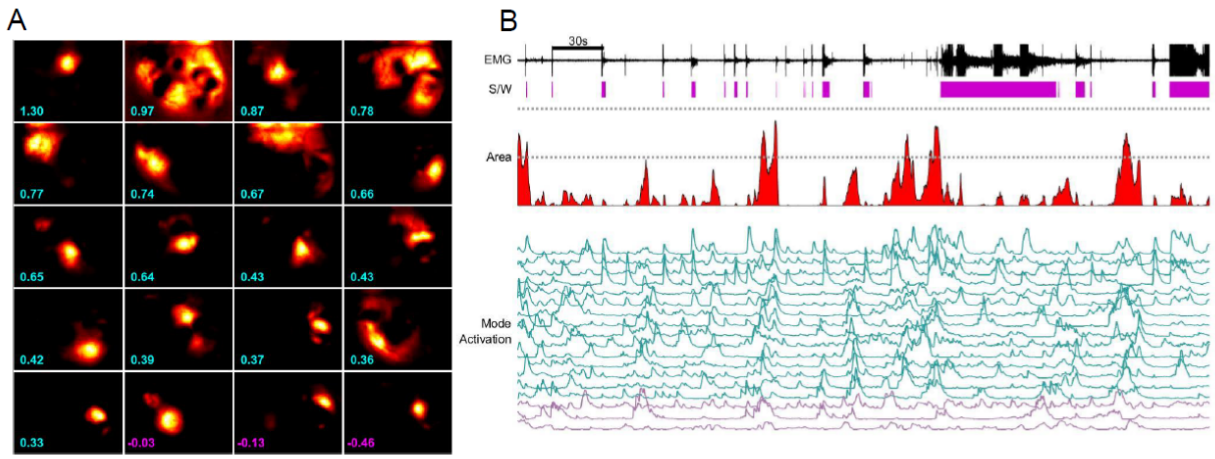

Figure 5. Non-negative Matrix Factorization of a typical record from a P6 animal. A: The 20 features required to capture 90% of the variance of the original data, displayed in descending order of the relative prominence in sleep vs wake, calculated from the mean values of their time vectors in the two states. Each is labeled with its Sleep Score, calculated as log of the mean time values of the time vectors in sleep/wake, so that a score >0 indicates preferential occurrence in sleep, and <0 preferential occurrence in wake. B: Plots of the time vectors all 20 Features arranged in descending order of sleep preference, from top to bottom, along with EMG, Sleep/Wake indicator, and fractional active area for a 9-minute continuous recording. Note the preferential occurrence of Feature 1 in sleep and Feature 20 in wake. Note the larger number of sleep associated features (17), indicating larger complexity of activity in sleep, and the larger areas of those features compared to wake features, indicating wider spatial correlation of activity in sleep.

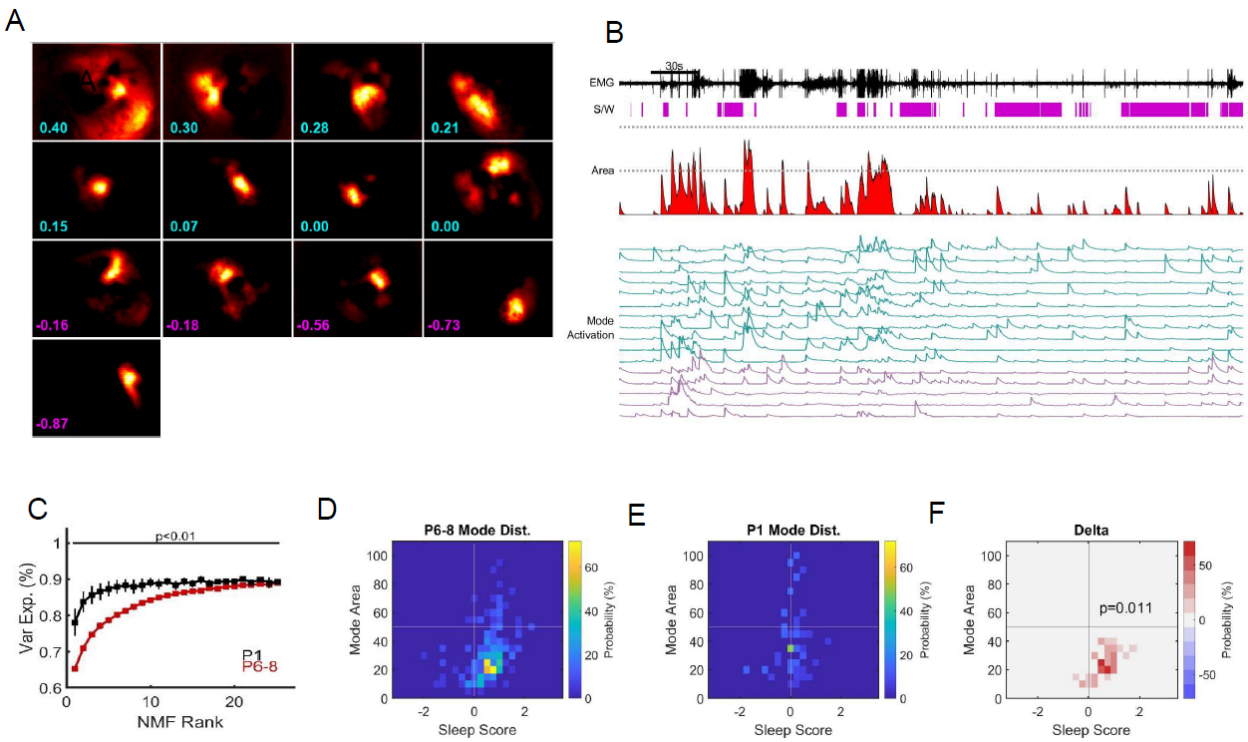

Figure 6. Non-negative Matrix Factorization of a typical record from a P1 animal. Display and labeling in A and B the same as in Fig. 5. Note the smaller total number of features required capture the same fraction of variance of the data compared to P6-P8 and the more even weighting of those features between sleep and wake, reflecting the more evenly distributed complexity of activity between the two states at P1. C: Relationship between number of features (NMF Rank) and fraction of variance captures for P6-P8 vs P1 animals. On average, fewer features are required to capture equal variances at P1. D-F: Bivariate distributions of Feature Area vs. Sleep Score at P6-P8 (D) and P1 (E), and the Sleep-Wake difference plot (F). Development during the first postnatal week is characterized by added features with wider spread (20-40% area coverage) in sleep (Sleep Score 0.5-1.2).

Sleep-deprivation results are summarized in Figure 8. The closed-loop mechanical stimulus caused a significant and reversible increase in the probability of waking (Fig. 8A,B). This resulted in a parallel reversible decrease in the probability of cortical activity covering > 50% of the hemisphere area (Fig. 8C,D) and a decrease in the frequency of pan-cortical waves Fig. 8E,F. At longer times of the experiments, stimuli became less effective in waking the animals, probably due to increased sleep pressure (Todd et al., 2010). Stimuli that failed to wake the animal also failed to produce significant reductions in the occurrence of Pan-cortical waves, indicating that it was the stimulus-induced change in behavioral state, and not the stimuli alone, that reduced Pan-cortical waves.

Synchronized broad spectrum activity is correlated with sleep waves

In order to relate calcium wave activity directly to electrical activity, we recorded EEG and calcium signals simultaneously in P6-8 pups. We used a transparent polyacetate sheet to anchor four silver wire leads to the skull using EEG gel to facilitate conduction (Fig. 9A). Figure 9B shows the position for all leads across all recordings in mm from lambda suture, taken from images of each experiment. The signals from the four channels was recorded at 1kHz with a 60Hz notch filter. Power spectra of the four signals (FFT) were not significantly different between sleep and wake, even when the analysis was restricted to sleep cycles containing waves (Fig. 9C). This is likely due to the fact that, even in sleep cycles containing waves, there are significant periods of time when large-scale activity is absent.

To refine the temporal analysis of wave activity and EEG signals we decomposed the EEG in each channel using a wavelet transform, and then collected the signals associated with all waves covering > 60% of the hemisphere area. EEG signals were triggered on crossing of 60% area fraction in the calcium signal and averaged for each channel. The spectrum over a broad range of frequencies (1-32Hz) was significantly elevated during the events, and also showed periods of quiescence before and after events (Fig. 9D). Although this analysis detected wave occurrence, no significant differences were seen between waves that occurred in sleep vs. wake.

We next asked whether sleep and wake waves could be distinguished in EEG recordings by weighting events with high levels of synchrony among the four channels, based on the fact that the propagation of the two types of events shows different spatial patterns in the calcium signals (see Fig. 2E,F). To do this, we averaged the spectrogram among all four channels and divided this average by the standard deviation across channels. This highlights events in which the signal is simultaneously elevated or decreased across all channels and penalizes cases in which the average power is elevated by a high signal in a single channel. Figure 9 E,F shows EEG signals processed in this way for sleep and wake events. As shown in Figure 9G, this method revealed significant differences between sleep and wake waves at several time points and frequencies. Thus, despite limitations in spatial resolution in on-skull EEG recordings from neonatal pups, the differences in sleep and wake waves that we detected using calcium imaging are reflected in the 4-channel EEG signal.

Discussion

Spontaneous pan-cortical waves of activity that occur in the developing brain have primarily been studied in brain slice or other in vitro preparation (Hunt et al., 2006; McCabe et al., 2006, 2007; Conhaim et al., 2011; Easton et al., 2014; Barger et al., 2016). As a result, little is known about their properties in vivo, where they must coexist with other forms of brain activity. To record pan-cortical waves in the neonatal mouse brain, we used trans-skull calcium

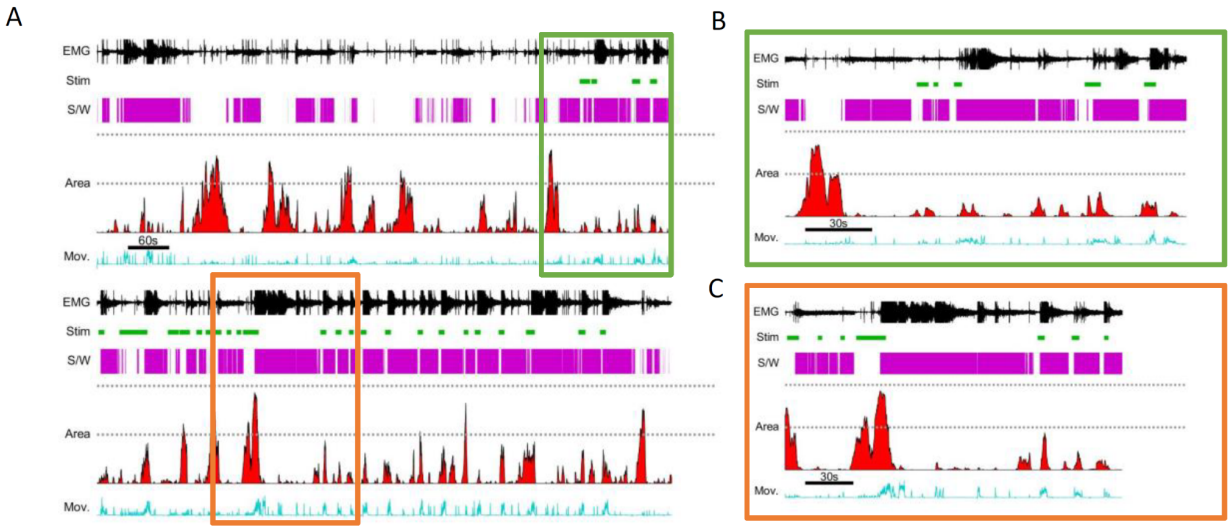

Figure 7. Forced waking reduces wave generation. A: Continuous 24-minute recording from a P6 animal. Data displayed as in Fig. 1 with the addition of the stimulus marker (green boxes, row 2) indicating closed-loop nose touch to achieve waking, activated automatically by detection of sleep onset from the nuchal EMG power spectrum. B,C: Expanded portions of record in A indicated by boxes. Note that forced waking causes an immediate truncation of pan-cortical waves, as indicated by large decrease in area coverage (red trace).

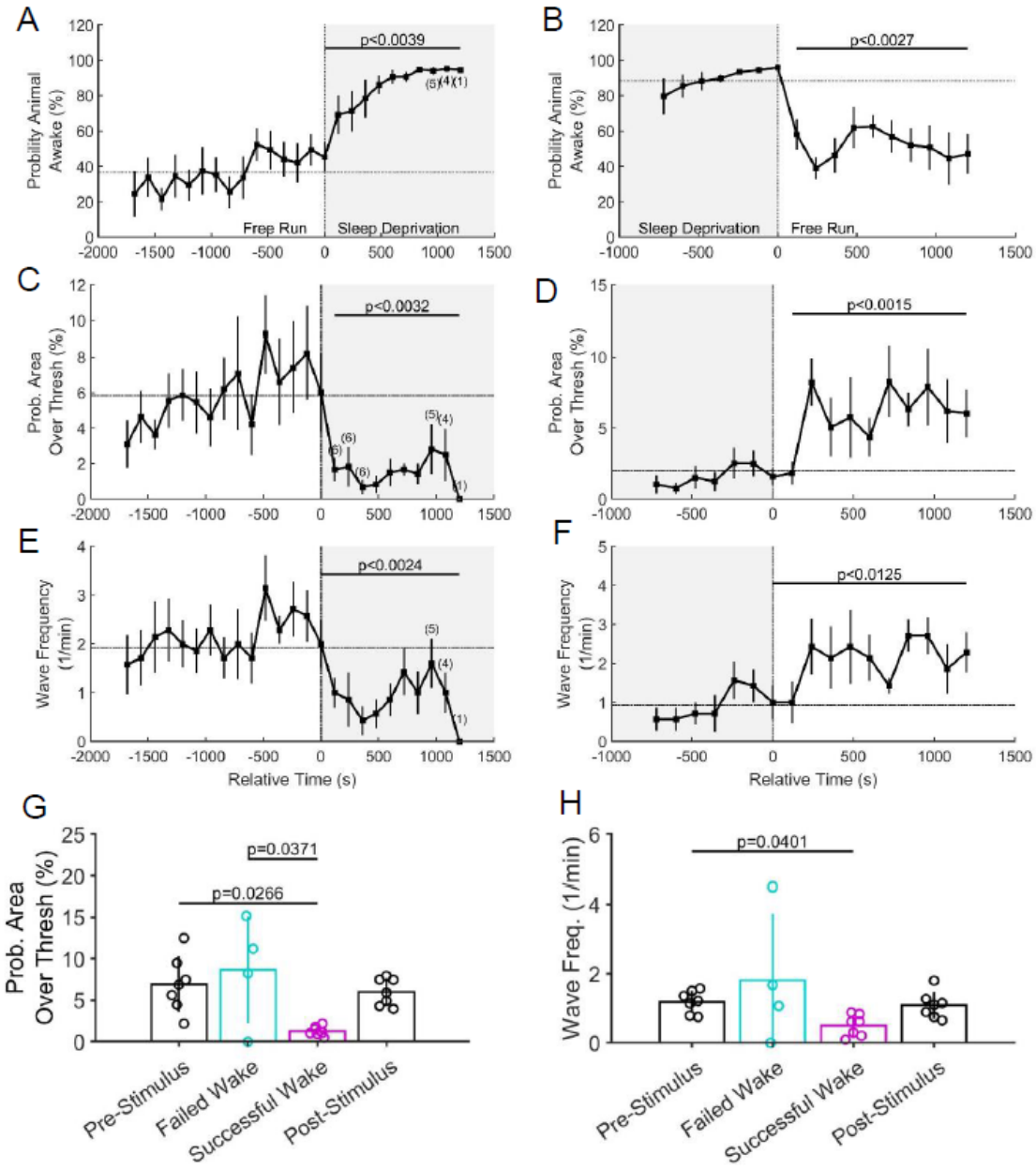

Figure 8. : Sleep deprivation disrupts correlated activity and waves. A) Probability of wake before and after entering sleep deprivation closed loop protocol. B) Probability of wake just prior to and after return to free run. Closed loop of nose touch dramatically increases the probability of wake. C & D) Percentage of time where correlated activity is high (area>50%) entering and exiting sleep deprivation. Periods of wide spread activity are significantly and reversibly depressed. E & F) Wave frequency before during and after sleep deprivation. Sleep deprivation also reversibly inhibits waves. For all, horizontal line depict the baseline means, the mean value of time bins leading up to the transition in or out of sleep derivation ($t<0$). Significance shifts from the baseline was determined by time shift permutation testing; n = 7 at all time bins unless otherwise indicated. Time bins from animals where sleep deprivation was incomplete were excluded from area and wave analyses (C-F), but not the wake probabilities (A & B). G) Percentage of time above threshold for animals prior to wake stimulus, periods where stimulus failed to wake animal, successful stimuli, and after sleep deprivation (post-stimulus). H) mean wave frequency for the same periods described in G.

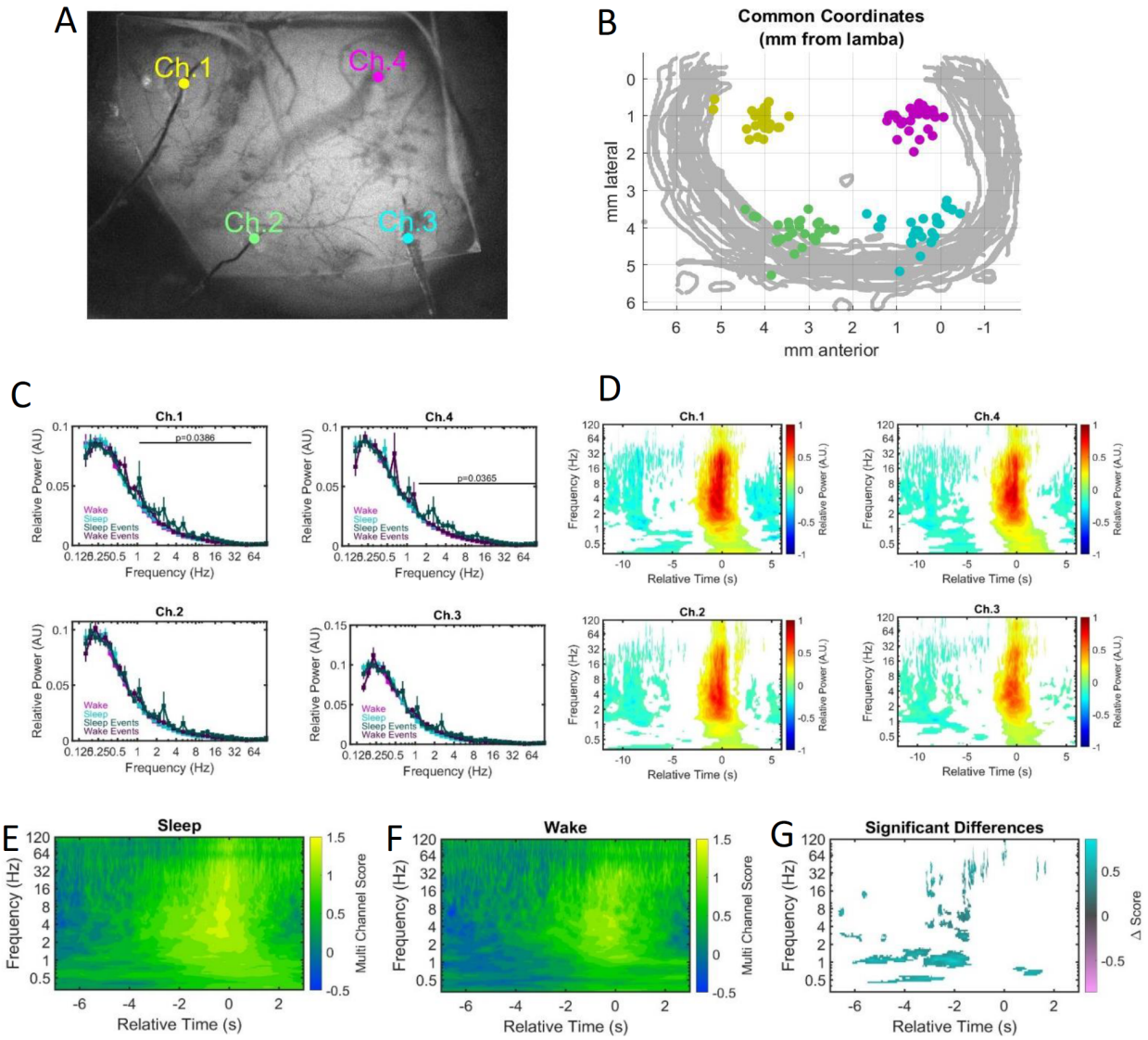

Figure 9: Sleep waves are associated with broad spectrum EEG activity. A) example field of view of the left hemisphere where EEG electrodes 1-4 are labeled. B) alignment of all fields of view to lambda suture with electrode placements. Electrodes are color coded and grey outlines are the superimposed ROIs of the cortical fields of view for each recording. C) Fourier analysis of EEG activity during periods of wake, sleep, and periods of >50% area coverage during wake and during sleep. D) Mean spectrograms for each channel created from wave triggered averages of wavelet transformed signal. Only time-frequency regions significantly elevated or depressed are depicted. E & F) Multi channel score for sleep and wake events respectively. G) Significant differences between sleep and wake events, cyan indicates increased score during sleep and magenta increased during wake.

imaging in unanesthetized animals combined with quantitative assessment of sleep-wake states based on k-means sorting of the nuchal EMG power spectrum. Based on probability histograms of event amplitudes, we identified a separate population of large-scale cortical events (Pan-cortical Waves) which propagated to cover more than 50% of the hemisphere area and which occurred almost exclusively during sleep. Although a small fraction of events during the wake state occupied this large an area, these represented the tail of the normal distribution of event amplitudes during the wake state, and they could be distinguished from pan-cortical sleep waves by their initiation points in the cortex and by their association with large body movements, an association absent in the sleep waves. Sleep waves commonly invaded the contralateral hemisphere, although our field of view did not permit us to determine how far that invasion proceeded.

Sleep states cannot be identified reliably using EEG criteria in neonatal mice sleep spindles have not yet matured, so behavioral and EMG criteria are more widely accepted as indicators of sleep (Blumberg et al., 2020). In this study, we used k-means sorting of the nuchal EMG power spectrum to make the determination of sleep and wake states more objective and reproducible. Nonetheless, by combining two of the k-means centroids into a single wake state, it is possible that some of the more active sleep states may have been misclassified as wake states. The effect of this would be to underestimate the degree of segregation of pan-cortical waves into sleep states and/or not to assess the possibility that pan-cortical waves are further segregated into a developing substate of quiet sleep.

To establish a causal relationship between sleep and these waves, we used an automated system to wake animals at the onset of sleep, triggered on the nuchal EMG power spectrum. Waking animals greatly reduced wave generation (Fig. 7). This was caused by the actual waking rather than the sensory stimulus used to wake the animals, as shown by analysis of cases in which the stimulus failed to wake animals (Fig. 8).

Analysis of image stacks using Non-negative Matrix Factorization indicated that the sleep state is generally a time of greater spatio-temporal complexity of activity and that it is characterized by an increase in the correlation of activity among spatially more distant cortical regions (Figs. 5,6). This latter conclusion was confirmed by an increase in correlation values calculated across all pixels in the image during sleep, and by the fact that cortical responses to whisker deflections occupied a significantly greater area of the cortex during sleep than wake (Fig. 4).

Finally, we showed that pan-cortical sleep waves show significant maturation between P1 and P6 (Fig. 3). P1 animals showed no preferential generation of large-scale activity in sleep, despite the fact that on average these animals sleep more than P6-P8 animals, and they showed a much weaker, although still significant, difference in the association of Pan-cortical Waves and wake-related large-scale activity with body movements.

The mechanisms responsible for wave initiation are not known. In slices, excitatory GABA action initiates waves in the first few postnatal days but this is superceded by a glutamatergic pacemaker by the end of the first postnatal week (Conhaim et al., 2010, 2011). The period of wave generation is terminated by the emergence of GABA inhibition (McCabe et al., 2007). On the other hand, the roles of GABA in neuronal synchrony are often difficult to predict. In the adult, inhibitory GABA inputs to cortical neurons are necessary to synchronize UP and DOWN states, and thus at least some forms of sleep-related propagating activity (Funk et al., 2017; Yang et al., 2017). Furthermore, GABA depolarization of neonatal cortical neurons is not

only insufficient to trigger network activity in vivo (Kirmse et al., 2015), it may actually be inhibitory to glutamate-driven wave activity (Easton et al., 2014).

Our results add to a growing body of evidence for the central role played by sleep in brain development (see Blumberg et al., 2020, for review). Early in rodent development, the primary motor cortex functions as a somatosensory area, and responds to reafferent signals from sleep-related twitches but not wake-related movements (Dooley et al., 2018). Wiring in the primary visual cortex depends in part on signals invading that area from spontaneous retinal waves, but the propagation of these signals into V1 is suppressed in the wake state (Mukherjee et al., 2017). Correlated oscillatory activity between cortex and hippocampus in infant rates occurs primarily during the sleep state (Rio-Bermudez et al., 2020). Finally, spontaneous cortical activity in the somatosensory area is also suppressed by waking (Adelsberger et al., 2005).

There appears to be a close functional relationship between neonatal pan-cortical waves and adult slow sleep waves (Steriade et al., 2001; Vanhatalo et al., 2004; Steriade, 2006; Feher et al., 2021; Salfi et al., 2020; McConnell et al., 2021). Both occur in sleep states and both involve propagating waves of electrical activity that encompass most of the cerebral cortex and in some cases other structures, such as the hippocampus (Barger et al., 2016). This relationship likely extends to the human cortex, which also generates slow sleep waves in the adult and 'infra-slow' EEG activity seen in DC-coupled EEG recordings made at stages of development comparable to neonatal mice (Clancy et al., 2001; Vanhatalo et al., 2005). In the adult, these correlations appear to mediate memory consolidation and synaptic rescaling (Salfi et al., 2020; Skelin et al., 2021; Cirelli & Tononi, 2021). In the neonate, similar correlations are likely to mediate establishment of the long-range functional circuitry of the cortex, a process that includes both synaptic strengthening by coincidence-detection mechanisms, and the neuro-protective effects of activity during the period of substantial apoptosis (Kilb et al., 2011; Blanquie et al., 2017a,b). In both cases, the sleep state appears to act a repository for spatially widespread activity that allows localized and widespread activity to be temporally segregated. In the developing brain, this allows activity-dependent developmental processes to coexist across local and global spatial domains without mutual interference. In the adult, this allows information processing in localized circuits to be separated from the activity that consolidates memory over wider range circuit domains.

Methods

Animal Procedures

All animal procedures were carried out under protocols approved by the University of Washington Institutional Animal Care and Use Committee. Experiments were done on animals homozygous for Cre dependent GCaMP6s (Ai162, Jackson labs, stock #: 031562) and heterozygous for Cre driven by Vglut1 (Slc17a7-IRES2-Cre-D, Jackson labs, stock #: 023527). Pups (P1-P8) were anesthetized globally with 2-3% isoflurane-oxygen mix and locally with injections of 0.25% bupivacaine into the scalp. Body temperature was maintained using a heating pad set to 38C (details below).Under a dissecting microscope we removed a section of scalp to expose an area roughly bounded by the base of the ears to the caudal edge of the eyes and extending caudally to expose some of the neck musculature. This exposed the majority of the dorsal surface of the frontal, parietal and interparietal bone plates. We rinsed and hydrated the wound with ACSF and removed the periosteum using fine forceps. Two silver hook wire electrodes (0.005in diameter, 36 AWG) were implanted in the neck muscle to record EMG. We used cyanoacrylate glue attach a 'U' shaped stainless steel holder which could then be clamped

to the microscope stage, and to reinforce the soft skull and seal the wound. Finally, we placed a third reference electrode just under the skin through a small dorsal incision at the midline of thorax. We then removed the animal from isoflurane, allowed a minimum of 1 hr for recovery from anesthesia, and positioned the animal on the microscope for imaging. While on the recording stage pups continued to be heated by the 38C pad but were also placed under a loosely sealed plexiglass enclosure kept humidified with a water dish. Under these conditions pups of all ages in our pilot experiments maintained a brain temperature of 36C measured by a thermocouple placed through the skull into the cortex. Local anesthesia at wound sites was maintained with topical application of bupivacaine as necessary. Animals were euthanized by decapitation if they showed signs of distress (struggling limb movements, vocalizations), or at the end of the experiment.

Calcium imaging

Calcium signals were acquired through the intact skull over the entire surface of one hemisphere at 10-45Hz using a Nikon AZ100 microscope, ORCA Flash 2.8 camera, and Hamamatsu HC Image software. Nuchal EMG was recorded using a silver wire electrode and acquired at 10kHz using LabChart software (AD Instruments). Calcium and EMG records were synchronized by acquiring the frame counter output pulse from the ORCA camera in LabChart. An infrared-wavelength film of the animal was acquired in LabChart software throughout each experiment so that calcium and EMG records could be correlated with behavior.

Separation of the EMG Record into Sleep and Wake Cycles

To determine sleep or wake state based on nuchal EMG activity, we the used k-means clustering method to generate centroids, stereotypic patterns of EMG activity, and assign each recording time point these patterns. To begin, we removed cardiac artifact from the EMG using a principal components analysis (PCA) based filtering in a manner similar to spike sorting methods in neurons. First, EKG transients were located using a manually set threshold. We then collected short windows of these traces centered on the transients, compiled them into a matrix and performed PCA. As the traces were enriched with the EKG signal the most dominant PCA modes consisted primarily of the transients. We then subtracted 1-5 of the top modes from the original traces to selectively cancel out the EKG signal but leave the underlying EMG pattern. The number of modes used was chosen on a case by case basis but erred on the side of less subtraction (weaker filtering) as only very large artefacts disrupted sleep classification. We then transformed the EMG, recorded at 10kHz, into a power spectrum density (Fig S2A) with a frequency resolution of 0 - 2.5kHz in 500 equal bins and a temporal resolution of 50ms. The relative power spectrum was calculated by diving the total recording by the mean power for each frequency bin across the entire recording. A sliding window 400ms wide of this power spectrum was used to classify each 50ms bin. We used the k-means function (MATLAB) and used an empirically chosen k equal to three as we observed three primary patterns of behavior & activity: (1) High amplitude activity (movement) on a background of high muscle tone indicating wakefulness; (2) High tone without movement indicating wakefulness; and (3) Low muscle tone indicating sleep. The two wake categories were combined after sorting. These patterns are typified by the example centroids shown in Figure S2b, and the corresponding EMG trace (Fig S2c). The resulting centroids from each classification run are not ordered in a particular fashion. However, ranking the centroids by total power always resulted in movement as the highest power centroid and low muscle tone as the lowest, thus the sleep and wake centroids could be reliably

distinguished for each run. Finally, the behavioral state over time was down sampled to match the frame rate of imaging. To validate this method, we divided each recording into two data sets, a test set of randomly chosen time points (20% of the total recording) and a training set (the remaining 80%). The training set was used to generate centroids using the above described k-means method and the test set was classified to these centroids. This was repeated 10 times for each recording. The test sets were compared to a consensus built by taking the mode of 10 replicated training sets for each time point which we treat as our ground truth for this validation. The mean rate at which the training set match consensus was 99.44% (SEM=0.25%, n=33 recordings), indicating a robust and repeatable classification.

Analysis of Calcium Imaging Data

Films of the raw calcium signal were imported into ImageJ, down sampled by averaging to a pixel resolution of 240 x 180, and converted to ΔF/F0 using a reference frame created by a minimum-value Z-projection of the image stack. These records were bleach-corrected, if necessary, in MATLAB using a baseline signal created by cubic spline interpolation of a series of manually selected baseline points. To determine the fractional hemispheric area occupied by each event, the maximum ΔF/F0 for the hemisphere was determined for each frame. These data were separated into sleep and wake frames in MatLab using a logical array that marked sleep frames based on the above EMG criteria. These records were searched for peaks using MatLab based on a 0.1 Peak Prominence and a 100-frame minimum distance. The fractional hemispheric area occupied by activity was computed for each frame defining active pixels as those exceeding 20% of the maximum ΔF/F0 calculated above, separately for sleep and wake states. This ensured that the area fraction calculation was not biased by different mean event amplitudes in sleep and wake. In practice, the mean event amplitudes in the two states varied by <10%. Finally, the sleep and wake frame sets were recombined into a single vector representing the area fraction as a function of time. From these plots, we defined pan-cortical waves based on the largest mode of even amplitudes in frequency histograms of all event amplitudes (see Fig. 2C). This was between 60 -65% area fraction for all experiments. Initiation points and times for events were based on 5% area coverage. For initiation point analysis we excluded waves that either invaded the imaged hemisphere from the contralateral side or started while other activity was in progress, so the points of origin could not be determined.

Non-Negative Matrix Factorization (NNMF) of Calcium Data

The ΔF/F0 image stacks were imported into MatLab, and reshaped into 2-dimensional matrices (a time dimension and a single consolidated spatial dimension). The resulting matrix was factored into a series of paired spatial and temporal components, using the MatLab implementation of the alternating least squares algorithm for NNMF. Each imaging run (2-5 / animal) was calculated separately and was repeated increasing the number of component pairs (from 1 - 25) used to estimate the total image stack for each run. The optimal number of component pairs used for final analysis was chosen to reduce the residual error by 90% of the distance between 1 and 25 components, at which point the error reached a pseudo-asymptote and the plot of error vs. component number became unstable. The resulting spatial features were transformed back into two-dimensional pseudo images of spatial activity patterns. The relative contribution of each spatial feature at any given time is indicated by its corresponding temporal component, a time series vector. To determine the segregation of a given spatial component into sleep and wake cycles, we divided the mean time vector for that component in sleep by its mean

value in wake. We refer to this number as the S/W ratio. In each recording a component pair consisting off cortex background activity was often observed. These were easily identified due to their characteristic spatial pattern (low amplitude activity restricted to frame edge) and their relative invariance of the temporal component, and were omitted from this study. To calculate the area of components a threshold of 20% of the maximum amplitude with in each spatial feature was used.

EEG Recording

Silver wire (0.005 in diameter, 36 AWG) leads were anchored to the skull in four locations using a transparent polyacetate sheet and EEG gel. The sheets were cut by hand and four holes were punched using a thumb tack to form a right sided trapezoid. Each hole was filled with a small dab of EEG recording gel and the sheet was glued to the skull such that the electrodes could be temporarily friction fit through the top of the sheet after glue had set. After placing the electrodes another layer of glue was applied to stabilize the wires. Signals were sampled at 1kHz using a 0.1 kHz low-frequency cutoff filter and a 60Hz notch filter, using an AM Systems Model 3600 amplifier. To analyze the frequency content with high temporal resolution we used the continuous wavelet transform in MatLab. The frequency range was limited from 0.3Hz to 120Hz with 12 voices per octave, yielding 104 frequency bins logarithmically spaced,with a temporal resolution matching the native EEG sampling rate of 1kHz. The wavelet power was scaled for each frequency bin independently by subtracting the mean power for the entire recording and dividing by the standard deviation of the entire. These normalized frequency powers were used to calculate the overall spectral content, the triggered average activity, and for the multi channel score.

Literature Cited

Adelsberger H, Garaschuk O, Konnerth A (2005). Cortical calcium waves in resting newborn mice. Nat Neurosci. 8:988-90.

Blankenship AG, Feller MB (2010) Mechanisms underlying spontaneous patterned activity in developing neural circuits. Nat Rev Neurosci 11:18–29.

Barger Z, Easton CR, Neuzil KE, Moody WJ (2016) Early network activity propagates bidirectionally between hippocampus and cortex. Dev Neurobiol 76:661–672

Berry M, Borwne M, Langville A, Pauca V, Plemmons R (2007) Algorithms and applications for approximate nonnegative matrix factorization. Computational Statistics and Data Analysis 52:155–173

Blanquie O, Kilb W, Sinning A, Luhmann HJ (2017a) Homeostatic interplay between electrical activity and neuronal apoptosis in the developing neocortex. Neuroscience 358:190–200.

Blanquie O, Yang J-W, Kilb W, Sharopov S, Sinning A, Luhmann HJ (2017b) Electrical activity controls area-specific expression of neuronal apoptosis in the mouse developing cerebral cortex. Elife 6

Blumberg MS, Dooley JC, Sokoloff G. (2020). The developing brain revealed during sleep. Curr Opin Physiol. 15:14-22.

Chang M, Kanold PO (2021). Development of Auditory Cortex Circuits. J Assoc Res Otolaryngol 22:237-259.

Cirelli C, Tononi G. (2021). The why and how of sleep-dependent synaptic down-selection. Semin Cell Dev Biol. 9:S1084-9521

Clancy B, Darlington RB, Finlay BL (2001) Translating developmental time across mammalian species. Neuroscience 105:7–17

Conhaim J, Cedarbaum ER, Barahimi M, Moore JG, Becker MI, Gleiss H, Kohl C, Moody WJ (2010) Bimodal septal and cortical triggering and complex propagation patterns of spontaneous waves of activity in the developing mouse cerebral cortex. Dev Neurobiol 70:679–692

Conhaim J, Easton CR, Becker MI, Barahimi M, Cedarbaum ER, Moore JG, Mather LF, Dabagh S, Minter DJ, Moen SP, Moody WJ (2011) Developmental changes in propagation patterns and transmitter dependence of waves of spontaneous activity in the mouse cerebral cortex. J Physiol (Lond) 589:2529–2541

Dooley JC, Blumberg MS (2018). Developmental 'awakening' of primary motor cortex to the sensory consequences of movement. Elife 7:e41841.

Easton CR, Weir K, Scott A, Moen SP, Barger Z, Folch A, Hevner RF, Moody WJ (2014) Genetic elimination of GABAergic neurotransmission reveals two distinct pacemakers for spontaneous waves of activity in the developing mouse cortex. J Neurosci 34:3854–3863

Feher KD, Winderlin M, Maier JG, Hertenstein E, Schneider CL, Mikutta C, Zust MA, Kloppel S, Nissen C. (2021). Shaping the slow waves of sleep: A systematic and integrative review of sleep slow wave modulation in humans using non-invasive brain stimulation. Sleep Med Rev 58: 101438

Funk CM, Peelman K, Bellesi M, Marshall W, Cirelli C, Tononi G (2017) Role of Somatostatin-Positive Cortical Interneurons in the Generation of Sleep Slow Waves. J Neurosci 37:9132–9148

Gómez LJ, Dooley JC, Sokoloff G, Blumberg MS (2021). Parallel and Serial Sensory Processing in Developing Primary Somatosensory and Motor Cortex. J. Neurosci 41:3418-3431.

Hunt PN, McCabe AK, Gust J, Bosma MM (2006) Spatial restriction of spontaneous activity towards the rostral primary initiating zone during development of the embryonic mouse hindbrain. J Neurobiol 66:1225–1238

Kilb W, Kirischuk S, Luhmann HJ (2011) Electrical activity patterns and the functional maturation of the neocortex. Eur J Neurosci 34:1677–1686.

Kirmse K, Kummer M, Kovalchuk Y, Witte OW, Garaschuk O, Holthoff K (2015) GABA depolarizes immature neurons and inhibits network activity in the neonatal neocortex in vivo. Nature Communications 6:7750

Lissek T, Obenhaus HA, Ditzel DAW, Nagai T, Miyawaki A, Sprengel R, Hasan MT (2016) General Anesthetic Conditions Induce Network Synchrony and Disrupt Sensory Processing in the Cortex. Front Cell Neurosci 10:64

Massimini M, Huber R, Ferrarelli F, Hill S, Tononi G (2004) The sleep slow oscillation as a traveling wave. J Neurosci 24:6862–6870

McCabe AK, Chisholm SL, Picken-Bahrey HL, Moody WJ (2006) The self-regulating nature of spontaneous synchronized activity in developing mouse cortical neurones. J Physiol (Lond) 577:155–167

McCabe AK, Easton CR, Lischalk JW, Moody WJ (2007) Roles of glutamate and GABA receptors in setting the developmental timing of spontaneous synchronized activity in the developing mouse cortex. Dev Neurobiol 67:1574–1588

McConnell BV, Kronberg E, Teale PD, Sillau SH, Fishback GM, Kaplan RI, Fought AJ, Dhanasekaran AR, Berman BD, Ramos AR, McClure RL, Bettcher BM (2021). The Aging Slow Wave: A Shifting Amalgam of Distinct Slow Wave and Spindle Coupling Subtypes Define Slow Wave Sleep Across the Human Lifespan. Sleep 17:zsab125

Molnár Z, Luhmann HJ, Kanold PO (2020). Transient cortical circuits match spontaneous and sensory-driven activity during development. Science 16:370

Mukherjee D, Yonk AJ, Sokoloff G, Blumberg MS (2017) Wakefulness suppresses retinal wave-related neural activity in visual cortex. J Neurophysiol 118:1190–1197

Rio-Bermudez CD, Kim J, Sokoloff G, Blumberg MS (2020). Active Sleep Promotes Coherent Oscillatory Activity in the Cortico-Hippocampal System of Infant Rats. Cereb. Cortex 14:2070-2082.

Riyahi P, Phillips MA, Colonnese MT (2021). Input-Independent Homeostasis of Developing Thalamocortical Activity, ENeuro 8:0184-21.

Salfi F, D'Atri A, Tempesta D, De Gennaro L, Ferrara M. (2020). Boosting slow oscillations during sleep to improve memory function in elderly people: A review of the literature. Brain Sci. 10:300

Skelin I, Zhang H, Zheng J, Ma S, Mander BA, Kim McManus O, Vadera S, Knight RT, McNaughton BL, Lin JJ (2021). Coupling between slow waves and sharp-wave ripples engages distributed neural activity during sleep in humans. Proc Natl Acad Sci U S A. 118:e2012075118

Steriade M (2006) Grouping of brain rhythms in corticothalamic systems. Neuroscience 137:1087–1106

Steriade M, Timofeev I, Grenier F (2001) Natural waking and sleep states: a view from inside neocortical neurons. J Neurophysiol 85:1969–1985

Todd WD, Gibson JL, Shaw CS, Blumberg MS (2010). Brainstem and hypothalamic regulation of sleep pressure and rebound in newborn rats. Behav Neurosci. 124:69-78

Vanhatalo S, Palva JM, Andersson S, Rivera C, Voipio J, Kaila K (2005) Slow endogenous activity transients and developmental expression of K+-Cl- cotransporter 2 in the immature human cortex. Eur J Neurosci 22:2799–2804

Vanhatalo S, Palva JM, Holmes MD, Miller JW, Voipio J, Kaila K (2004) Infraslow oscillations modulate excitability and interictal epileptic activity in the human cortex during sleep. Proc Natl Acad Sci USA 101:5053–5057Wei Y, Krishnan GP, Bazhenov M (2016) Synaptic Mechanisms of Memory Consolidation during Sleep Slow Oscillations. J Neurosci 36:4231–4247

Yang J-W, Prouvot P-H, Reyes-Puerta V, Stüttgen MC, Stroh A, Luhmann HJ (2017) Optogenetic Modulation of a Minor Fraction of Parvalbumin-Positive Interneurons Specifically Affects Spatiotemporal Dynamics of Spontaneous and Sensory-Evoked Activity in Mouse Somatosensory Cortex in Vivo. Cereb Cortex 27:5784–5803

Supplemental Material

Supplemental Movies

Movies are available for download at `https://github.com/dtabuena/PanCorticalWaves/tree/main/SupplementalVideos`.

Movie 1: An 24 sec recording of P7 pup during a sleep, corresponding to the montage in Fig. 1A. The time synced EMG trace is scrolls below where the red cursor indicates the activity visible in in the current frame and the shaded region indicates a window of ±0.25s. The behavioral state is indicated in the upper right with a magenta ‘W’ for wake and cyan ‘S’ for sleep. Time is indicated in the lower left in seconds. The audio is a direct play back of the EMG trace. Wave begins in the occipital region and propogates rostrally.

Movie 2: An 8 sec recording of P7 pup during a sleep, corresponding to the montage in Fig. 1B. The time synced EMG trace is scrolls below where the red cursor indicates the activity visible in in the current frame and the shaded region indicates a window of ±0.25s. The behavioral state is indicated in the upper right with a magenta ‘W’ for wake and cyan ‘S’ for sleep. Time is indicated in the lower left in seconds. The audio is a direct play back of the EMG trace. Wave begins in the rostral-medial region and propogates caudally.

Movies 3: A time accelerated movie (5X) of a 10 min recording of P7 pup with multiple sleep wake transition and waves. The time synced EMG trace is scrolls below where the red cursor indicates the activity visible in in the current frame and the shaded region indicates a window of ±0.25s. The behavioral state is indicated in the upper right with a magenta ‘W’ for wake and cyan ‘S’ for sleep. Time is indicated in the lower left (mm:ss). The audio is a direct play back of the EMG trace and clearly distinguishes periods of wake and sleep. Sleep periods are dominated by broad waves of activity, while during wake activity spans smaller asynchronous regions and high activity in motor cortex.

Supplemental Figures

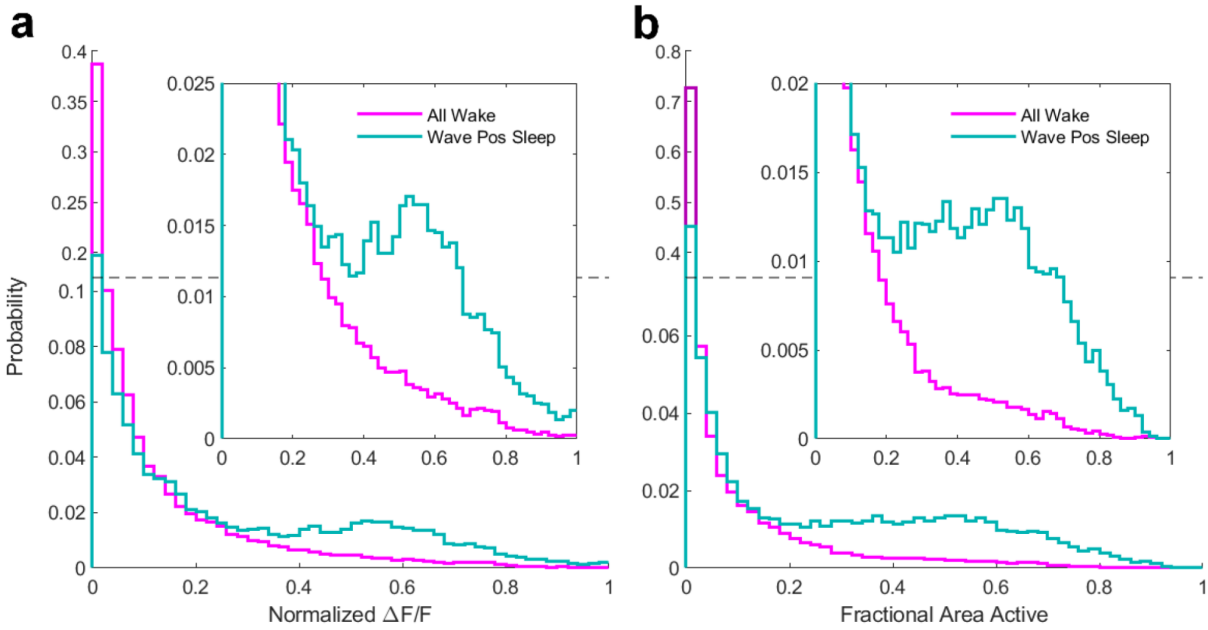

Supplemental Figure 1: Bimodality in of Cortical Activity. (a,b) Probability distributions of normalized ΔF/F and area active especially for wake periods of wake (magenta) and wave containing sleep (cyan), dashed line indicates y-axis break and insets are magnified regions of the distributions. Both measures indicate a bimodal activity pattern during sleep that is not present in wake. Inserts magnify the higher end of the distributions.

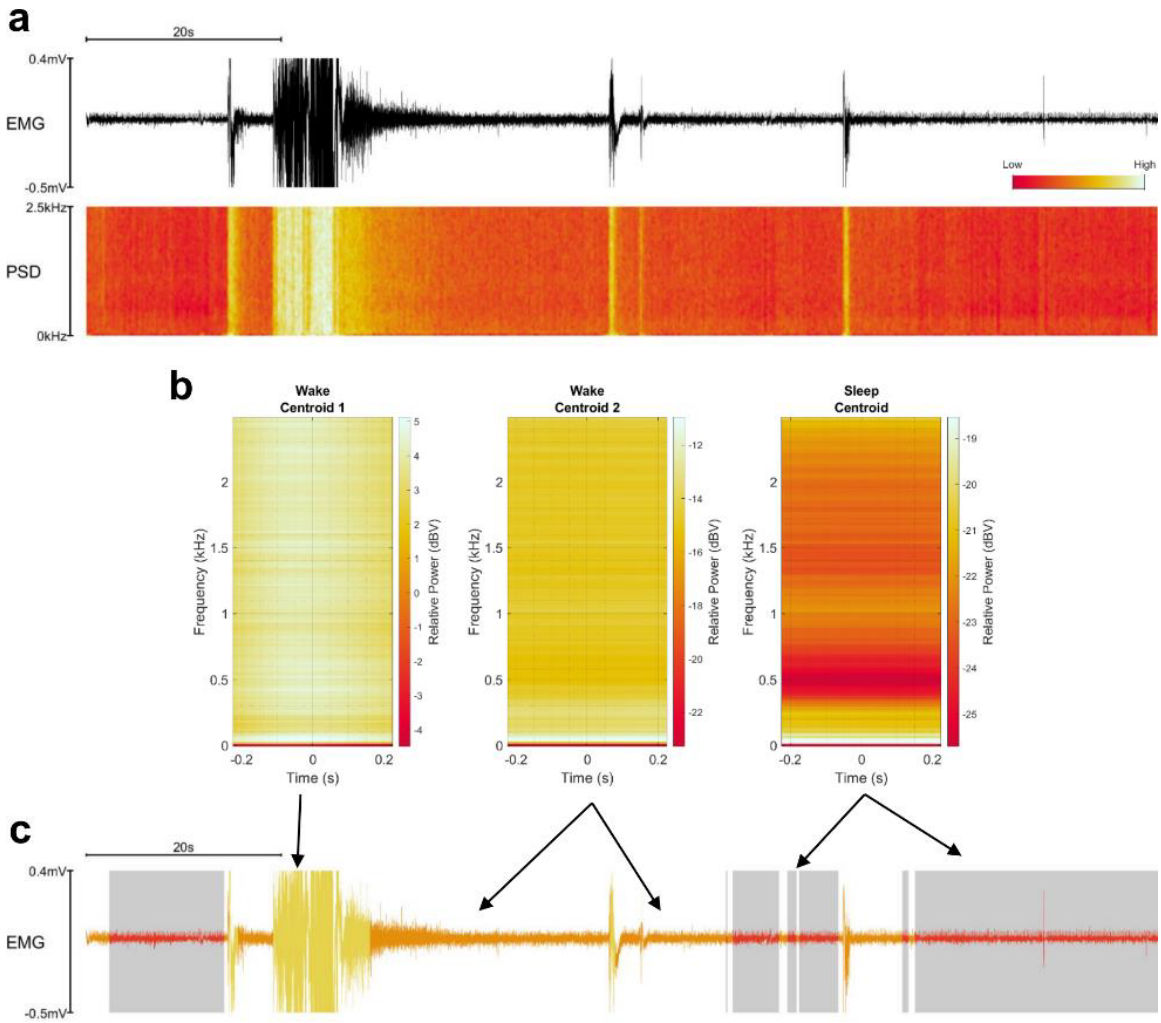

Supplemental Figure 2: K-means clustering of EMG power spectrum to separate sleep and wake states. (a) A typical recording of EMG activity (top) and associated power spectrum density (bottom). (b) The three centroids generated using k-means where (k=3, see methods) two wake (left and center) and one sleep (right). Centroids determined from a sliding window of time in the PSD centered on the time point to be classified. These centroids as well as those from all other recordings correspond to three primary EMG patterns: a period of movement during wake (Wake 1) indicated by high power across all frequencies, a period of still wakefulness with moderate EMG power indicated by high muscle tone (Wake 2), and finally a period of relative low power composed primarily of spectral components present in the background ECG (Sleep). (c) Classification of the EMG trace in a, color-coded to indicate the best fit behavior state (shortest distance to centroid) with yellow and light orange indicating wake and red indicating sleep (also shaded grey).

Go with the FLOW: Visualizing spatiotemporal dynamics in optical widefield calcium imaging

(Journal of the Royal Society Interface, 2021)

Nathaniel J. Linden[1,2], Dennis R. Tabuena[2,3], Nicholas A. Steinmetz[4], William J. Moody[2], Steven L. Brunton[5], Bingni W. Brunton[2,*]

[1]Department of Bioengineering, University of Washington, Seattle
[2]Department of Biology, University of Washington, Seattle
[3]Graduate Program in Neuroscience, University of Washington, Seattle
[4]Department of Biological Structure, University of Washington, Seattle
[5]Department of Mechanical Engineering, University of Washington, Seattle
[*] Corresponding author: bbrunton@uw.edu.

Abstract
Widefield calcium imaging has recently emerged as a powerful experimental technique to record coordinated large-scale brain activity. These measurements present a unique opportunity to characterize spatiotemporally coherent structures that underlie neural activity across many regions of the brain. In this work, we leverage analytic techniques from fluid dynamics to develop a visualization framework that highlights features of flow across the cortex, mapping time-varying sources and wave fronts that may be correlated with behavioral events. First, we transform the time series of widefield calcium images into time-varying vector fields using optic flow. Next, we extract concise diagrams summarizing the dynamics, which we refer to as FLOW (flow lines in optical widefield imaging) portraits. These FLOW portraits provide an intuitive map of dynamic calcium activity, including regions of initiation and termination, as well as the direction and extent of activity spread. To extract these structures, we use the finite-time Lyapunov exponent (FTLE) technique developed to analyze time-varying manifolds in unsteady fluids. Importantly, our approach captures coherent structures that are poorly represented by traditional modal decomposition techniques. We demonstrate the application of FLOW portraits on three simple synthetic datasets and two widefield calcium imaging datasets, including cortical waves in the developing mouse cortex and spontaneous cortical activity in an adult mouse.
Keywords– Widefield calcium imaging, computational neuroscience, dynamical systems, coherent structures, finite time Lyapunov exponents.

1 Introduction

Coordinated organization of neural activity among brain regions is believed to serve many crucial roles, including performing specific computations in the cortex [1–3] and supporting brain development [4–6]; further, its disruption may lead to neurological disease [7–9]. One prominent characteristic of neural activity at the scale of brain regions is the rapid and coherent propagation of activity across cortex, which has been widely observed in a variety of contexts, including spontaneous activity, task engagement, sleep, and development [10–12]. Qualitatively similar patterns of neural activity propagation have been also observed

in the retina, often referred to as retinal waves, during development [13–16]. Although such spatiotemporal dynamic features are often visually salient, it remains challenging to quantify and succinctly summarize their behavior directly from neural recordings.

Widefield optical imaging of calcium activity provides a unique opportunity to study coordinated spatiotemporal neural activity among brain areas, because this experimental approach achieves large fields-of-view with high temporal and spatial resolution [17, 18]. In general, widefield imaging experiments involve fluorescence imaging of the entire brain surface of transgenic animals that express optical indicator proteins in known populations of neurons [19–24]. Many experiments choose to use genetically encoded calcium indicators from the GCaMP family to image neural calcium dynamics, which is a proxy for electrical neuronal activity [25–28]; more generally, the visualization methods we discuss here can be applied to any widefield optical imaging experiment, such as imaging with voltage-sensitive indicators [29, 30]. Cortical activity has been measured using widefield calcium imaging in a variety of experiments, notably to study perceptual decision making [1, 3, 31–35], to extract cortical functional connectivity [8, 36, 37], to characterize cortical activity that organize brain development [38], and to study the effects of disease in the cortex [7–9]. In all of these data, it is typical to observe multiple regions activating transiently or in regular succession, with distinct source regions and wave-like flows of activity across the fields of view. These features can often be described as flow of activity with coherent traveling fronts, distinct sources, and sinks; interestingly, all of these patterns are well studied as nonlinear features of spatiotemporal dynamical systems [39].

The most widely applied approaches to analyze time-varying recordings of high-dimensional neural activity are dimensionality reduction techniques, which extract modes that correspond to dominant, low dimensional features of the high-dimensional data [40–42]. These low-dimensional features are useful as representations of the neural activity that facilitate further analysis and modeling. Furthermore, the observation that the dynamics of neuronal populations can be reduced to a relatively small number of features may be a clue about the mechanisms that underlie coordinated neural activity [43–46]. Common modal decomposition algorithms used in neuroscience [40, 47] include singular value decomposition (SVD), which is closely related to principle component analysis (PCA), independent component analysis (ICA), and nonnegative matrix factorization (NNMF). These techniques all solve for combinations of relatively few modes in space and time that reconstruct an estimate of the original high-dimensional data; their solutions differ by making different assumptions about the statistical structure of the modes.

There are many exciting recent innovations in modal decomposition for analyzing large-scale neural data, some of which are extensions and derivatives of SVD, ICA, and NNMF. Interestingly, while some of these methods have explicit representations of the temporal dynamics (for instance, jPCA [44], dynamic mode decomposition (DMD) [48–50], and NNMF with temporal constraints [51–54]), they largely set out to achieve space/time separation. Applying PCA and NNMF to segments of synthetic and experimental data (Figure 1A) yields a set of spatial modes (Figure 1B; temporal modes not shown) that provide a representation of the activity. However, these representations are static modes and may not adequately summarize spatiotemporal data.

A complementary set of methods have been developed to describe spatiotemporal

patterns in widefield neural activity by explicitly extracting propagating waves. Traveling waves are often characterized by their propagation speed (amplitude) and their direction (see [55] and [56] for examples), and these measures are then aggregated for all of the waves observed in a recording to quantify the trends in wave dynamics. While this information has proven useful in studying the roles of waves, the approach is limited because waves need to be identified individually. Several related methods have used the computation of optical flow to convert widefield activity to time-varying vector fields [57, 58]. This velocity field can then be analyzed using tools from vector calculus to identify fixed points, including classifying each fixed point as a source or a sink of activity. Nevertheless, these methods are constrained to identify only fixed points and cannot identify multiple local planar waves.

Our visualization approach is inspired by the similarity of spatial flows observed in widefield optical imaging to flows of physical fluids. Humans have a deep intuition about fluid flows from our everyday experiences (e.g., the patterns of milk mixing in coffee, a river flowing). Representing brain data as a flow allows us to leverage this intuition and decades of methods from flow analysis and visualization. Propagation of neural activity has many commonalities and differences with physical fluid flows. In both, there exist coherent structures whose boundaries may be invariant even as the activity changes with time. In fluid physics, these invariant manifolds are known as Lagrangian coherent structures (LCS) [59–61], which act as transport barriers in the flow, either repelling or attracting material. LCS are often visualized by computing ridges in the finite-time Lyapunov exponent (FTLE) field [62–65], although there are other computational approaches based on variational theory [66]. Some noteworthy biological applications include the use of LCS to study the physics of jellyfish feeding [67] and understanding cardiovascular hemodynamics [68, 69]. Unlike physical flows, neural activity is not governed by fundamental conservation laws; nevertheless, these dynamics are well described by time-varying vector fields [57, 58, 70, 71].

In this work, we develop a visualization framework to capture the spatiotemporal dynamics of neural activity by extracting field lines in optical widefield imaging, which we call FLOW portraits. FLOW portraits are generated by considering frame-by-frame dynamics as time-varying optical flow vector fields, from which we compute and integrate the ridges in its FTLE. To validate and develop intuition for our approach, we show that FLOW portraits give accurate and interpretable visual summaries of simple synthetic datasets. Next, we apply our methods to analyze bouts of activity from two widefield calcium imaging datasets in mice, both of which exhibit spontaneous, widespread activity across cortex. The first data are recordings of spontaneous cortical activity of GCaMP6s-expressing mouse pups during their first 8 postnatal days [38]. The second example are recordings of spontaneous cortical activity in a GCaMP6s-expressing adult mouse [35]. In both examples, we demonstrate that FLOW portraits extract meaningful and interpretable outlines of the dominant patterns in the cortical activity that contribute to our understanding of the animals' developmental and behavioral states.

2 FLOW Portraits

This work introduces FLOW (flow lines in optical widefield imaging) portraits, which are visualizations that provide a concise and intuitive summary of the spatiotemporal

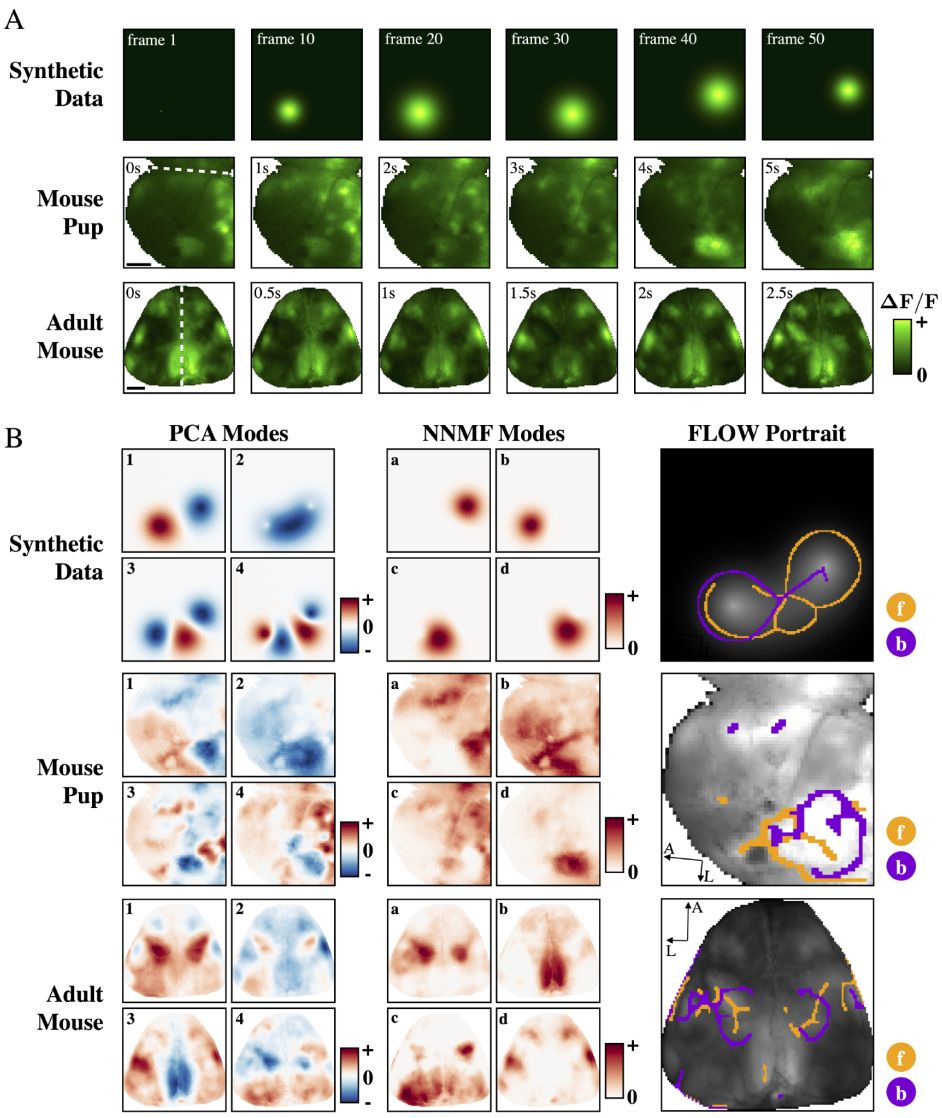

Figure 1: FLOW portraits capture coherent propagation of structures that are poorly represented by common modal decompositions that aim to achieve space-time factorization. (A) Three examples of spatiotemporal data for which we compare principal component analysis (PCA), non-negative matrix factorization (NNMF), and our FLOW portraits. One synthetic example is a two-dimensional Gaussian that grows, translates to the right, then shrinks. Two further in vivo examples are widefield calcium imaging data from a developing pup and an adult mouse. The dashed white lines at 0 sec indicate the mideline of the brain. The mouse pup data includes a pan-cortical wave from a postnatal day 7 (P7) animal; scale bar is 1 mm. The adult mouse data shows spontaneous widefield calcium activity recorded in the dark; scale bar is 2 mm. (B) FLOW portraits show a succinct summary of the spatiotemporal flow in each example dataset, while spatial PCA and NNMF modes do not. The PCA modes are the first 4 spatial components; the NNMF modes are from a 4-mode solution to the factorization and are not ordered. Both sets of modes decompose the growth and translation of activity into static spatial images, from which the flow of the activity cannot be easily appreciated. In contrast, our FLOW portraits highlight regions of activity initiation and termination, as well as the direction and extent of activity spread. Orange structures ('f'; forward time FTLE) capture regions where activity propagates from, and purple structures ('b'; backward time FTLE) capture regions where activity propagates towards. Supplemental videos illustrating all datasets are available as Supplemental Videos 1–5. FLOW portraits were computed with integration lengths of 10 frames, 40 frames, and 15 frames and the threshold percentile was set to the 85th, 93rd and 93rd percentiles for the synthetic, mouse pup, and adult mouse datasets, respectively.

dynamics, highlighting coherent structures in widefield recordings. Importantly, FLOW portraits differ from modal decomposition techniques in that they do not provide a basis in which to approximate the data and cannot quantitatively explain variance in the recordings. Instead, FLOW portraits explicitly convert the image stack into time-varying vector fields to extract patterns of activity propagation in the data (Figure 1). As our approach leverages and adapts analytic techniques from fluid dynamics [61] that are unfamiliar to most neuroscientists, this section describes how to compute finite time Lyapunov exponent (FTLE) from time-varying vector fields. We also build intuition for how the ridges of the FTLE field can be interpreted in the context of widefield calcium imaging, using several simple synthetic examples.

The steps of our approach to compute FLOW portraits are illustrated in Figures 2 and 3. The input data is a video (i.e. image stack) of the relative change of fluorescence of the imaged optical protein indicator, $\Delta F/F$, as it changes in time over many frames. The raw fluorescence may drift over the course of an experiment, so $\Delta F/F$ is considered to be a robust proxy for the magnitude of neural activation, normalizing the change in fluorescence over a moving-window baseline [72]. FLOW portraits are well suited to summarize data where optical activity is seen to diffuse or flow across the field of view, with varied patterns throughout the recording. To characterize the propagation of recorded neural activity across brain areas through space, we first compute the flow vector field using optic flow. Next, the FTLE is computed from the time-varying vector field using the standard integration method as outlined by Onu et al. [73]. Last, the FTLE field is post-processed to visualize ridge-like features that highlight the coherent features of a spatial flow [61, 62]. It is important to note that we refer to the processed FTLE ridges as FLOW portraits to avoid misinterpretation with traditional LCS analysis in fluid dynamics [61]. Details of data collection, preprocessing, and computation are described in the Methods (Section 5).

2.1 Optical flow of widefield imaging data

We describe the frame-by-frame spread of neural activity as time-varying vector fields, computed by optical flow. In specific, as regions of high pixel intensity in $\Delta F/F$ move and diffuse across the field of view, these coherent motions can be converted into a vector field of velocities, dx/dt and dy/dt, at every pixel in the recording. We denote this vector field as $v(x, t)$, defined at every point in space x at time t. Motion velocities are commonly estimated from video data in computer vision using optical flow algorithms [74], and biological visual systems of vertebrates and invertebrates also perceive moving scenes with computations akin to optical flow [75, 76]. In addition, some prior work has explored optical flow computations in widefield calcium imaging data [57, 58]. Here we use the Horn-Schunck (HS) [77] method because of its simplicity and its observed strong performance on our sample data.

Figure 3A and B show an example of snapshots of $\Delta F/F$ data and the extracted optical flow vector fields. The magnitude and direction of the vector at each pixel is computed by solving for the optimal vector field that describes the change from each frame to the subsequent frame (see schematic in Figure 2A). In order to minimize the effects of noise and

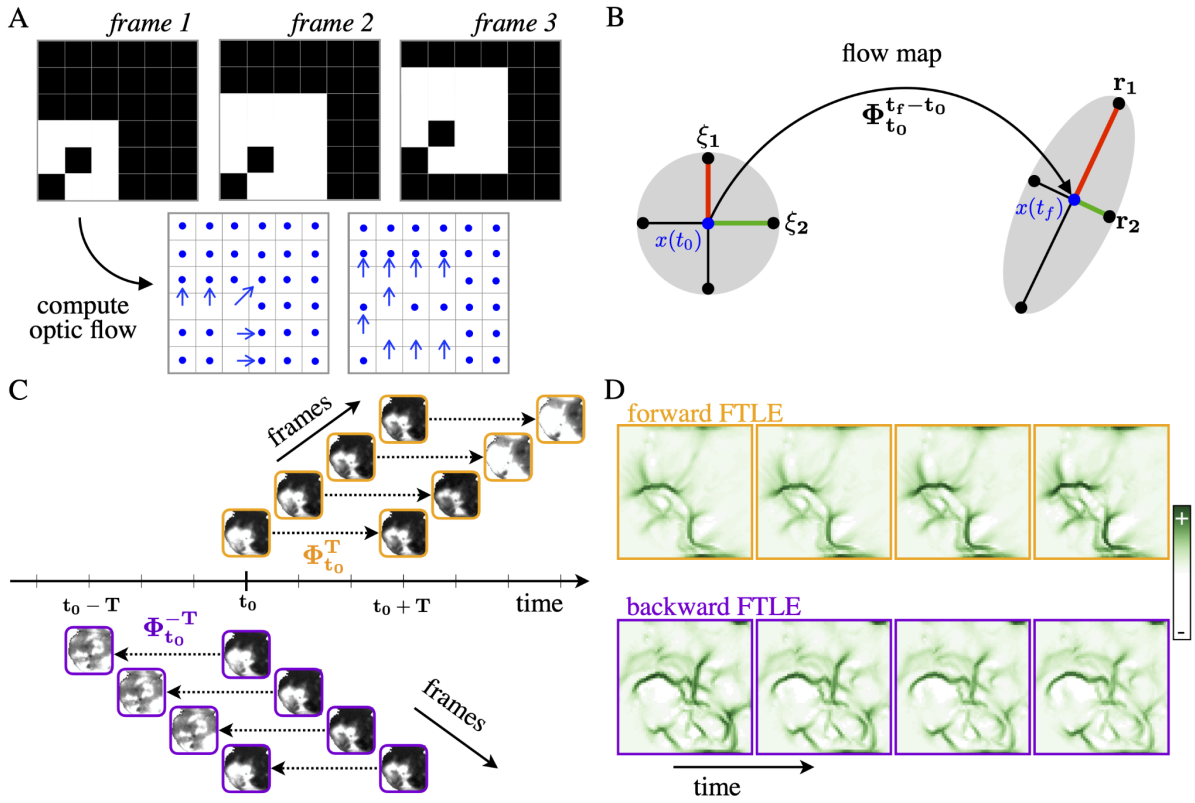

Figure 2: Finite Time Lyapunov Exponent (FTLE) fields are computed from spatiotemporal data. (A) An illustration of how optic flow is computed from successive frames of images by correlating the relative movement of pixel intensities. This procedure converts widefield imaging data into a vector field of velocities. (B) The flow map at every pixel location is a virtual particle at x integrated through the vector field for a duration of T, from t0 to t0+T; in reverse time, particles are integrated from t0 to t0 T. This integration stretches neighboring particles in some directions (r1) and compresses them in others (r2). (C) The flow map computation is repeated starting at each frame of the movie, at base time t0+kt, where t is the separation between frames; forward maps are orange and backward maps are purple. (D) The FTLE fields are computed from the Jacobians of these flow maps; example FTLE fields are illustrated for successive frames of widefield imaging data.

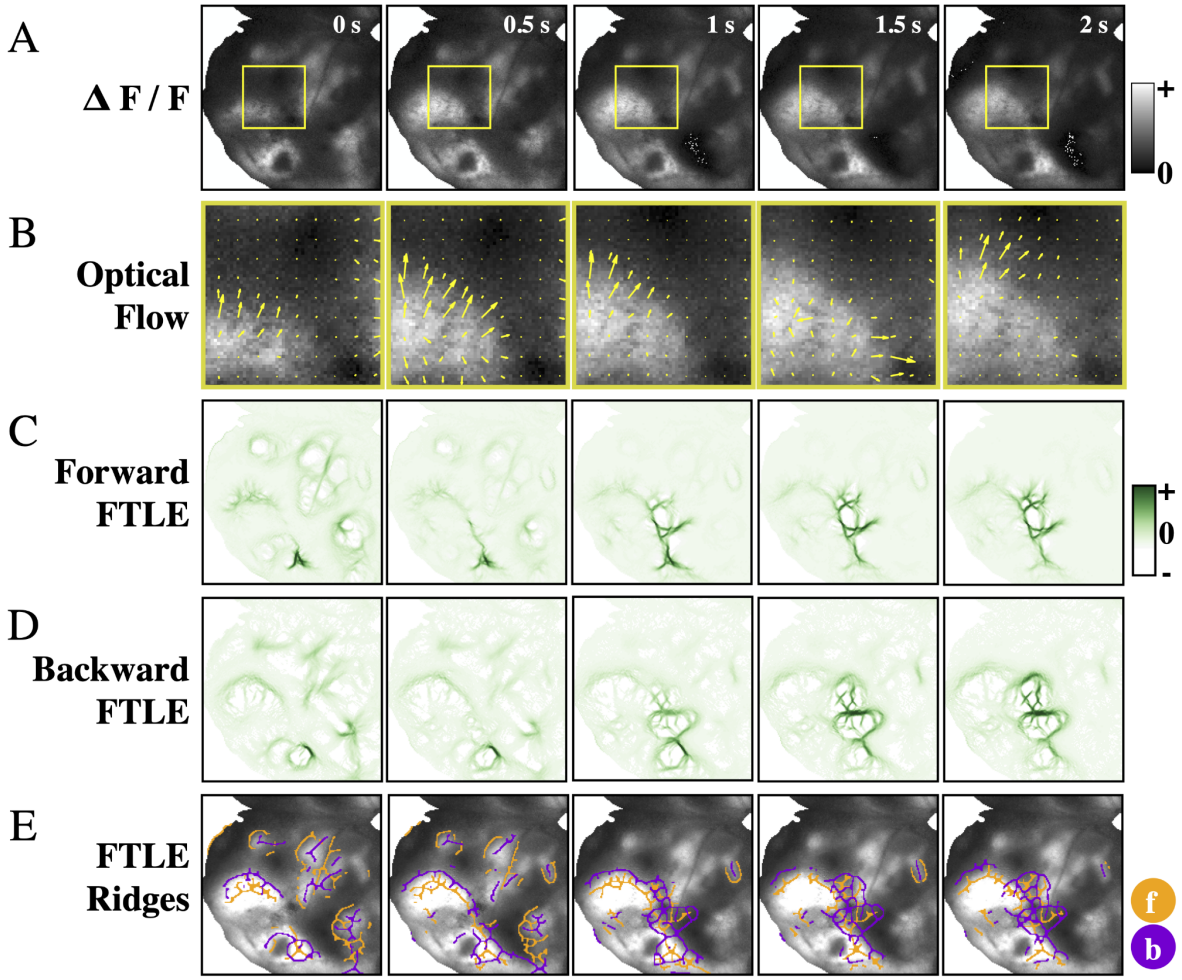

Figure 3: Steps to compute a FLOW portrait. Starting with widefield data preprocessed as F=F (A), optical flow is used to convert the frame-by-frame changes in pixel intensity to a vector field, shown zoomed in for the smaller area outlined with the yellow box and at 1=6 spatial resolution for clarity (B). Next, the FTLE fields are computed in forwards (C) and backwards (D) time using an integration length of 2 seconds (40 frames); here we show only the non-negative Lyapunov exponents. Ridges of these fields highlight coherent structures of the flow (E), and these ridges are used to compute the final FLOW portrait (see Figure 4). The threshold percentile was set to 93 percent. The forward time FTLE ridges (orange) highlight regions that repel flow, while the backward time ridges (purple) show regions that attract activity. Note that ridges in neighboring frames are similar but do vary in time.

numerical differentiation on the optical flow field, we apply temporal scaling and smoothing to the computed vector fields. Briefly, the magnitude of each optical flow vector is scaled proportionally to the relative change in the raw pixel intensity for the corresponding pixel over a prescribed time delay. This scaling attenuates the magnitudes of vectors that do not represent corresponding changes in the widefield imaging data. To mitigate the effects of pixel noise, we also apply temporal Gaussian smoothing to the scaled vector fields. The scaled and smoothed Horn-Schunck optical flow vector fields are used throughout the rest of the FLOW portrait algorithm where velocity data is required. This process of computing the optical flow vector field from widefield imaging data is analogous to the process of extracting the motion vector field from particle image velocimetery (PIV) data [78, 79] in experimental fluid dynamics. Both approaches approximate the velocity field from experimental data of material transported through the studied flow.

2.2 The Finite Time Lyapunov Exponent (FTLE)

Once a flow velocity field, v(x, t), is computed, there are numerous computational approaches that can be performed to study and characterize the flow. These methods include instantaneous metrics from vector calculus, such as the divergence and the curl of the vector field, modal decomposition techniques [80, 81], such as POD and DMD, and Lagrangian metrics such as the FTLE [59, 61, 62]. Although instantaneous metrics have the potential to extract relevant features from widefield imaging optical flow fields (Supplemental Figure 1; [57]), the unsteady nature of this data suggests that Lagrangian metrics may provide a more useful summary of the activity.Here we compute the FTLE fields [62] to extract time invariant features of flow-like widefield activity.

The FTLE field is a scalar field $\sigma(x, t0, T)$ defined at every point in space x and time t0, with respect to some relevant time-scale of integration, T. The FTLE field is a measure of how much neighboring initial conditions separate when integrated through the velocity field v for a duration T. Thus, regions of high stretching for positive T (forward time) or negative T(backward time) provide time-varying analogs of stable and unstable manifolds, respectively [39, 61, 62]. The FTLE field is typically approximated numerically from flow field snapshots at discrete instants in time [62, 65]. First, the flow map $\Phi_{t_0}^{T}$ is approximated on a discretized set of spatial points, typically the same discretized domain where the velocity field is defined. The flow map $\Phi_{t_0}^{T}$ describes the position of an initial condition $x(t_0)$ after it is integrated along the vector field v for a duration T, and is defined as

$$\mathbf{x}(t_0 + T) = \Phi_{t_0}^{T}(\mathbf{x}(t_0)) = \mathbf{x}(t_0) + \int_{t_0}^{t_0+T} \mathbf{v}(\mathbf{x}(\tau), \tau)\, d\tau. \tag{1}$$

Next, the flow map Jacobian $\mathbf{D}\Phi_{t_0}^{T}$ is approximated via finite-difference derivatives with neighboring points in the flow. In two-dimensions, the flow map Jacobian at a point x is:

$$\mathbf{D}\Phi_{t_0}^{T}(\mathrm{x}) \approx \begin{bmatrix} \frac{\Phi_{x,t_0}^{T}(\mathbf{x}+\Delta x)-\Phi_{x,t_0}^{T}(\mathbf{x}-\Delta x)}{2\Delta x} & \frac{\Phi_{x,t_0}^{T}(\mathbf{x}+\Delta y)-\Phi_{x,t_0}^{T}(\mathbf{x}-\Delta y)}{2\Delta y} \\ \frac{\Phi_{y,t_0}^{T}(\mathbf{x}+\Delta x)-\Phi_{y,t_0}^{T}(\mathbf{x}-\Delta x)}{2\Delta x} & \frac{\Phi_{y,t_0}^{T}(\mathbf{x}+\Delta y)-\Phi_{y,t_0}^{T}(\mathbf{x}-\Delta y)}{2\Delta y} \end{bmatrix}, \quad (2)$$

where Φ_{x,t_0}^{T} denotes the x component of $\Phi_{t_0}^{T}$ and Φ_{y,t_0}^{T} denotes the y component. The finite-time Lyapunov exponent $\boldsymbol{\sigma}$ is finally computed from the largest eigenvalue $\lambda_{\max}$ of the Cauchy-Green deformation tensor $\Delta = \left(D\Phi_{t_0}^{T}\right)^{T} D\Phi_{t_0}^{T}$, which is the maximum singular value of the flow map Jacobian:

$$\boldsymbol{\sigma}(\mathrm{x}_0, t_0, T) = \frac{1}{|T|} \ln\left(\sqrt{\lambda_{\max}\left[\boldsymbol{\Delta}(\mathrm{x}_0, t_0, T)\right]}\right). \quad (3)$$

The FTLE value at a point x0 determines the maximum stretching that may occur between x0 and a perturbed location $\mathrm{x}_0 + \epsilon$ after time T:

$$\boldsymbol{\Phi}_{t_0}^{T}(\mathrm{x}_0 + \boldsymbol{\epsilon}) \approx \boldsymbol{\Phi}_{t_0}^{T}(\mathrm{x}_0) + \mathbf{D}\boldsymbol{\Phi}_{t_0}^{T}(\mathrm{x}_0) \cdot \boldsymbol{\epsilon}, \quad (4)$$

where the amplification of the perturbation is bounded by

$$\|\mathbf{D}\boldsymbol{\Phi}_{t_0}^{T}(\mathrm{x}_0) \cdot \boldsymbol{\epsilon}\|_2 \leq \exp(\boldsymbol{\sigma}|T|)\|\boldsymbol{\epsilon}\|_2. \quad (5)$$

The $\boldsymbol{\sigma}$ term is understood to depend on x_0, t_0, and T.

The FTLE field is quite robust to noisy measurements of the vector field v(x, t) [59], since the computation involves integration in time, which tends to average out noise. This robustness was a major factor in its wide adoption in fluid mechanics, where experimentally acquired velocity fields often contain noise and outliers. The same robustness is appealing for optical widefield imaging.

Figures 2 and 3 illustrate the intuition behind this FTLE computation, and additional implementation details are provided in the Methods. The key insight in the FTLE computation is that virtual particles at every pixel location flow according to the vector field from t_0 to $\mathrm{t}_0 + T$, and these integrated optical flow fields form a flow map $\Phi_{t_0}^{T}$ (Figure 2B). This flow stretches neighboring virtual particles, so that equidistant particles have stretched in some directions and compressed in others (see also Supplemental Movie 1). Relative deformations are described by the Cauchy-Green strain tensor at every pixel, and the FTLE

corresponds to the log-normalized leading eigenvalue of this tensor. The same procedure is repeated by reversing the ordering of frames to compute flow maps in backwards time. The forward and backward FTLE fields computed for each example time snapshot are shown in Figure 3C and D.

Drawing again on our analogy to physical fluid flows, ridges in the FTLE field correspond to time varying analogs of invariant manifolds, and they approximate LCS [60, 61]. In forward time, these features repel fluid material, similar to a stable manifold in a dynamical system. The opposite is true for backward time ridges, where material is attracted in forward time, as with the unstable manifold. A similar interpretation can be extended to the FTLE of optical activity flows, where forward time structures repel activity, while backward time structures attract activity. However, additional care must be taken when interpreting the intensity of FTLE ridges for brain activity, since the induced velocity field is not divergence free, as is typically the case when analyzing incompressible fluid systems. When the velocity field is incompressible, then the determinant of the flow map Jacobian is equal to one, so the largest eigenvalue is greater than or equal to one. However, for compressible vector fields (as is in the case for widefield imaging of neural activity), the divergence is nonzero and the product of the eigenvalues of the flow map Jacobian may not equal to one. In this case, we may locally have two positive or two negative Lyapunov exponents. Here we consider only the non-negative Lyapunov exponents, which correspond to repelling ridges in forward time and attractive ridges in backward time (Figure 3C and D).

2.3 Ridge extraction for FLOW Portrait visualization

By aggregating the forward and backward FTLE ridges within a window in time, we summarize the coherent structures of propagating activity within that window with a single FLOW portrait. Ridges of an FTLE field have been shown to approximate LCS, and several mathematical definitions are suggested to extract them from data [60, 62, 82, 83]. We found that implementing existing strategies for ridge extraction on FTLE of widefield calcium imaging data did not adequately extract ridge-like features. Therefore, we developed a post-processing approach to visualize ridges from the forward and backward mean FTLE fields. Ridges lie along local extremes in a field, thus we can approximate their locations by extracting maximal regions and computing the skeleton structure. To compute the dominant features over the entire recording, we first threshold the mean of all non-negative FTLE values, to isolate local maxima in the field (Figure 4B). Next, we approximate ridges from the local FTLE maxima by performing a morphological skeletonization operation (Figure 4C). Lastly, these ridges are smoothed by applying morphological image processing (Figure 4D). Thus, the resulting visualization depicts the average approximate FTLE ridges in a recording window to summarize the time invariant patterns of activity. We refer to this visualization as FLOW portraits because it is designed for compressible vector fields typical of widefield imaging of calcium activity. There are two parameters the user must choose: the integration time T for the flow map $\Phi_{t_0}^{T}$ and the threshold percentile for FTLE values to include in the visualization. The choice of these parameters depends on knowledge of the timescales of relevant coherent activity propagation in each dataset. Larger integration time windows filter out shorter timescale waves; lower percentile thresholds admit more ridges

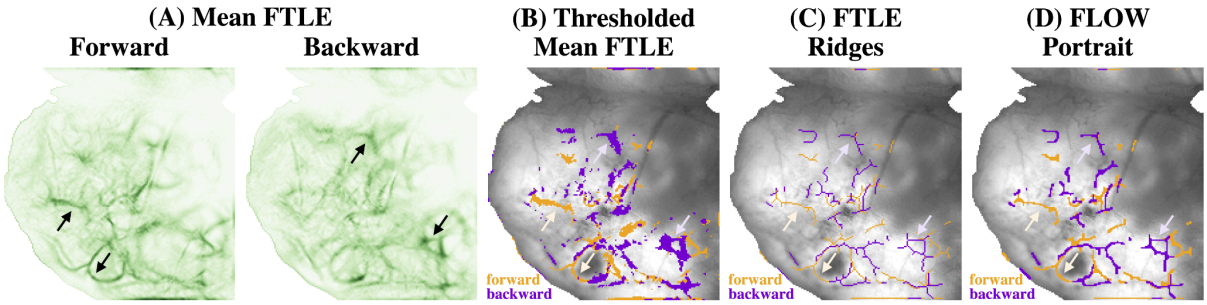

Figure 4: Ridges in the FTLE field are extracted to form the FLOW portrait. (A) The forward and backward FTLE fields are separately averaged to aggregate flow structures over time. Black arrows indicate examples of FTLE ridges which are extracted in the following analysis. (B) Next, the mean FTLE fields are binarized using a threshold which is chosen by the user at a specified percentile (denoted the threshold percentile; here this is chosen to be the 95th percentile). The binary forward and backward FTLE fields are shown overlaid on the mean F=F image. Pale orange and purple arrows show the same forward and backwards ridges as in (A); pale orange corresponds to the forward time ridges and pale purple to those in backward time. (C) Ridges in the FTLE are approximated by performing a skeletonization procedure on the binarized FTLE fields. (D) Lastly, FLOW portraits are produced by further morphological image processing to smooth the approximate FTLE ridges. The final FLOW portrait highlights the example ridges observed in the original mean FTLE fields.

with less intense coherence, which can also admit more spurious ridges if the data are noisy. Supplementary Figure 4 shows how a range of these parameters yields different FLOW portraits. As a practical recommendation to users, we recommend repeating the computation for a range of parameter values so that the visually salient features in a dataset are reflected in the FLOW portraits.

2.4 How to interpret a FLOW portrait

To build intuition and illustrate how spatiotemporal patterns are visualized by FLOW portraits, let's examine them for several simple synthetic datasets, each capturing the types of coherent activity commonly observed in widefield calcium imaging. The first example is a plane wave that starts in the middle of the field-of-view and travels to the right (Figure 5A). In the corresponding FLOW portrait, the forward time FTLE structures delineate where the wave originates in the middle of the field-of-view, while the backward-time FTLE structures outline where the wave terminates (Figure 5B). This type of traveling plane wave closely resembles spread of neural activity observed by widefield imaging (for instance, data from mouse pup in Figure 5). The second synthetic dataset is a circular wave that initiates in the middle, then grows larger towards the edges (Supplemental Figure 2). Here, the forward-time FTLE structures mark the site of initiation, while the backward-time FTLE structures outline the maximal spatial extent of the circle's spread. Our third synthetic example combines both traveling and growing/shrinking wave fronts. As shown in Figure 1 and Supplemental Figure 2, the 2D Gaussian dataset includes a Gaussian blob that appears in the field-of-view, grows in diameter, translates to the right, then shrinks. Forward-time FTLE structures capture where the activity originates, including the back edge of the Gaussian as it starts to translate and the outside perimeter of the blob as it shrinks. Similarly, backward-time FTLE structures capture where the activity terminates, including the outside perimeter of the blob as it grew and the center of the shrinking blob.

In all of these examples, FLOW portraits represent succinct summaries of spatiotemporal coherent activity, highlighting regions of activity initiation and termination, as well as the direction and spatial extent of how activity spreads. Specifically, activity originates from the forward-time FLOW ridges (orange lines, analogous to stable manifolds) and goes to the backward-time FLOW ridges (purple lines, analogous to unstable manifolds). This visualization caricaturizes features of coherent activity not accessible by established methods, including modal decomposition (Figure 1), instantaneous metrics like divergence and curl (Supplemental Figure 1), and source/sink classification of fixed points (Supplemental Figures 2 and 3). The forward and backward time FTLE structures carry more information than sources and sinks because they are not constrained to be fixed points; thus, these structures are able to delineate traveling fronts. The intersection of two or more FLOW structures, such as where the orange and purple ridges intersect in Figure 1B, can occur for several reasons. First, intersections of the forward and backward FTLE ridges are reflected as intersections in the FLOW portraits. Points where these FTLE ridges intersect correspond to time-dependent saddle points, as the forward and backward FTLE ridges are time-dependent analogs of the stable and unstable manifolds of the vector field. Second, two different spatiotemporal structures may occur at the same spatial location at different times during the recording, as in the case of the 2D Gaussian synthetic dataset.

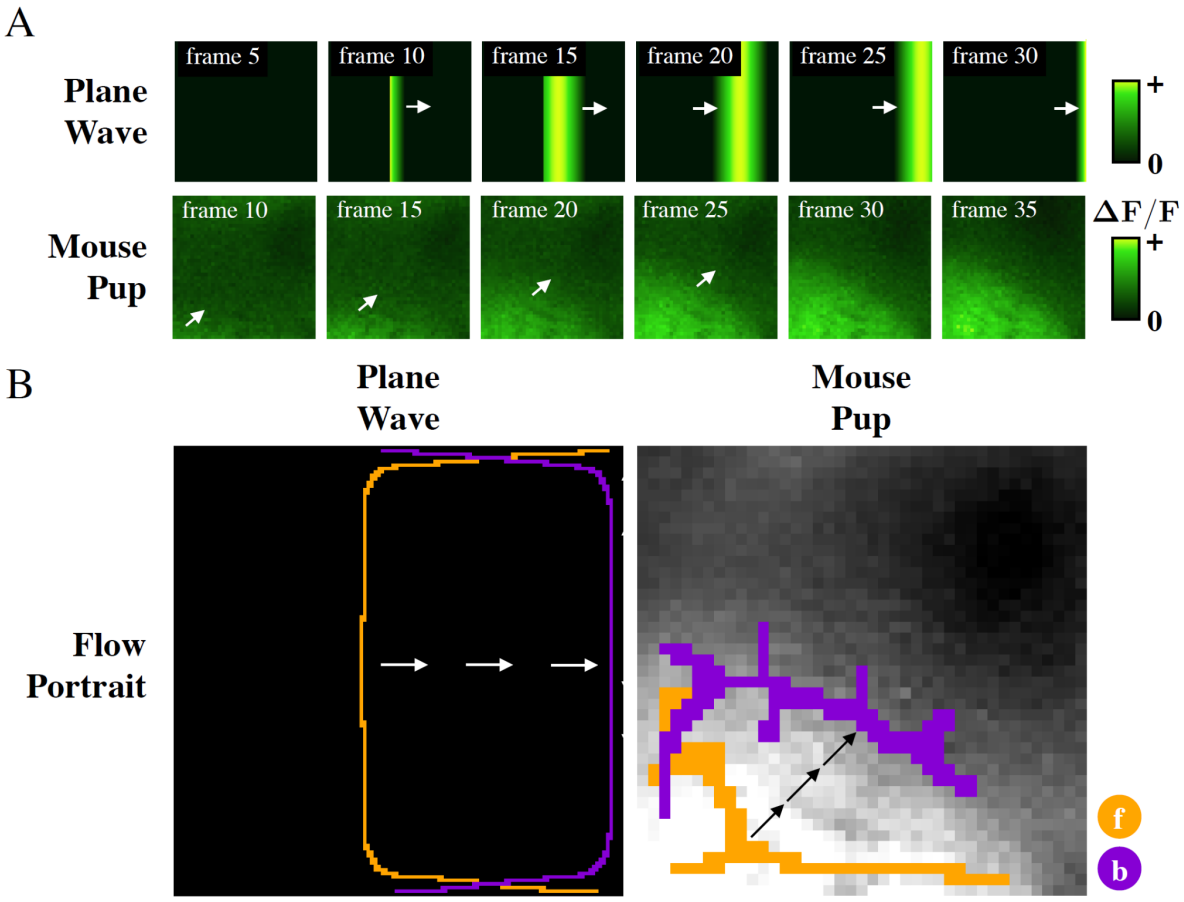

Figure 5: FLOW portraits summarize the activity within a segment of data by highlighting where activity begins and ends. (A) Simple traveling waves for which we illustrate FLOW portraits. The 'PlaneWave' example shows a synthetic traveling wave which begins in the center of the frame and travels to the right. The 'Mouse Pup' example shows a short traveling wave within a segment of widefield calcium imaging experiment of a P7 mouse pup. White arrows indicate the direction of activity propagation. (B) The FLOW portraits for both waves highlight the regions where the wave begins and where the wave ends. Arrows (black and white) show the general direction of wave propagation. FLOW portraits were computed with integration lengths of 15 frames and 5 frames and the threshold percentile was set to the 91st and the 90th percentiles for the plane wave and mouse pup datasets, respectively.

3 FLOW portraits of widefield calcium imaging data

We demonstrate the application of our approach on several optical widefield datasets, all recordings of spontaneous calcium activation imaged from the cortical surface of transgenic mice. In each example, we have chosen to focus on windows in time when bouts of activity are observed across large portions of cortex. We show that FLOW portraits extracted from these windows summarize the extent and direction of calcium flow, highlighting cortical areas whose neural activations can be interpreted in the context of the behavioral and developmental context of the animals.

3.1 Example 1: Pan-cortical waves

Pan-cortical waves are bouts of activity that propagate across large areas of the cortex [5, 84–87] and are suggested to play a critical role in cortical development [38]. These events are defined heuristically by simultaneous activity of a large fraction of the imaged cortical surface. In Figure 6A, the gray bars highlight individual cortical wave events, defined as when the fraction of active cortex rises to above 1/2 and falls back to the baseline (1/10). To contribute to our understanding of pan-cortical waves in development, we use FLOW portraits to summarize the activity during each wave event, thus facilitating direct comparisons across individual waves and developmental time points.

We construct FLOW portraits to summarize the flow of activity during each pan-cortical wave. Spatial integration of the FTLE fields yields the FTLE intensity (Figure 6A, orange and purple traces), which indicates the relative amount of time-averaged flow throughout the recording. The resulting FLOW portraits for two pan-cortical waves can be seen in Figure 6B, alongside 12 frames of the $\Delta F/F$ data from each wave (see also Supplemental Movies 2 and 3). The portraits of every pan-cortical wave are shown in Supplemental Figure 2. Each FLOW portrait provides a summary of the prominent activity observed during each wave event, highlighting the source (forward FTLE, orange) and sink (backward FTLE, purple) features. Indeed, both waves shown in Figure 6B exhibit two stages of propagation, where activity spreads and pauses briefly at sensorimotor cortex (outlined by the purple rings) before spreading towards frontal cortex. This concise visualization allows us to easily compare such qualitative features of wave propagation without having to parse through the raw data manually.

3.2 Example 2: Sleep-state cortical activity changes in development

To further investigate the role of spontaneous cortical activity during development, we analyzed optical recordings of spontaneous calcium activity in mouse pups during the first 8 postnatal days of development. We computed FLOW portraits on bouts of spontaneous cortical activity during sleep in 12 animals of ages P1, P2, P3, P5, P7 and P8 (Figure 7). Briefly, the sleep state was determined by binning time points into three categories (sleep, wake, and moving-wake) using the power of nuchal EMG spectrum [38, 88, 89]. We chose to focus on sleep state cortical activity for its proposed developmental roles and observed changes during development [38]. For each animal, we computed FLOW portraits for up to the 10 longest bouts of sleep (fewer portraits were computed for short recordings where there were less than 10 sleep bouts). Five (5) example FLOW portraits for each animal are in Figure 7A, with a complete set in Supplemental Figure 6. This organization allows us to

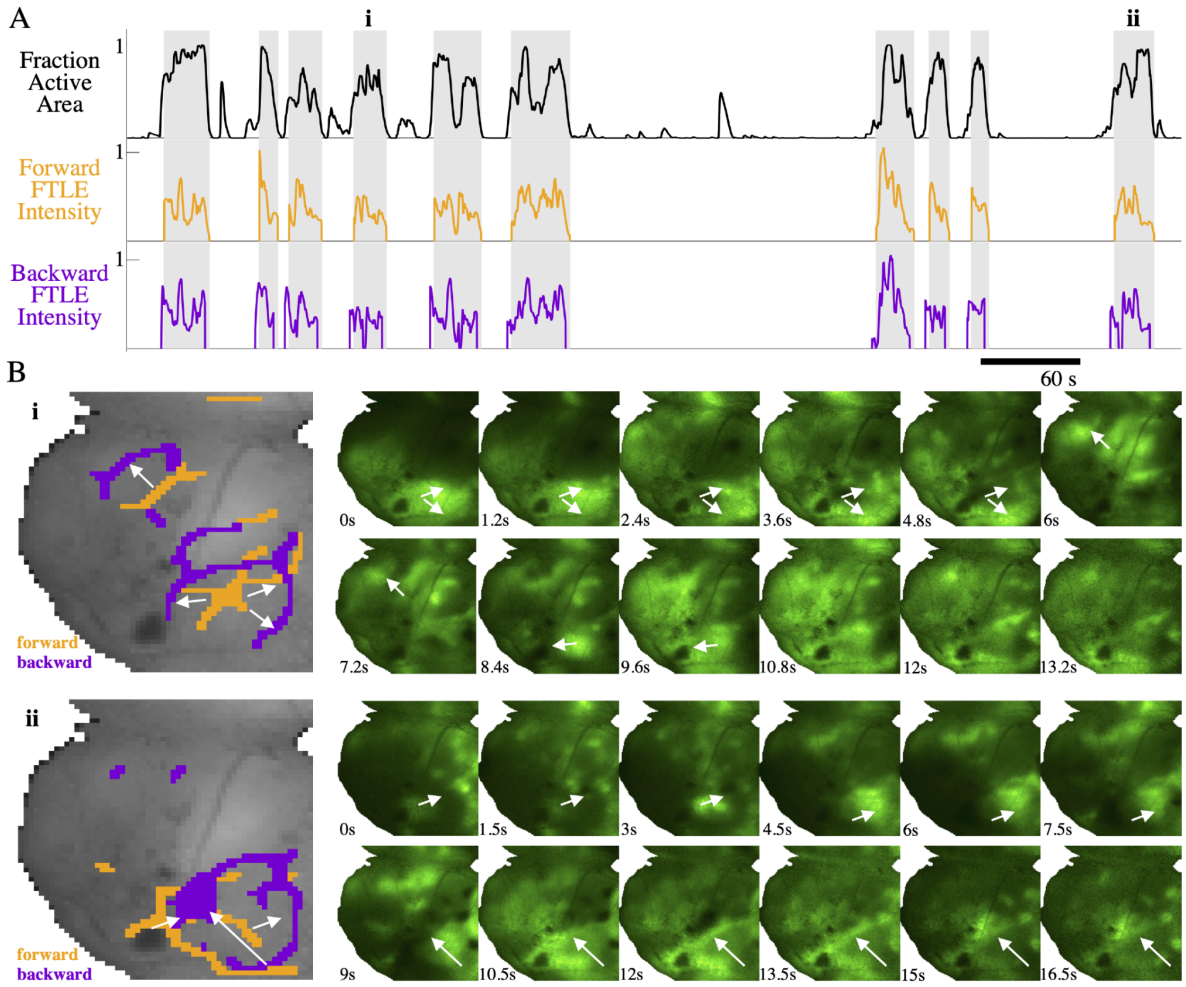

Figure 6: Pan-cortical wave events in a P7 mouse pup are summarized as FLOW portraits. (A) Pan cortical waves are defined as events where the fraction of active cortex (black-trace) exceeds 50-percent. Briefly, the fraction of active cortex is defined as the fraction of pixels whose intensity is greater than one standard deviation above the mean (in time) for that pixel. FTLE intensity is defined as the sum of the FTLE values for each frame, normalized by the maximum value in time; this intensity is computed for both the forward and backward FTLE time series. (B) FLOW portraits are shown for two example waves, indicated by i and ii in A. Orange indicates forward time FTLE ridges where calcium activity originates. Purple indicates backward time FTLE ridges where calcium activity propagates towards. White arrows highlight the general direction of activity propagation during the cortical wave. The FLOW portraits are computed using an integration length of 2 seconds (40 frames) and a threshold percentile of 93 percent.

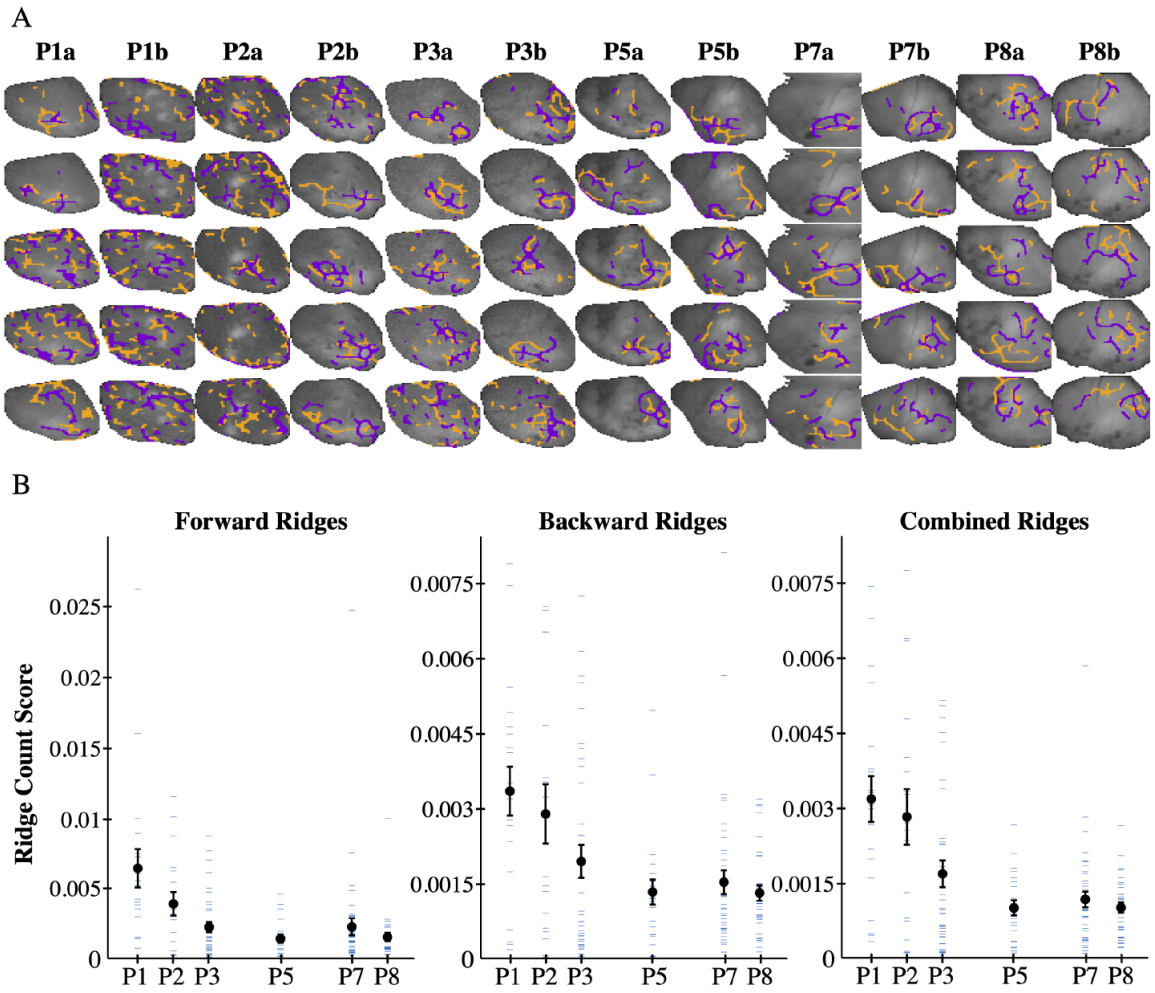

Figure 7: FLOW portraits highlight developmental changes of sleep-state cortical activity. (A) FLOW portraits for 5 sleep bouts from 12 P 1-8 mouse pups are shown. During the first 3 postnatal days, activity is diffuse, as indicated by many short-length structures in the FLOW portrait. As animals grow older (postnatal days 5-8), sleep-state cortical activity becomes more structured, as indicated by a consolidation of features in the FLOW portraits. Orange indicates repelling or source structures, and purple indicates attracting or sink structures. All images are of the left-hemisphere, such that the midline and anterior directions are oriented towards the bottom and left of the images, respectively. FLOW portraits were computed using an integration length of 2 seconds (40 frames) and a threshold percentile of 93 percent for all sleep-bouts shown. (B) Quantification of the number of FLOW ridges seen versus developmental day. The ridge count score for a FLOW portrait is computed by counting the number of FLOW ridges, either forward, backward, or both combined, and dividing by the total area of FLOW ridges in that portrait. When the ridge count score is high there are many smaller ridges in the image, whereas when the score is low there are fewer ridges with a larger ridge area. Here, the mean ridge count score (black point) decreases between developmental day one and day five and then remains constant. Further, the mean ridge count score over days P1-P3 (0.0038, 0.0027, and 0.0022 for forward, backward and combined, respectively) is significantly different than the mean ridge count score over day P5- P8 (0.0019, 0.0015, and 0.0010 for forward, backward and combined respectively; paired t-test, p-values 8.7×10^{-4} 7.16×10^{-5}, and 1.62×10^{-7} for forward, backward and combined, respectively). Blue dashes show individual data points; the ridge count score for an individual FLOW portrait. Error bars show ± 1 standard error measure.

leverage FLOW portraits to examine developmental changes in cortical activity across long recordings from different animals. We observe a qualitative change between the portraits from the early postnatal days (P1–3) to the later days (P5–8). The FLOW portraits from the early days show more diffuse activity, with less consolidated FTLE ridges. After P5, the FLOW portraits show cortical activity during sleep becoming more consolidated and following more defined flow patterns. Thus, we may easily visualize how cortical activity during sleep undergoes a substantial change during development. We quantify this transition to more consolidated FTLE ridges after P5 by defining a ridge count score. Briefly, this metric is computed by counting the total number of disconnected ridges in a FLOW portrait and dividing this sum by the total area of the FLOW portrait. We computed ridge count scores for all FLOW portraits seen in Supplemental Figure 6 and summarized the mean over each developmental day (Figure 7B). We found that the ridge count score for forward FTLE structures, backward FTLE structures, and both combined all decreased between P1 and P5. Further, we found that the mean ridge count score over the early developmental days (P1–3) was significantly different (p-values of 8.70×10^{-4}, 7.16×10^{-5}, and 1.62×10^{-7} for forward, backward, and combined, respectively; paired t-test) than that over the later developmental days (P5–8).

3.3 Example 3: Cortical activity during spontaneous movement

Lastly, we analyze the FLOW portraits of spontaneous cortical activity in a head-fixed, behaving adult mouse [35]. To investigate how FLOW portraits align with an animal's behavior, we analyze IR videos of spontaneous facial and limb movements alongside cortical calcium activity. A movement score was assigned to each recording time point by using the total pixel-wise difference between the current and next frames (the forward difference) and normalizing this to the maximum observed difference. During bouts of limb movement or whisking the movement score was greater, approaching the maximum score of 1, than during periods of rest, when the score approached the minimum score of 0.

We chose two bouts of spontaneous movement (gray shading in Figure 8A highlights the two bouts, i and ii) to compute the corresponding FLOW portraits (see also Supplemental Movies 4 and 5). Large variations in the movement score (Figure 8A, blue trace) can be observed throughout these bouts, indicating that the animal is continuously switching from a resting to a moving state. We see signatures of these movement behaviors in the calcium activity, when we expect sensorimotor cortical regions to be more active than during periods of rest. Indeed, the FLOW portrait for each activity bout provides a clear summary of calcium activity surrounding the sensorimotor cortex (Figure 8B). During both bouts, a ring-like repelling (forward, orange) field line outlines the sensory-motor region, while attracting (backward, purple) field lines fill in the centers of the rings. We note that these patterns are different from our analysis of Example 1 of pan-cortical waves. Specifically, these features suggest a dominant pattern of cortical calcium activity as diffusion of activity from the entirety (or outer edges) of sensorimotor regions towards the center. In other words, our FLOW portraits point to sensory-motor cortex as a sink of cortical activity during spontaneous movement behaviors. Interestingly, compared to the overlaid Allen Mouse Brain Common Coordinate Framework (white lines in Figure 8B), the attracting (backward, purple) field lines are close to the boundary between somatosensory and primary motor cortices. We

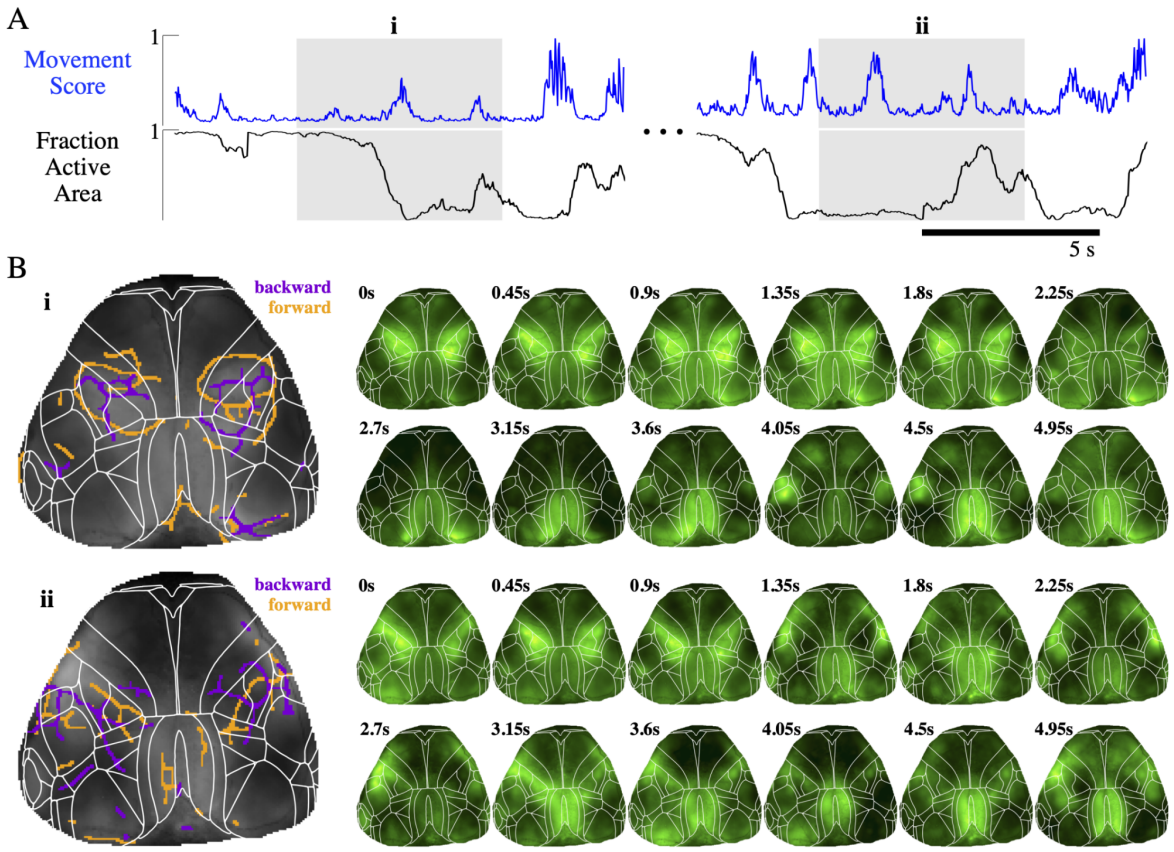

Figure 8: Examples of spontaneous cortical calcium activity associated with movements of an adult mouse summarized as FLOW portraits. (A) A movement score extracted from IR video of the mouse moving spontaneously in the dark shows bouts of large movements among more quiescent periods. These bouts of movements do not correspond necessarily to when a large fraction of the cortical surface is active (see Methods for threshold criteria). (B) FLOW portraits for two bouts involving spontaneous movements labeled i and ii show coherent structures that highlight activity appear in sensorimotor regions and are then attracted to the centers of these regions bilaterally. Boundaries aligned to the Allen Mouse Brain Common Coordinate Framework [90] are overlaid in white. FLOW portraits were computed with a 15 frame integration length and threshold percentile of 93 percent.

note that the integration length and the threshold percentile parameters chosen for these examples determine which ridges are highlighted in the FLOW portraits.

4 Discussion

This paper introduces FLOW portraits as a novel approach to visualize spatiotemporal flow of coherent features in optical widefield calcium imaging data. Viewed at this meso-scale of temporal and spatial resolution, neural activity at the cortical surface is typified by multiple brain regions activating transiently and sometimes in spatial succession. Motivated by an analogy between this flow of neural activity over cortex and physical fluid flows, we leverage techniques well established to study physical fluid flows, in particular the finite-time Lyapunov exponent (FTLE). Here we convert movies of $\Delta F/F$ over the cortical surface into vector fields, and the FTLE ridges in these vector fields form an intuitive map of dynamic calcium activity. Importantly, our FLOW portraits do not decompose the data into modes and are not models of the data. Instead, they capture succinct portraits of diverse, variable, and non-stationary spatiotemporal patterns, such as those often observed in spontaneous or task-driven widefield calcium imaging experiments.

The FLOW portrait analysis makes several assumptions that are usually true of physical fluid systems but often not met by neural data. Coherent propagation of neural activity on the cortex does not obey mass or energy conservation, so the extraction of FTLE ridges are only approximate “material” accumulation lines. This assumption is particularly invalid for long bouts of data and over long integration windows, so caution must be exercised in choosing these parameters in the analysis (the same is true of FTLE analysis in fluid flows). Because the integration window effectively low-pass filters the dynamics of the data, activity that is on a faster timescale may be attenuated, and local activity may integrate to appear more coherent. The optimal choice of FTLE parameters for visualization widefield activity and how these depend on spatiotemporal statistics will be important to understand in future applications. Further, although widefield imaging offers much larger fields of view at a higher temporal resolution than many other imaging methods, there remains much unobservable neural activity. Brain areas outside the imaging window and underneath the cortical surface contribute to the imaged activity, yet the flow of neural activity among these regions cannot be captured by our analysis and may bias the extracted flow lines. This limitation is more severe in considering brains with sulci and gyri, as our analysis fundamentally assumes that neighboring pixels are also neighbors on the cortical sheet.

The quality and interpretability of FLOW portraits requires the imaging data to have been acquired with sufficient temporal and spatial resolution to support the analysis. To be specific, we require that the sampling in time to be fast enough that successive frames of the movie are very similar. If the frame rate is too slow and neighboring frames differ substantially, then the optical flow computation infers inaccurate vector fields and can no longer disambiguate between gradual flow of activity and sudden jumps in activation. Despite the relatively slow dynamics of GCaMP6s compared to single neuron activity [27], the temporal dynamics of lasting neural synchrony at this meso-scale is adequately matched to the kinetics of the indicator protein in all the data we highlight here. The choice of calcium or voltage indicator also introduces filtering in time, so that our analysis relies on the dynamics of the indicator to be faster than the dynamics of the underlying flow across the

brain. Similarly, the spatial resolution of the data need not support disambiguation of single neurons, but it is important that spatial averaging in the field of view does not obscure coherent features of interest.

We suggest our approach expands our toolbox of techniques to analyze and understand widefield imaging data, especially facilitating direct comparison of multiple bouts of spatiotemporal activity that are interpretability in the context of behavior and development. This visualization framework can be developed to explicitly quantify features of the flow (for example, the ridge count score analysis in Figure 7). Such quantification may be of value in further work that connects features of FLOW portraits with states of relevance to behavior, development, or disease. The transformation of widefield calcium imaging data into a vector field representation suggests multiple avenues for development of analytic tools. For instance, where multiple coherent waves are present and propagate locally, future work may develop visualizations of the direction of activity propagation, from individual forward FLOW ridges to backward FLOW ridges. Intriguingly, it may be possible to discover partial differential equations that govern the flow of activity through these vector fields using data-driven techniques [91, 92].

5 Methods

5.1 Widefield calcium imaging and data preprocessing

5.1.1 Developing mouse datasets

These experimental procedures were conducted at University of Washington, and all protocols were reviewed and approved by the University of Washington IACUC. Neonatal mice expressing GCaAMP6S in cortical neurons were bred by crossing mice heterozygous expressing a Emx1 driven Cre (Emx1-Cre+/-, Jackson Labs ID 005628) with mice homozygously expressing GCaAMP6S under control of a cre promoter (Ai162+/+, Donated by Allen Institute, Jackson Labs ID 031562). This cross resulted in mice expressing GCaAMP6S primarily in glutamatergic cortical neurons early in development. On the day of recording, mice were placed on a heating pad and anesthetized using 1–2% isoflurane carried by 100% O_2, while local anesthetic bupivacaine was delivered subcutaneously at the scalp. The skin over the cortex was removed over a window spanning between the ears to just above the eyes of the pup, to reveal the skull. The periosteum was then removed with fine tip forceps and cotton swabs. At this developmental stage, the skull is uncalcified and largely transparent, so thinning or cutting a window was unnecessary. A stainless steel U-shaped bracket was then attached to the skull with cyanoacrylate glue. The bracket was clamped in place to the heating pad and stage to stabilise the head. To prevent the skull from drying and to preserve clarity, the exposed skull was also sealed with a thin layer of cyanoacrylate. Silver wire hook leads were implanted into the nuchal muscle through the same incision to monitor neck electromyography (EMG).

Once glue had dried, isoflurane anesthesia was removed and the pup along with heating pad and stage was positioned for imaging on a Nikon AZ100 with 2X objective and 0.6X reducer. Nuchal EMG activity was amplified with an AM Systems Model 1700 amplifier (10Hz high pass, 60Hz notch, 10kHz low pass) and was sampled at 10kHz using a Powerlab 4/26 and Labchart v8 (AD Instruments). GCaMPP6s activity was excited using an Intensilight mercury lamp (Nikon), captured using an CCD camera (ORCA Flash 2.8), and

recorded using the HCImage application (Hamamatsu). Frame capture rates varied from 10–50Hz with maximum exposure times (100–20ms, respectively). To further increase signal to noise ratio, the camera was set to perform online hardware based pixel binning, reducing a 1920 1440p image to 960 720p. Individual recordings began when the animal began cycling regularly between sleep and wake, and recordings typically lasted between 40–60 minutes, after which the pup was euthanized.

Ca^{2+} records were processed using MATLAB (Mathworks) to create ΔF/F image stacks for FLOW portrait analysis. Briefly, imaging runs were further downsampled by pixel binning the 960 720p image down to 480 360p. To compensate for slow drift, a moving window of 40-sec was used to calculate baseline F for each frame; each pixel in F was set to the minimum value for that pixel across the 40-sec window. ΔF was calculated as the difference between the raw pixel intensity and this calculated moving minimum. The difference was then normalized to relative change by dividing (ΔF/F). A small Gaussian spatial blur was used to attenuate "speckled" noise. Region of interests (ROI) masks of the visible cortical surface were generated by excluding any pixel whose mean-to-variance ratio was greater than 400:1. This value was determined heuristically to optimize exclusion of any pixels that displayed minimal change in fluorescence over time, such as those that lie outside the cortical window.

5.1.2 Adult mouse dataset

These experimental procedures were conducted at UCL according to the UK Animals Scientific Procedures Act (1986) and under personal and project licenses granted by the Home Office following appropriate ethics review. The dataset and associated procedures were described previously [35]. In brief, the data were from an adult (30 weeks) male mouse expressing GCaMP6s in excitatory neurons (tetO-GCaMP6s; CaMK2a-tTa genotype [11]). The mouse was implanted with a metal headplate, plastic light isolation chamber, and transparent covering over the dorsal skull. On the day of recording, the mouse was head-fixed under the microscope on a stable seat with a rubber wheel underneath the forelimbs. Video cameras captured the frontal aspect of the mouse as well as its eye. Imaging was conducted at 70 Hz with alternating blue and violet illumination, and imaging data was corrected for hemodynamic components. The data were processed by singular value decomposition (SVD) compression.

The images were aligned to the Allen Common Coordinate Framework [90] by manually identifying Bregma and the orientation of the midline in the images. Bregma was taken to be located at the coordinate 5.7 mm AP in the CCF. Since the pixel size in the camera was known (21.7 μm / pixel), the CCF region boundaries could then be overlaid on the images.

5.2 Imaging analysis

5.2.1 Pan-cortical wave segmentation

Pan-cortical, as defined by [38], are cortical activity events where recorded activity spreads over a large area of the imaged cortex. We defined large cortical area to be when 50 percent of the cortical pixels (pixels which show the cortex) are active. At any time point, a pixel is active if its intensity is more than one standard deviation above the temporal mean

for that pixel. To extract pan-cortical wave events, we computed the fraction of active cortical pixels throughout the recording, and noted the time points where the active area exceeded the 50 percent threshold. Each wave event was then defined by the time points when the active area crossed 10 percent active prior to the time of crossing the 50 percent threshold and the time when the active area crossed this 10 percent lower bound following the peak. Overlapping wave events were merged into a signal pan-cortical wave to avoid redundancy. Furthermore, events that lasted less than the FTLE integration length (T) plus the optical flow scaling delay (3.5 sec or 70 frames for the mouse pup data; 0.85 sec or 30 frames for the adult mouse data) were not analyzed because the FTLE and optical flow computations require longer bouts of data.

5.2.2 Sleep bouts during development

Sleep state cortical activity was segmented using the nuchal EMG as an indicator of state (sleep or awake). Time points were clustered into three groups based on the nuchal EMG power spectrum as in [38, 88, 89], where the lowest power group is known to represent the sleep state. We defined a sleep bout as a period of continuous classification in the sleep state, and extracted the 10 longest bouts from each recording over the developmental time span. Any bout that did not meet the FTLE and optical flow length requirement (3.5 sec or 70 frames for the mouse pup data; 0.8 sec or 30frames for the adult mouse data) was not analyzed further. In cases when there were less than 10 bouts that met the length requirement, we chose to include fewer sleep bouts for that recording.

5.2.3 Movement event extraction

We extracted movement events from video of the face and front arms of the adult mouse during the widefield imaging experiment. We defined a movement score for each time point in the video based on the difference between the current time point and the previous time point. Each video frame was assigned a movement score given by the sum (over all pixels in the frame) of the difference between the current and previous frame. For time point t, the score is given by $\text{MovementScore}_t = \Sigma_{pixels}\left(I_t - I_{t-1}\right)$, where I is the pixel intensity for each of the pixels in the frame. The time series of movement scores was normalized to the maximum observed value for ease of interpretation and visualization. Timestamps of video frames were determined by recording TTL pulses emitted by the camera on each exposure, for both calcium imaging and behavioral videos. We then compared cortical activity across varying movement regimes.

5.3 Optical flow computation

5.3.1 Horn-Schunck optical flow

We computed optical flow vector fields using the Horn-Schunck optical flow algorithm [77] implemented in MATLAB [93]. Two parameters must be supplied to the optical flow algorithm: the maximum number of iterations and the α smoothness parameter. Values for both parameters were selected such that the errors in the Horn-Schucnk minimization problem (see [77] for details) were simultaneously minimized. We set the maximum number of iterations to 100 and α to 1 for all computations.

5.3.2 Optical flow scaling and smoothing

To minimize the effects of noise on optical flow fields, we applied an activity-based scaling to the magnitudes of the optical flow vectors. First, we created a time series of weights for each pixel by normalizing change in raw pixel intensity between the current time and the intensity of that pixel 1.5 seconds in the past to the maximum observed change. We chose a time delay of 1.5 and 0.5 seconds, for the developmental and adult mouse datasets respectively, to empirically match the time scale of large changes observed in the raw data. Next, we took the sliding windowed average, over a window of 0.25 seconds, of the weights in order to further reduce the effects of recording noise. We then scaled the magnitude of the optical flow vectors by applying the weights to the corresponding vector. Lastly, we temporally smoothed the optical flow fields using a 5-point Gaussian window created with MATLAB's gausswin() function. The gausswin function takes an additional parameter, α, which is proportional to the inverse of the standard deviation of the Gaussian smoothing kernel. We set this parameter to 1.25 for all smoothing operations for its observed ability to reduce noise in the processed vector fields.

5.4 Finite Time Lyapunov Exponent (FTLE) fields

We computed the FTLE of all vector fields using the LCS Tool [73] (`https://github.com/jeixav/LCS-Tool`) MATLAB software package. We computed the FTLE using an integration length of 2.0 seconds (40 frames) for the developing mouse data and an integration length of 0.5 seconds (15 frames) for the adult mouse data. Additionally, we used an integration lengths of 15 frames, 12 frames, and 10 frames for the plane wave, the circular wave, and the traveling Gaussian examples respectively. To choose the integration length T, we followed the criteria outlined in [62] of choosing a value such that the FTLE ridges are sufficiently resolved. Using a sample of each dataset, we computed the FTLE for a range of integration lengths (0 to 100 frames) and visualized the resulting FTLE fields. We then chose the smallest integration length where the corresponding FTLE field had well resolved, sharp, ridges. Supplemental Figure 4B illustrates the effects of computing FLOW portraits with a range of integration lengths.

5.5 FLOW portrait construction

FLOW portraits are constructed through several image processing steps that aim to extract ridges from an FTLE field (see Figure 4 for a visualization of the intermediate processing steps). It is important to note that we process the forward and backward FTLE fields separately and overlay them on the mean $\Delta F/F$ image to create the final FLOW portrait.

We begin by averaging the FTLE time-series to aggregate the flow features into mean forward and backward FTLE fields. Next, we isolate possible ridge-like features by thresholding the mean FTLE field at a chosen percentile to form a binarized image. This thresholding step is motivated by recognizing that a ridge can be thought of as a continuous path along a local maximum in the field [60, 62]. Therefore, the binarized mean FTLE fields are thought to contain the ridges whose value is above the chosen threshold value. Throughout this work we denote the specified threshold value as a parameter named the

threshold percentile. For each FLOW portrait analysis we choose the threshold percentile to extract the FTLE ridges (see black arrows in Figure 4A for example ridges). Figure 4A and B show the correspondence between the mean FTLE field and the binary versions (the threshold percentile was set to 95 percent). We used threshold percentiles between 90% – 93% for the mouse pup dataset and a threshold percentile of 93% for the adult mouse dataset. Additionally, we thresholded the plane wave, the circular wave, and the traveling Gaussian examples to the 91st, the 93rd, and the 85th percentiles respectively. Supplemental Figure 4C illustrates FLOW portraits computed with a range of threshold percentiles.

Next, we perform two sets of morphological image processing operations on each binarized mean FTLE field to produce the final FLOW portrait. The first set of operations aims to denoise approximate ridges from the FTLE fields. While the second set smooths the ridges to produce the FLOW portrait. We found that these two series of operations provide strong approximations to the ridge features that we observe in the FTLE fields. We use the bwmorph() function in MATLAB for all morphological image processing operations(see `https://www.mathworks.com/help/images/ref/bwmorph.html` for details). This function applies a specified morphological operation iteratively, with the number of iterations specified by the n parameter, or until the input image remains unchanged, n = Inf. Unless otherwise specified, we performed morphological operations until the image no longer changed, with n = Inf. We refer the reader to the MATLAB documentation, Gonzales et al. [94] and Haralick and Shapiro [95] for the mathematical details of each morphological processing operation used.

The first set of operations aims to transform the noisy, disconnected, ridges in the binarized images to connected ridges that resemble those observed in the raw data. First, we perform the IcloseI operation (morphological dilation followed by erosion) to close any gaps within the binary image. Next, we use the `'thin'` operation to thin the blob-like structures seen in Figure 4B to a series of lines. Lastly, we skeletonize the image by applying the `'skel'` (performed with n = 4). Together these operations convert the disconnected, blob-like, structures seen in Figure 4B to the connected, single-pixel, structures in Figure 4C. These skeletonized structures can be thought to approximate the centerlines of the FTLE ridges. The second set of operations aims to smooth the skeletonized image to produce the FLOW portrait. Here we perform the `'diag'` operation to connect regions where two pixels lie corner-to-corner with an additional pixel. We then apply the `'spur'` operation to remove any remaining single pixel spurs from the ridges. Lastly, we close any gaps introduced with the and the `'close'` operation. Lastly, we overlay the processed forward and backward images on the corresponding mean ΔF/F image to create the final FLOW portrait. An example FLOW portrait can be seen in Figure 4D.

5.6 Quantification of FLOW portrait consolidation during development

In order to quantify the consolidation of FLOW portraits during development we computed a metric we denote as the ridge count score. The ridge count score is defined as the number of disconnected ridges in the FLOW portrait divided by the total area of the FLOW portrait. This metric is computed by counting disconnected ridges (objects) in the FLOW portrait and dividing by the total number of pixels included in the FLOW portrait. This score was computed for forward FLOW, backward FLOW and the both combined for each sleep

bout. We then take the mean ridge count score of all sleep bouts from animals of the same developmental age. Lastly, we use a paired t-test to determine whether the mean of mean ridge score for developmental days P1–P3 is statistically different from that for developmental days P5–P7.

5.7 Code and data availability

Our code is publicly available without restriction, other than citation, on Github at `https://github.com/natejlinden/FLOWPortrait`. The code and data in this repository can reproduce all main analyses, findings, and figures from our paper.

Acknowledgements

We are grateful for helpful discussion with Aditya Nair, Kameron Decker Harris, and Seth Hirsh. NJL acknowledges support through a Neuroengineering Undergraduate Research Fellowship from the University of Washington Institute of Neuroengineering (UWIN) and the Washington Research Foundation Funds for Innovation in Neuroengineering. DRT acknowledges funding support from UW Neuroscience Graduate Program (T32NS099578) and the UW Computational Neuroscience Center (5T90DA032436). NAS was supported by the Human Frontiers Science Program (Fellowship LT001071), and the European Union's Horizon 2020 research and innovation programme (Marie Sklodowska-Curie fellowship 656528). WJM acknowledges funding from a Simons Foundation Autism grant. SLB acknowledges funding support from the Army Research Office (ARO W911NF-19-1-0045). BWB acknowledges funding from the Washington Research Foundation, the Alfred P. Sloan Foundation, and Weill Neurohub.

Author contributions

NJL, SLB, and BWB conceived of the study and designed the analyses. NJL carried out the analyses. DRT, NAS, and WJM collected the imaging data and helped interpret the results. NJL and BWB wrote the paper, and all authors contributed to editing the manuscript.

Competing interests

The authors have no competing interests.

References

[1] J. B. Wekselblatt, E. D. Flister, D. M. Piscopo, and C. M. Niell, "Large-scale imaging of cortical dynamics during sensory perception and behavior," Journal of neurophysiology, 2016.

[2] L. Muller, F. Chavane, J. Reynolds, and T. J. Sejnowski, "Cortical travelling waves: mechanisms and computational principles," Nature Reviews Neuroscience, vol. 19, no. 5, p. 255, 2018.

[3] S. Musall, M. T. Kaufman, A. L. Juavinett, S. Gluf, and A. K. Churchland, "Single-trial neural dynamics are dominated by richly varied movements," Nature neuroscience, vol. 22, no. 10, pp. 1677–1686, 2019.

[4] R. Corlew, M. M. Bosma, and W. J. Moody, “Spontaneous, synchronous electrical activity in neonatal mouse cortical neurones,” The Journal of physiology, vol. 560, no. 2, pp. 377–390, 2004.

[5] J. Conhaim, E. R. Cedarbaum, M. Barahimi, J. G. Moore, M. I. Becker, H. Gleiss, C. Kohl, and W. J. Moody, “Bimodal septal and cortical triggering and complex propagation patterns of spontaneous waves of activity in the developing mouse cerebral cortex,” Developmental neurobiology, vol. 70, no. 10, pp. 679–692, 2010.

[6] H. J. Luhmann, A. Sinning, J.-W. Yang, V. Reyes-Puerta, M. C. Stu¨ ttgen, S. Kirischuk, and W. Kilb, “Spontaneous neuronal activity in developing neocortical networks: from single cells to large-scale interactions,” Frontiers in neural circuits, vol. 10, p. 40, 2016.

[7] L. F. Rossi, R. C. Wykes, D. M. Kullmann, and M. Carandini, “Focal cortical seizures start as standing waves and propagate respecting homotopic connectivity,” Nature communications, vol. 8, no. 1, pp. 1–11, 2017.

[8] J. V. Cramer, B. Gesierich, S. Roth, M. Dichgans, M. Du¨ ring, and A. Liesz, “In vivo widefield calcium imaging of the mouse cortex for analysis of network connectivity in health and brain disease,” Neuroimage, vol. 199, pp. 570–584, 2019.

[9] A. McGirr, J. LeDue, A. W. Chan, Y. Xie, and T. H. Murphy, “Cortical functional hyperconnectivity in a mouse model of depression and selective network effects of ketamine,” Brain, vol. 140, no. 8, pp. 2210–2225, 2017.

[10] A. G. Siapas and M. A. Wilson, “Coordinated interactions between hippocampal ripples and cortical spindles during slow-wave sleep,” Neuron, vol. 21, no. 5, pp. 1123–1128, 1998.

[11] J. B. Wekselblatt and C. M. Niell, “Distinct functional classes of excitatory neurons in mouse V1 are differentially modulated by learning and task engagement,” bioRxiv, p. 533463, 2019.

[12] M. Liu, C. Song, Y. Liang, T. Kno¨ pfel, and C. Zhou, “Assessing spatiotemporal variability of brain spontaneous activity by multiscale entropy and functional connectivity,” NeuroImage, vol. 198, pp. 198–220, 2019.

[13] M. B. Feller, D. P. Wellis, D. Stellwagen, F. S. Werblin, and C. J. Shatz, “Requirement for cholinergic synaptic transmission in the propagation of spontaneous retinal waves,” Science, vol. 272, no. 5265, pp. 1182–1187, 1996.

[14] M. B. Feller, D. A. Butts, H. L. Aaron, D. S. Rokhsar, and C. J. Shatz, “Dynamic processes shape spatiotemporal properties of retinal waves,” Neuron, vol. 19, no. 2, pp. 293–306, 1997.

[15] R. O. Wong, “Retinal waves and visual system development,” Annual review of

neuroscience, vol. 22, no. 1, pp. 29–47, 1999.

[16] A. Tiriac, B. E. Smith, and M. B. Feller, “Light prior to eye opening promotes retinal waves and eye-specific segregation,” Neuron, vol. 100, no. 5, pp. 1059–1065, 2018.

[17] C. Ren and T. Komiyama, “Characterizing cortex-wide dynamics with wide-field calcium imaging,” Journal of Neuroscience, vol. 41, no. 19, pp. 4160–4168, 2021.

[18] A. E. Urai, B. Doiron, A. M. Leifer, and A. K. Churchland, “Large-scale neural recordings call for new insights to link brain and behavior,” arXiv preprint arXiv:2103.14662, 2021.

[19] T. K. Sato, I. Nauhaus, and M. Carandini, “Traveling waves in visual cortex,” Neuron, vol. 75, no. 2, pp. 218–229, 2012.

[20] H. Dana, T.-W. Chen, A. Hu, B. C. Shields, C. Guo, L. L. Looger, D. S. Kim, and K. Svoboda, “Thy1-GCaMP6 transgenic mice for neuronal population imaging in vivo,” PloS one, vol. 9, no. 9, 2014.

[21] J. N. Stirman, I. T. Smith, M. W. Kudenov, and S. L. Smith, “Wide field-of-view, multi-region, two-photon imaging of neuronal activity in the mammalian brain,” Nature biotechnology, vol. 34, no. 8, pp. 857–862, 2016.

[22] G. Silasi, D. Xiao, M. P. Vanni, A. C. Chen, and T. H. Murphy, “Intact skull chronic windows for mesoscopic wide-field imaging in awake mice,” Journal of neuroscience methods, vol. 267, pp. 141–149, 2016.

[23] N. A. Steinmetz, C. Buetfering, J. Lecoq, C. R. Lee, A. J. Peters, E. A. Jacobs, P. Coen, D. R. Ollerenshaw, M. T. Valley, S. E. De Vries et al., “Aberrant cortical activity in multiple GCaMP6-expressing transgenic mouse lines,” eneuro, 2017.

[24] J. Couto, S. Musall, X. R. Sun, A. Khanal, S. Gluf, S. Saxena, I. Kinsella, T. Abe, J. P. Cunningham, L. Paninski et al., “Chronic, cortex-wide imaging of specific cell populations during behavior,” Nature Protocols, pp. 1–25, 2021.

[25] J. Nakai, M. Ohkura, and K. Imoto, “A high signal-to-noise Ca 2+ probe composed of a single green fluorescent protein,” Nature biotechnology, vol. 19, no. 2, pp. 137–141, 2001.

[26] L. Tian, S. A. Hires, T. Mao, D. Huber, M. E. Chiappe, S. H. Chalasani, L. Petreanu, J. Akerboom, S. A. McKinney, E. R. Schreiter, C. I. Bargmann, V. Jayaraman, K. Svoboda, and L. L. Looger, “Imaging neural activity in worms, flies and mice with improved GCaMP calcium indicators,” Nature methods, vol. 6, no. 12, p. 875, 2009.

[27] T.-W. Chen, T. J. Wardill, Y. Sun, S. R. Pulver, S. L. Renninger, A. Baohan, E. R. Schreiter, R. A. Kerr, M. B. Orger, V. Jayaraman, L. L. Looger, K. Svoboda, and D. S. Kim, “Ultrasensitive fluorescent proteins for imaging neuronal activity,” Nature, vol.

499, no. 7458, pp. 295–300, 2013.

[28] M. P. Vanni and T. H. Murphy, “Mesoscale transcranial spontaneous activity mapping in GCaMP3 transgenic mice reveals extensive reciprocal connections between areas of somatomotor cortex,” Journal of Neuroscience, vol. 34, no. 48, pp. 15 931–15 946, 2014.

[29] D. A. McVea, M. H. Mohajerani, and T. H. Murphy, “Voltage-sensitive dye imaging reveals dynamic spatiotemporal properties of cortical activity after spontaneous muscle twitches in the newborn rat,” Journal of Neuroscience, vol. 32, no. 32, pp. 10 982–10 994, 2012.

[30] C. Song, D. M. Piscopo, C. M. Niell, and T. Kno¨ pfel, “Cortical signatures of wakeful somatosensory processing,” Scientific reports, vol. 8, no. 1, pp. 1–12, 2018.

[31] B. B. Scott, S. Y. Thiberge, C. Guo, D. G. R. Tervo, C. D. Brody, A. Y. Karpova, and D. W. Tank, “Imaging cortical dynamics in GCaMP transgenic rats with a head-mounted widefield macroscope,” Neuron, vol. 100, no. 5, pp. 1045–1058, 2018.

[32] W. E. Allen, I. V. Kauvar, M. Z. Chen, E. B. Richman, S. J. Yang, K. Chan, V. Gradinaru, B. E. Deverman, L. Luo, and K. Deisseroth, “Global representations of goal-directed behavior in distinct cell types of mouse neocortex,” Neuron, vol. 94, no. 4, pp. 891–907, 2017.

[33] L. Pinto, K. Rajan, B. DePasquale, S. Y. Thiberge, D. W. Tank, and C. D. Brody, “Task-dependent changes in the large-scale dynamics and necessity of cortical regions,” Neuron, vol. 104, no. 4, pp. 810–824, 2019.

[34] E. A. Jacobs, N. A. Steinmetz, M. Carandini, and K. D. Harris, “Cortical state fluctuations during sensory decision making,” Biorxiv, p. 348193, 2018.

[35] P. Zatka-Haas, N. A. Steinmetz, M. Carandini, and K. D. Harris, “A perceptual decision requires sensory but not action coding in mouse cortex,” bioRxiv, p. 501627, 2020.

[36] P. W. Wright, L. M. Brier, A. Q. Bauer, G. A. Baxter, A. W. Kraft, M. D. Reisman, A. R. Bice, A. Z. Snyder, J.-M. Lee, and J. P. Culver, “Functional connectivity structure of cortical calcium dynamics in anesthetized and awake mice,” PloS one, vol. 12, no. 10, 2017.

[37] M. P. Vanni, A. W. Chan, M. Balbi, G. Silasi, and T. H. Murphy, “Mesoscale mapping of mouse cortex reveals frequency-dependent cycling between distinct macroscale functional modules,” Journal of Neuroscience, vol. 37, no. 31, pp. 7513–7533, 2017.

[38] D. R. Tabuena, R. Huynh, J. Metcalf, T. Richner, A. Stroh, B. W. Brunton, W. J. Moody, and C. R. Easton, “Pancortical waves in the neonatal rodent brain in vivo: A precursor of adult sleep waves?” In review., 2019.

[39] P. Holmes and J. Guckenheimer, Nonlinear oscillations, dynamical systems, and bifurcations of vector fields, ser. Applied Mathematical Sciences. Berlin, Heidelberg: Springer-Verlag, 1983, vol. 42.

[40] R. Pang, B. J. Lansdell, and A. L. Fairhall, "Dimensionality reduction in neuroscience," Current Biology, vol. 26, no. 14, pp. R656–R660, 2016.

[41] J. P. Cunningham and M. Y. Byron, "Dimensionality reduction for large-scale neural recordings," Nature neuroscience, vol. 17, no. 11, pp. 1500–1509, 2014.

[42] E. L. Dyer, M. G. Azar, M. G. Perich, H. L. Fernandes, S. Naufel, L. E. Miller, and K. P. Ko¨ rding, "A cryptographybased approach for movement decoding," Nature Biomedical Engineering, vol. 1, no. 12, pp. 967–976, 2017.

[43] S. Ganguli and H. Sompolinsky, "Compressed sensing, sparsity, and dimensionality in neuronal information processing and data analysis," Annual review of neuroscience, vol. 35, pp. 485–508, 2012.

[44] M. M. Churchland, J. P. Cunningham, M. T. Kaufman, J. D. Foster, P. Nuyujukian, S. I. Ryu, and K. V. Shenoy, "Neural population dynamics during reaching," Nature, vol. 487, no. 7405, pp. 51–56, 2012.

[45] J. A. Gallego, M. G. Perich, L. E. Miller, and S. A. Solla, "Neural manifolds for the control of movement," Neuron, vol. 94, no. 5, pp. 978–984, 2017.

[46] J. A. Gallego, M. G. Perich, R. H. Chowdhury, S. A. Solla, and L. E. Miller, "Long-term stability of cortical population dynamics underlying consistent behavior," Nature neuroscience, vol. 23, no. 2, pp. 260–270, 2020.

[47] J. P. Cunningham and Z. Ghahramani, "Linear dimensionality reduction: Survey, insights, and generalizations," The Journal of Machine Learning Research, vol. 16, no. 1, pp. 2859–2900, 2015.

[48] B. W. Brunton, L. A. Johnson, J. G. Ojemann, and J. N. Kutz, "Extracting spatial–temporal coherent patterns in large-scale neural recordings using dynamic mode decomposition," Journal of neuroscience methods, vol. 258, pp. 1–15, 2016.

[49] J. H. Tu, C. W. Rowley, D. M. Luchtenburg, S. L. Brunton, and J. N. Kutz, "On dynamic mode decomposition: theory and applications," Journal of Computational Dynamics, vol. 1, no. 2, pp. 391–421, 2014.

[50] J. N. Kutz, S. L. Brunton, B. W. Brunton, and J. L. Proctor, Dynamic mode decomposition: data-driven modeling of complex systems. SIAM, 2016.

[51] C. J. MacDowell and T. J. Buschman, "Low-dimensional spatiotemporal dynamics underlie cortex-wide neural activity," Current Biology, 2020.

[52] S. Saxena, I. Kinsella, S. Musall, S. H. Kim, J. Meszaros, D. N. Thibodeaux, C. Kim, J. Cunningham, E. M. Hillman, A. Churchland et al., "Localized semi-nonnegative matrix factorization (LocaNMF) of widefield calcium imaging data," PLOS Computational Biology, vol. 16, no. 4, p. e1007791, 2020.

[53] E. L. Mackevicius, A. H. Bahle, A. H. Williams, S. Gu, N. I. Denisenko, M. S. Goldman, and M. S. Fee, "Unsupervised discovery of temporal sequences in high-dimensional datasets, with applications to neuroscience," Elife, vol. 8, p. e38471, 2019.

[54] P. Zhou, S. L. Resendez, J. Rodriguez-Romaguera, J. C. Jimenez, S. Q. Neufeld, A. Giovannucci, J. Friedrich, E. A. Pnevmatikakis, G. D. Stuber, R. Hen et al., "Efficient and accurate extraction of in vivo calcium signals from microendoscopic video data," Elife, vol. 7, p. e28728, 2018.

[55] T. P. Zanos, P. J. Mineault, K. T. Nasiotis, D. Guitton, and C. C. Pack, "A sensorimotor role for traveling waves in primate visual cortex," Neuron, vol. 85, no. 3, pp. 615–627, 2015.

[56] A. G. Blankenship, A. M. Hamby, A. Firl, S. Vyas, S. Maxeiner, K. Willecke, and M. B. Feller, "The role of neuronal connexins 36 and 45 in shaping spontaneous firing patterns in the developing retina," Journal of Neuroscience, vol. 31, no. 27, pp. 9998–10 008, 2011.

[57] N. Afrashteh, S. Inayat, M. Mohsenvand, and M. H. Mohajerani, "Optical-flow analysis toolbox for characterization of spatiotemporal dynamics in mesoscale optical imaging of brain activity," Neuroimage, vol. 153, pp. 58–74, 2017.

[58] R. G. Townsend and P. Gong, "Detection and analysis of spatiotemporal patterns in brain activity," PLoS computational biology, vol. 14, no. 12, p. e1006643, 2018.

[59] G. Haller, "Lagrangian coherent structures from approximate velocity data," Physics of Fluids, vol. 14, no. 6, pp. 1851–1861, June 2002.

[60] S. C. Shadden, Lagrangian Coherent Structures. John Wiley & Sons, Ltd, 2011, ch. 3, pp. 59–89. [Online]. Available: https://onlinelibrary.wiley.com/doi/abs/10.1002/9783527639748.ch3

[61] G. Haller, "Lagrangian coherent structures," Annual Review of Fluid Mechanics, vol. 47, pp. 137–162, 2015.

[62] S. C. Shadden, F. Lekien, and J. E. Marsden, "Definition and properties of lagrangian coherent structures from finite-time lyapunov exponents in two-dimensional aperiodic flows," Physica D: Nonlinear Phenomena, vol. 212, no. 3-4, pp. 271–304, 2005.

[63] M. Mathur, G. Haller, T. Peacock, J. E. Ruppert-Felsot, and H. L. Swinney, "Uncovering the Lagrangian skeleton of turbulence," Physical Review Letters, vol. 98, pp.

502–1–502–4, 2007.

[64] M. A. Green, C. W. Rowley, and G. Haller, "Detection of Lagrangian coherent structures in 3D turbulence." Journal of Fluid Mechanics, vol. 572, pp. 111–120, 2007.

[65] S. L. Brunton and C. W. Rowley, "Fast computation of FTLE fields for unsteady flows: a comparison of methods," Chaos, vol. 20, p. 017503, 2010.

[66] M. Farazmand and G. Haller, "Computing Lagrangian coherent structures from their variational theory," Chaos, vol. 22, no. 013128, pp. 128–1–128–12, 2012.

[67] J. Peng and J. Dabiri, "Transport of inertial particles by lagrangian coherent structures: application to predator– prey interaction in jellyfish feeding," Journal of Fluid Mechanics, vol. 623, pp. 75–84, 2009.

[68] V. Duvernois, A. L. Marsden, and S. C. Shadden, "Lagrangian analysis of hemodynamics data from fsi simulation," International journal for numerical methods in biomedical engineering, vol. 29, no. 4, pp. 445–461, 2013.

[69] S. C. Shadden and A. Arzani, "Lagrangian postprocessing of computational hemodynamics," Annals of biomedical engineering, vol. 43, no. 1, pp. 41–58, 2015.

[70] M. H. Mohajerani, A. W. Chan, M. Mohsenvand, J. LeDue, R. Liu, D. A. McVea, J. D. Boyd, Y. T. Wang, M. Reimers, and T. H. Murphy, "Spontaneous cortical activity alternates between motifs defined by regional axonal projections," Nature neuroscience, vol. 16, no. 10, p. 1426, 2013.

[71] D. M. Ashby, J. LeDue, T. H. Murphy, and A. McGirr, "Peripheral nerve ligation elicits widespread alterations in cortical sensory evoked and spontaneous activity," Scientific reports, vol. 9, no. 1, pp. 1–10, 2019.

[72] H. Jia, N. L. Rochefort, X. Chen, and A. Konnerth, "In vivo two-photon imaging of sensory-evoked dendritic calcium signals in cortical neurons," Nature protocols, vol. 6, no. 1, pp. 28–35, 2011.

[73] K. Onu, F. Huhn, and G. Haller, "LCS Tool: a computational platform for lagrangian coherent structures," Journal of Computational Science, vol. 7, pp. 26–36, 2015.

[74] N. Paragios, Y. Chen, and O. D. Faugeras, Handbook of mathematical models in computer vision. Springer Science & Business Media, 2006.

[75] C. J. Duffy and R. H. Wurtz, "Sensitivity of MSTneurons to optic flow stimuli. II. Mechanisms of response selectivity revealed by small-field stimuli," Journal of neurophysiology, vol. 65, no. 6, pp. 1346–1359, 1991.

[76] H. G. Krapp and R. Hengstenberg, "Estimation of self-motion by optic flow processing in single visual interneurons," Nature, vol. 384, no. 6608, pp. 463–466, 1996.

[77] B. K. Horn and B. G. Schunck, “Determining optical flow,” in Techniques and Applications of Image Understanding, vol. 281. International Society for Optics and Photonics, 1981, pp. 319–331.

[78] C. E. Willert and M. Gharib, “Digital particle image velocimetry,” Experiments in fluids, vol. 10, no. 4, pp. 181–193, 1991.

[79] J. Westerweel, “Fundamentals of digital particle image velocimetry,” Measurement science and technology, vol. 8, no. 12, p. 1379, 1997.

[80] K. Taira, S. L. Brunton, S. Dawson, C. W. Rowley, T. Colonius, B. J. McKeon, O. T. Schmidt, S. Gordeyev, V. Theofilis, and L. S. Ukeiley, “Modal analysis of fluid flows: An overview,” AIAA Journal, vol. 55, no. 12, pp. 4013–4041, 2017.

[81] K. Taira, M. S. Hemati, S. L. Brunton, Y. Sun, K. Duraisamy, S. Bagheri, S. Dawson, and C.-A. Yeh, “Modal analysis of fluid flows: Applications and outlook,” AIAA Journal, vol. 58, no. 3, pp. 998–1022, 2020.

[82] C. Garth, F. Gerhardt, X. Tricoche, and H. Hans, “Efficient computation and visualization of coherent structures in fluid flow applications,” IEEE Transactions on Visualization and Computer Graphics, vol. 13, no. 6, pp. 1464–1471, 2007.

[83] D. Lipinski and K. Mohseni, “A ridge tracking algorithm and error estimate for efficient computation of lagrangian coherent structures,” Chaos: An Interdisciplinary Journal of Nonlinear Science, vol. 20, no. 1, p. 017504, 2010.

[84] O. Garaschuk, J. Linn, J. Eilers, and A. Konnerth, “Large-scale oscillatory calcium waves in the immature cortex,” Nature neuroscience, vol. 3, no. 5, pp. 452–459, 2000.

[85] J. Conhaim, C. R. Easton, M. I. Becker, M. Barahimi, E. R. Cedarbaum, J. G. Moore, L. F. Mather, S. Dabagh, D. J. Minter, S. P. Moen et al., “Developmental changes in propagation patterns and transmitter dependence of waves of spontaneous activity in the mouse cerebral cortex,” The Journal of physiology, vol. 589, no. 10, pp. 2529–2541, 2011.

[86] C. R. Easton, K. Weir, A. Scott, S. P. Moen, Z. Barger, A. Folch, R. F. Hevner, and W. J. Moody, “Genetic elimination of gabaergic neurotransmission reveals two distinct pacemakers for spontaneous waves of activity in the developing mouse cortex,” Journal of Neuroscience, vol. 34, no. 11, pp. 3854–3863, 2014.

[87] Z. Barger, C. R. Easton, K. E. Neuzil, and W. J. Moody, “Early network activity propagates bidirectionally between hippocampus and cortex,” Developmental neurobiology, vol. 76, no. 6, pp. 661–672, 2016.

[88] A. M. Seelke and M. S. Blumberg, “Developmental appearance and disappearance of cortical events and oscillations in infant rats,” Brain research, vol. 1324, pp. 34–42,

2010.

[89] M. S. Blumberg, A. J. Gall, and W. D. Todd, “The development of sleep–wake rhythms and the search for elemental circuits in the infant brain.” Behavioral neuroscience, vol. 128, no. 3, p. 250, 2014.

[90] Q. Wang, S.-L. Ding, Y. Li, J. Royall, D. Feng, P. Lesnar, N. Graddis, M. Naeemi, B. Facer, A. Ho et al., “The Allen Mouse Brain Common Coordinate Framework: A 3D reference atlas,” Cell, 2020.

[91] S. H. Rudy, S. L. Brunton, J. L. Proctor, and J. N. Kutz, “Data-driven discovery of partial differential equations,” Science Advances, vol. 3, no. 4, p. e1602614, 2017.

[92] H. Schaeffer, “Learning partial differential equations via data discovery and sparse optimization,” in Proc. R. Soc. A, vol. 473, no. 2197. The Royal Society, 2017, p. 20160446.

[93] M. Kharbat, “Horn-Schunck optical flow method,” MATLAB Central File Exchange, 2009. [Online]. Available: https://www.mathworks.com/matlabcentral/fileexchange/22756-horn-schunck-optical-flow-method

[94] C. Gonzalez, R, E. Woods, R, and L. Eddins S, Digital Image Processing Using MATLAB. Gatesmark Publishing, 2009.

[95] M. Haralick, Robert and G. Shapiro, Linda, Computer and Robot Vision, Vol 1. Addison-Wesley, 1992.

Supplemental Materials

1 Code and Data Access

All code and data developed to construct FLOWportraits and to run analyses shown here is freely available in a repository at `https://github.com/natejlinden/FLOWPortrait`. The code is implemented in MATLAB 2017b. A basicMATLAB implementation withMATLAB’s Image Processing Toolbox (`https://www.mathworks.com/products/image.html`) is enough to reproduce the figures and run additional FLOW Portrait analyses. The data required to create the figures from the developing mouse dataset [38] and from the adult mouse dataset [35] are included in the repository.

2 Supplemental Videos

Supplemental videos 1–5 are available in the repository at https://github.com/natejlinden/FLOWPortrait/tree/master/SupplementaryVideos.

Video Captions

Video 1 – Steps to compute a FLOW portrait for a synthetic two-dimensional Gaussian that grows, translates to the right, then shrinks. This synthetic example is depicted in Figure 1, and Supplemental Figures 2 and 4. (Raw Data) Raw spatiotemporal data for the two-dimensional Gaussian example. (Optical Flow) The optical flow vector field overlaid on the original data. Optical flow is used to convert frame-by-frame changes in pixel intensity into a vector field. (Particles) Uniformly spaced particles are propagated through space according to the optical flow vector field. The particles' positions are updated by adding a displacement that corresponds to the vector field multiplied by a unit time step. Regions where particles cluster will be captured as ridges in the backward time FTLE and regions where particles separate will be captured as ridges in the forward time FTLE. (FLOW Portrait) The final FLOW portrait for this dataset. Orange structures correspond to the forward time FTLE and show regions where activity is repelled; purple structures correspond to the backward time FTLE and show regions where activity is attracted. The FLOW portrait was computed using a 10 frame integration length and a 85th threshold percentile.

Video 2 – An example pan cortical wave (left pane) in widefield imaging data recorded from a developing mouse and the corresponding FLOW portrait (right pane). This wave event is depicted in Figure 6B as 32 wave ii. The video is played at 20 frames per second such that one second of video corresponds to one second of recording. The FLOW portrait was computed using an integration length of 2 seconds (40 frames), and a visualization threshold of 0.92.

Video 3 – An example pan cortical wave (left pane) in widefield imaging data recorded from a developing mouse and the corresponding FLOW portrait (right pane). This wave event is depicted in Figure 6B as wave i. Note, the FLOW portrait differs from that seen in the figure due to differences in thresholding. The video is played at 20 frames per second such that one second of video corresponds to one second of recording. The FLOW portrait was computed using an integration length of 2 seconds (40 frames), and a visualization threshold of 0.92.

Video 4 – An example bout of spontaneous (left pane) cortical activity in widefield imaging data recorded from an adult mouse and the corresponding FLOW portrait (right pane). This bout is depicted in Figure 8 as bout i. The video is played at 20 frames per second such that one second of video corresponds to one second of recording. The FLOW portrait was computed using an integration length of approximately 0.4 seconds (15 frames), and a visualization threshold of 0.93.

Video 5 – An example bout of spontaneous (left pane) cortical activity in widefield imaging data recorded from an adult mouse and the corresponding FLOW portrait (right pane). This bout is depicted in Figure b as bout ii. The video is played at 20 frames per second such that one second of video corresponds to one second of recording. The FLOW portrait was computed using an integration length of approximately 0.4 seconds (15 frames), and a visualization threshold of 0.93.

3 Supplemental Figures

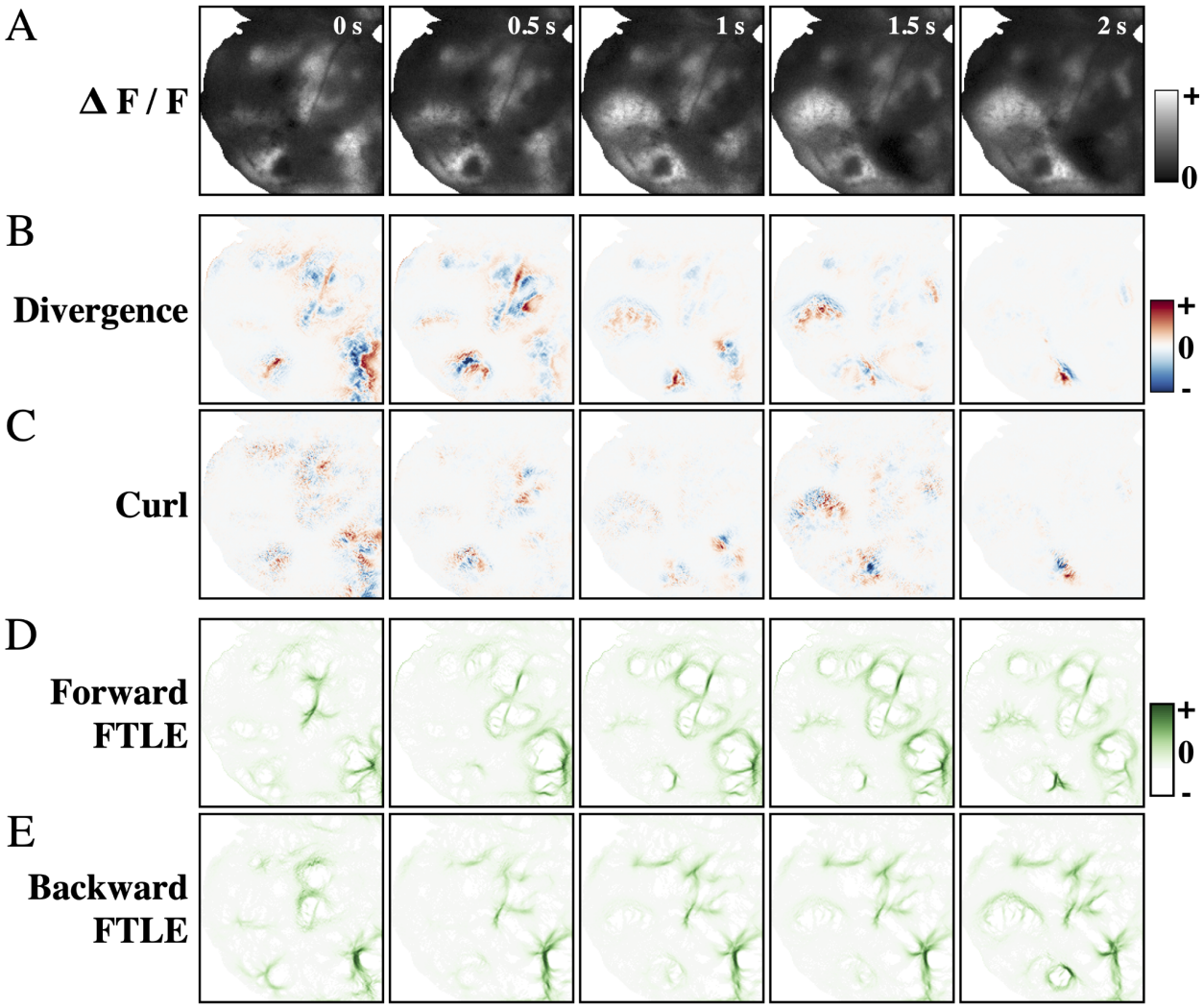

Supplemental Figure 1: The unsteady nature of widefield imaging data suggested Lagrangian metrics (FTLE) will prove more useful than instantaneous metrics (divergence and curl) in summarizing activity. (A) Widefield imaging data from which instantaneous divergence and curl along with the Lagrangian FTLE are computed. Instantaneous divergence (B) and curl (C) show a similar unsteady nature to the data. Meanwhile, persistent features in the forward and backward FTLEs (D and E, respectively) can summarize the activity seen throughout the segment of data.

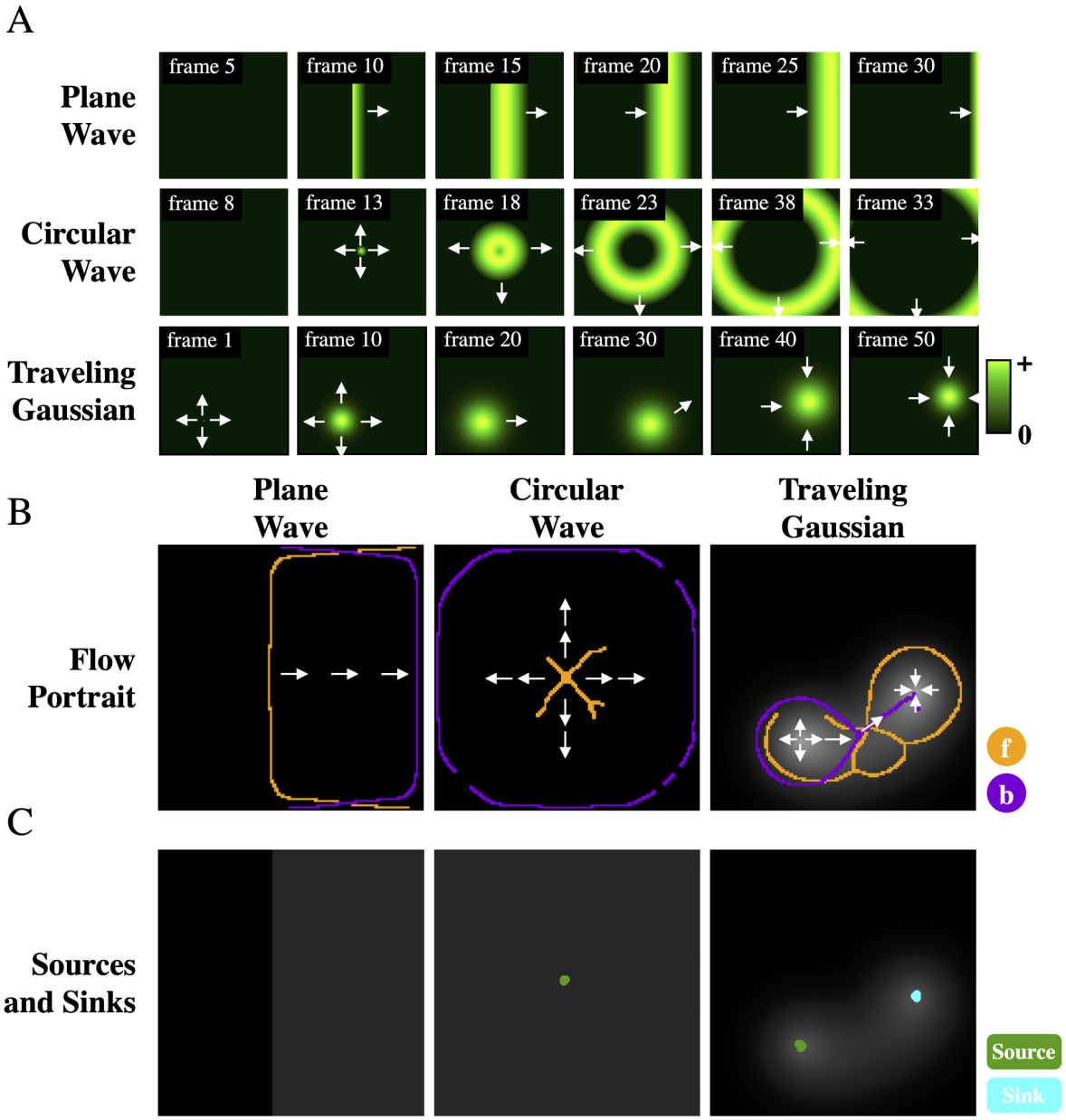

Supplemental Figure 2: (A) Three additional synthetic examples for which we illustrate FLOW portraits and compare to source sink analysis. The 'Plane Wave' example shows a traveling plane wave which begins in the center of the frame and propagates to the right. The 'CircularWave' example shows a traveling circular wave which begins in the center of the frame and expands outwards. The 'Traveling Gaussian' example shows a 2-D Gaussian which grows (a source), translates, and shrinks (a sink). White arrows indicate the direction of activity propagation. (B) The FLOW portraits for both synthetic examples. White arrows show the general directions of activity propagation. FLOW portraits were computed with integration lengths of15 frames, 12 frames and 10 frames and the threshold percentile was set to the 91st, 93rd and the 85th percentile for the plane wave, circular wave and traveling Gaussian datasets respectively. (C) Sources (green)and sinks (cyan) identified using the Optical Flow Analysis Toolbox for Wide-field Neuroimaging [57].

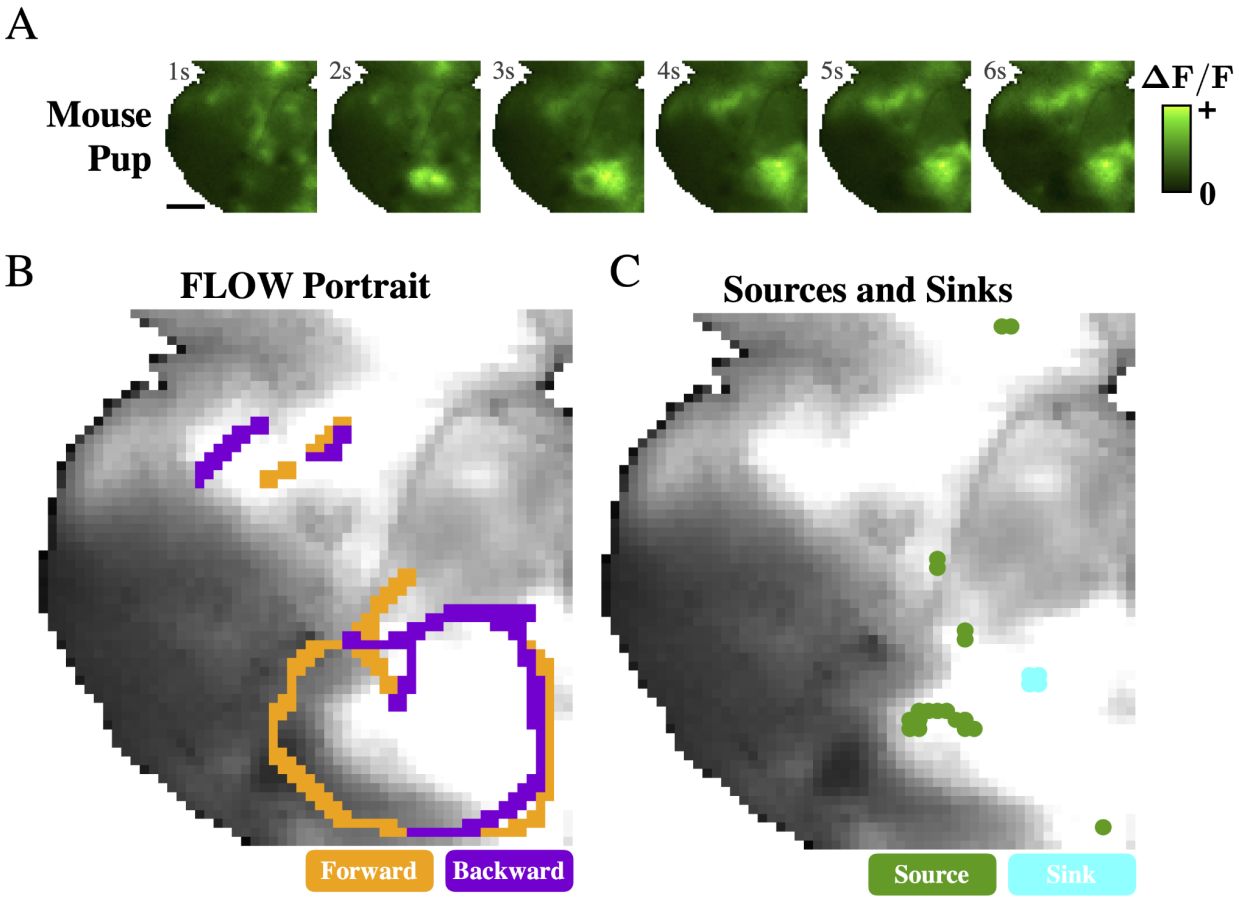

Supplemental Figure 3: FLOW portraits provide a summary of the flow beyond identifying sources and sinks. (A)Widefield imaging data from which FLOW portraits were compared to source sink analysis. The widefield imaging dataset depicts a prominent wave towards the bottom of the frame and an additional wave near the top (scale bar is 1mm). (B) FLOW portraits for the data shown above with a 20 frame integration length and a 91% threshold percentile. (C) Sources (green) and sinks (cyan) identified using the Optical Flow Analysis Toolbox forWide-field Neuroimaging [57]. Comparison with the FLOW portraits highlights how FLOW portraits summarize the overall pattern of activity beyond identifying the sources and sinks.

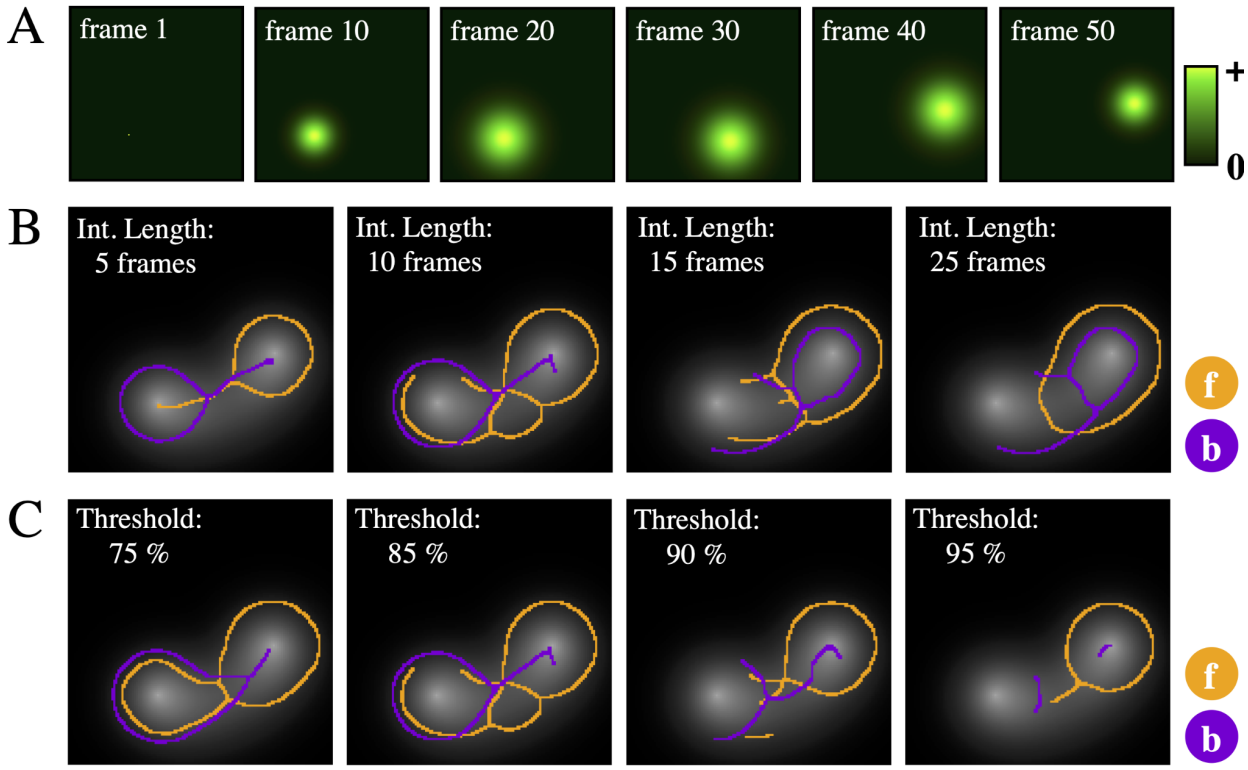

Supplemental Figure 4: Effects of integration length and threshold percentile hyperparameters on FLOW portraits. (A) Synthetic traveling Gaussian examples for which we illustrate the effects of hyperparameters on FLOW portraits. (B) Increasing the integration length resolves more detail in the FLOW portrait until a critical integration length is reached. Integration lengths beyond the critical value begin to lose detail. The critical integration length is around 10 frames in this example. All FLOW portraits were computed with the threshold percentile fixed to 85%. (C) Thresholding the FTLE field enables isolation of FTLE ridges. However, ridge information will be lost if the threshold percentile is too large. All FLOW portraits were computed with the integration length fixed to 10 frames.

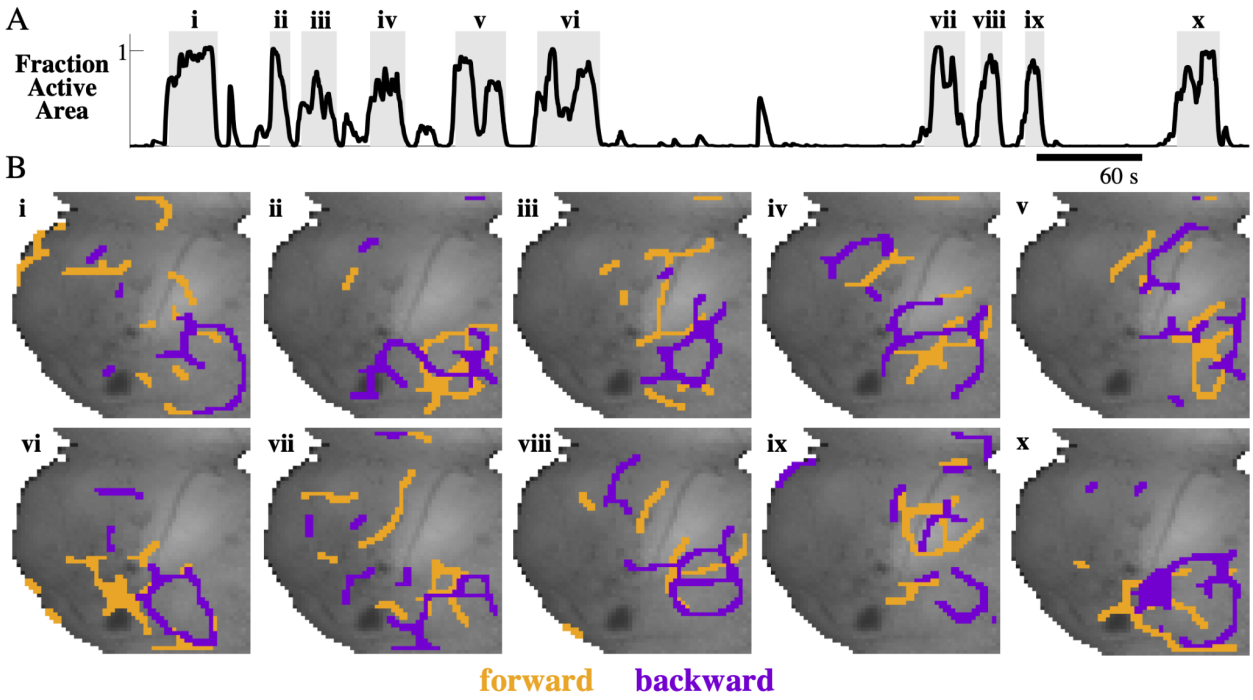

Supplemental Figure 5: Flow portraits for all examples of pan-cortical waves events analyzed in Figure 5. (A) Ten additional pan-cortical events are seen, as indicated by events where the area of active cortex crosses the 50% threshold (i-x). Events iv and x are analyzed in Figure 5 and are repeated here. (B) FLOW portraits for each pan-cortical wave can be used to summarize the distinct activity that occurs during each event. All portraits were computed with an integration length of 40 frames and the threshold percentile was set to the 92nd percentile.

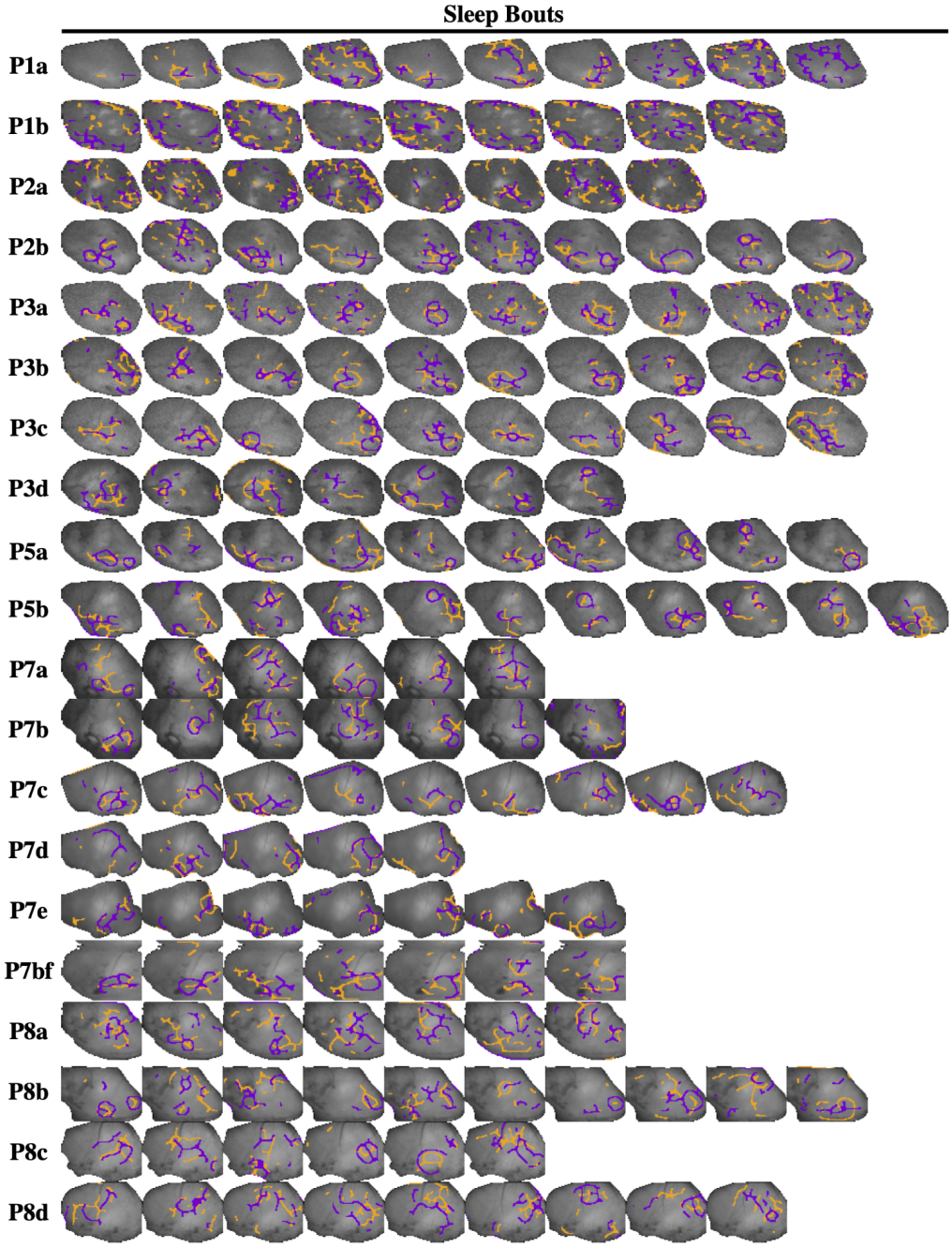

Supplemental Figure 6: FLOW portraits of all sleep bouts from 20 P1-8 mouse pups are shown. A subset of examples from P1-8a,b are shown in Figure 6, while additional examples are shown here. All portraits were computed with an integration length of 40 frames and the threshold percentile was set to the 93rd percentile.

Conclusion

Through these studies we have gained a clearer picture of the nature and properties of cortical waves *in vivo* and have laid the groundwork for further study with advanced recording methods and analysis tools. In anesthetized adult mice we demonstrated that the cortex can produce multiple states including those permissive, or not permissive, for cortical waves. In both states the primary sensory response was always present but only in the slow wave state did information propagate out of the primary sensory cortex carried by low frequency oscillations. While the two anesthetized states can only approximate natural brain states like wake and sleep, they provide a window into how functional connectivity can be altered through changing states allowing differential control over the flow of information. It remains unclear how this regulation occurs, however cortical inhibitory neuron populations have been shown to alter activity according to changes in natural sleep and wake states (Niethard et al, 2016). Thus control of cortical spread of activity may be modulated through interneurons restricting the spread of activity. In addition, segregating this state of widespread wave propagation into sleep states suggests that the permissive state may share commonalities with slow wave sleep typified by broad delta wave activity. It will be of course necessary to expand these studies to more natural states however the practicality and reliability to induce the states will likely continue to be advantageous in pursuing finer grained analysis into the mechanism of wave regulation.

We were able to make several advances in understanding of the regulation of cortical activity in the neonatal mouse. While previous studies have also focused on the early postnatal period, the area of the cortex studied was small, thus limiting the conclusions that could be drawn about large-scale activity (Rio-Bermudez et al., 2020, Blumberg et al., 2020), and work imaging whole cortex is becoming more common (Gupta and Murphy 2019, Murphy 2020), recording large areas of cortex in neonates whose cranium remains soft has not proved feasible until now. By adapting these methods for neonates we were able to demonstrate cortical calcium waves do indeed occur in the whole animal, and that these waves are not yet present at birth but emerge by the end of the first postnatal week. Furthermore we were also able to demonstrate that waves are restricted to periods of sleep through observations of natural sleep-wake behavior and using sleep deprivation to disrupt wave activity. Overall functional connectivity was also increased during sleep as indicated by observations through NMF feature analysis and differential spatial correlations within the cortex, where we found increased NMF feature size and higher spatial correlation between distant areas, indicating higher levels of synchronization across the cortex. During these periods we observed increases in coordinated oscillations in a broad frequency range across the cortex.

Based on this evidence we can conclude that, as was the case in the adult brain, early in development state changes are used to allow differential control of information flow in the cortex. The mechanism allowing these state switches remains unclear, however it seems likely that GABA signaling may play a role given that the onset of the GABA inhibitory coincides with key changes in vitro control of Ca waves in slices (Conhaim et al., 2011) and differential modulation of inhibitory neuron populations in adult sleep (Niethard et al, 2016). Our newly developed system could yield significant light on this issue as our model is easily adaptable to probe other cell populations such as inhibitory neurons using the modular Cre system. Also unclear is the exact role that these waves play during development. Spontaneous activity and local synchronizations have been shown provide mechanism for establishing long range connections, increasing synaptogenesis, and protection from apoptosis (Blankenship and Feller,

2010; Kilb et al., 2011; Riyahi et al., 2021; Chang & Kanold, 2021). Further studies with our model could shed light on the developmental role of waves. Given that we can now identify and selectively interrupt waves through closed-loop forced waking it may be possible to determine long term effects on brain development. Furthermore genetic surveys of developmental disorders such as autism strongly point towards defects in the early circuit formation expected during Ca generation (Parikshak et al., 2013). Thus it may be feasible to study wave disruption in a translationally relevant genetic model to explore the relation between waves and development.

References:

Blankenship, A. G., & Feller, M. B. (2010). Mechanisms underlying spontaneous patterned activity in developing neural circuits. In Nature Reviews Neuroscience. https://doi.org/10.1038/nrn2759

Blumberg, M. S., Dooley, J. C., & Sokoloff, G. (2020). The developing brain revealed during sleep. Current Opinion in Physiology, 15, 14–22. https://doi.org/10.1016/J.COPHYS.2019.11.002

Chang, M., & Kanold, P. O. (2021). Development of Auditory Cortex Circuits. Journal of the Association for Research in Otolaryngology 2021 22:3, 22(3), 237–259. https://doi.org/10.1007/S10162-021-00794-3

Conhaim, J., Easton, C. R., Becker, M. I., Barahimi, M., Cedarbaum, E. R., Moore, J. G., Mather, L. F., Dabagh, S., Minter, D. J., Moen, S. P., & Moody, W. J. (2011). Developmental changes in propagation patterns and transmitter dependence of waves of spontaneous activity in the mouse cerebral cortex. Journal of Physiology, 589(10), 2529–2541. https://doi.org/10.1113/jphysiol.2010.202382

Del Rio-Bermudez, C., Kim, J., Sokoloff, G., & Blumberg, M. S. (2020). Active Sleep Promotes Coherent Oscillatory Activity in the Cortico-Hippocampal System of Infant Rats. Cerebral Cortex, 30(4), 2070–2082. https://doi.org/10.1093/cercor/bhz223

Gupta, P. K., & Murphy, T. H. (2019). Cortex-wide Computations in Complex Decision Making in Mice. Neuron, 104(4), 631–633. https://doi.org/10.1016/J.NEURON.2019.10.043

Kilb, W., Kirischuk, S., & Luhmann, H. J. (2011). Electrical activity patterns and the functional maturation of the neocortex. In European Journal of Neuroscience. https://doi.org/10.1111/j.1460-9568.2011.07878.x

Murphy, T. H., Michelson, N. J., Boyd, J. D., Fong, T., Bolaños, L. A., Bierbrauer, D., Siu, T., Balbi, M., Bolaños, F., Vanni, M., & Ledue, J. M. (2020). Automated task training and longitudinal monitoring of mouse mesoscale cortical circuits using home cages. ELife, 9, 1–91. https://doi.org/10.7554/ELIFE.55964

Niethard, N., Hasegawa, M., Itokazu, T., Oyanedel, C. N., Born, J., & Sato, T. R. (2016). Sleep-Stage-Specific Regulation of Cortical Excitation and Inhibition. Current Biology. https://doi.org/10.1016/j.cub.2016.08.035

Parikshak, N. N., Luo, R., Zhang, A., Won, H., Lowe, J. K., Chandran, V., Horvath, S., & Geschwind, D. H. (2013). Integrative functional genomic analyses implicate specific molecular pathways and circuits in autism. Cell, 155(5), 1008. https://doi.org/10.1016/j.cell.2013.10.031

Riyahi, P., Phillips, M. A., & Colonnese, M. T. (2021). Input-Independent Homeostasis of Developing Thalamocortical Activity. ENeuro, 8(3). https://doi.org/10.1523/ENEURO.0184-21.2021